Silicon Microwire Arrays for Photoelectrochemical and Photovoltaic Applications

Thesis by
Emily Lowell Warren

In Partial Fulfillment of the Requirements
for the Degree of
Doctor of Philosophy

California Institute of Technology
Pasadena, California

2013

(Defended November 8, 2012)

In memory of Grandpa Bob, PhD

Acknowledgements

Looking back on my time at Caltech I am amazed at how many smart and talented people I have had the opportunity to interact with over the past five years. First and foremost, I would like to thank Nate Lewis for being a great mentor, giving me the space to figure out exactly what it was that I wanted to do, and exposing me to the world of politics and policy that is so closely tied to our particular field of research. Harry Atwater has been a second academic mentor, always welcoming me into his group, which became a second home to me during grad school. I would also like to thank my committee members: Sossina Haile and Rick Flagan for their continued advice and support. While not technically on my committee, Bruce Brunschwig has been an invaluable resource and truly is "the scientist everyone wants to be when they grow up."

I am honored to have been a part of "Team Nanowire" since my early days at Caltech. The friendly, collaborative environment that has thrived among the growers of silicon wires is something that is rare and I have learned a lot from everyone involved. The core members: Brendan Kayes, Mike Filler, Morgan Putnam, Mike Kelzenberg, Josh Spurgeon, Shannon Boettcher, Adele Tamboli, Dan Turner-Evans, Hal Emmer, Chris Chen, Liz Santori, Matt Bierman, Ron Grimm, and Anna Beck have maintained equipment, run evaporations, made single wire measurements, and all the other little things that made all of my research possible. From late night wire growth to poker night, you have all been great collaborators and friends.

When I first showed up in the Lewis group, without any idea of how to do electrochemistry, Stephen Maldonado and Jim Maiolo were the first people to help me/let me fail a few times until I figured things out for myself. Shannon Boettcher taught me how to work like a mad scientist and the importance of optimism in research. I would like to thank James McKone for being a great collaborator who could see the big picture and also understand the tiniest of experimental details. Heather Audesirk has already proven herself to be an excellent researcher and I am grateful for all of her hard work on the projects we have tackled together. Ron Grimm cannot be thanked enough for taking the time to answer every question on every subject and turning my dream of an organized lab into a reality.

The smartest thing I ever did in grad school was to take on Jessie Ku as a SURF student, and then keep her around for two more years. She is not only an incredibly productive researcher, but also makes a mean tiramisu. Liz Santori and Leslie O'Leary have been my rocks, inside and outside the lab; I might not have joined the Lewis group if they hadn't, and I'm glad we all made it through grad school together.

I am indebted to the wonderful people who have taken time to help me with equipment training, or letting me borrow chemicals or tools over the years: David Knapp, Craig Wiggenhorn, Joseph Beardslee, Anna Folinsky, Amy Hoffman, Emily Warrmann, Kelsey Whitesall, and Andrew Leenheer to name a few. While I was in grad school, the number of post-docs in our group exploded from two to ten, but I am so thankful for all of the great hallway conversations I have had with Kate Plass, CX Xiang, Nick Strandwitz, Shane Ardo, Erik Johansson, Mike Walter, Mike Rose, Bryce Stadtler, Ron Grimm, and Rob Coridan. There were also the grad students who made coming to work everyday just a little bit more fun, so thank you Edgardo Garcia-Berrios, Greg Kimball, Matt Shaner, and Adam Nichols-Nielander. I am also grateful for the opportunity to have shared lab and office space with the ever growing Lewis group, including: Heather McCaig, Amanda Shing, Don Walker, David Gleason-Rohrer, Jacob Good, Adam Pieterick, Noah Plymale, Fan Yang,

and Teddy Huang. Also, thanks to everyone in the Atwater group who kept me entertained in the hallways of Watson, at lunch, or at conferences far from home: Vivian Ferry, Imogen Price, Emily Kosten, Matt Sheldon, Ryan Briggs, Ana Brown, Chris Flowers, Raymond Weitekamp, Jeff Bosco, Ken Diest, Dennis Callahan, Faisal Tajdar, Samantha Wilson, and Carissa Eisler.

After working in the user facility labs around campus, I have come to realize how indispensable the staff are for keeping the equipment operational, regardless of how many stupid mistakes the grad students can make. Chi Ma of the GPS Analytical Facility is somewhat of a personal hero for his amazing microscopy skills and endless patience. I would like to thank the KNI staff: Melissa Melendes, Bophan Chim, Nils Asplund, Guy DeRose, and Chris Morales, for their ability to keep the lab running no matter what the users manage to break. I would also like to thank the super-user graduate students in the KNI who were generous with their time: particularly Jim Fakones, David Henry, and Sameer Walavalkar. My research was enabled by access to equipment in Bruce Brunschwig's MMRC, as well as the technical expertise of Rick Gerhart and Mike Roy in the glass/tool shops in the sub-basement of Church.

I am grateful for the amazing administrative assistants across campus who have put up with my never-ending questions: Amy Crown, Elyse Garlock, April Nieldholt, Lyra Haas, Tiffany Kimoto, Jennifer Blankenship, and Kathy Bubash. I would particularly like to thank Barbara Miralles for helping me stay sane at the end of my grad school career. I would also like to thank Felicia Hunt, Sue Chiarchiaro, and Jeff and Karen Blake for their support of the graduate RA program and for lots of free lunches, as well as my fellow RAs: Zeesh Ahmed, Andy Downard, and Devin Wiley who kept those lunch meetings entertaining.

Outside of the lab I am thankful for my amazing friends who have helped keep me sane and my family for their never-ending support. My parents, brother, grandparents, and Rusty and Lulu have stuck with me through twenty-two years of school, never once encouraging me to "get a real job." Last but not least, Mike Deceglie not only helped me with device physics simulation, but has also put up with my tears, rants, and propensity to stay at work two hours later than planned. I couldn't have made it through grad school without his love, support, and coffee-making abilities.

Emily L. Warren
November 2012
Pasadena, CA

Abstract

Si microwire (Si MW) arrays grown by the vapor-liquid-solid (VLS) process are promising materials for next-generation solar energy devices. High-aspect-ratio semiconductor structures have attracted recent interest as solar absorber materials because their radial geometry decouples the direction of light absorption and carrier collection, enabling the use of materials with shorter minority-carrier diffusion lengths than would be acceptable in a planar geometry. The VLS growth process is a low-cost deposition technique, which can be used to fabricate flexible, high-performance semiconductor materials. Si MW arrays have been investigated as an inexpensive alternative to wafer-based solar photovoltaics for low-cost electricity generation. Another potential application is to use these vertically oriented wire arrays as photocathodes of a solar fuel conversion devices, where instead of producing electricity, sunlight is used to directly drive a fuel-forming reaction (e.g., splitting water to form O_2 and H_2). The high aspect ratio of the Si MW arrays provides a large surface area for the integration of fuel-forming catalysts, allowing for the development of a low-cost, scalable, energy storage technology.

This thesis discusses the fabrication and photoelectrochemical characterization of Si MWs grown by the VLS process, focusing on the use of these wire arrays as hydrogen-evolving photocathodes for solar water-splitting. To optimize such a device it is important to balance all of the factors that will affect performance: light absorption, band energetics, attainable open circuit voltage, and catalysis. First, we characterize the electrical performance of the wire arrays using regenerative photoelectrochemistry to understand the material quality and band energetics at the Si/water interface. We demonstrate the fabrication of H_2-evolving photocathodes using p-n junction Si MW arrays and earth-abundant Ni–Mo alloy hydrogen evolution catalysts. We then investigate modifying the fabrication techniques for wire growth to lower the cost and processing time required to grow arrays of Si MWs. Finally, we study the band energetics of Si decorated with Pt to build a preliminary model of the heterogeneous catalyst/semiconductor/liquid interface.

Contents

List of Figures

List of Tables

List of Publications

Portions of this thesis have been drawn from the following publications:

- E. L. Warren, J. R. McKone, H. A. Atwater, H. B. Gray, and N. S. Lewis. Hydrogen-Evolution Characteristics of NiMo-Coated, Radial Junction, n^+p Silicon Microwire Array Photocathodes. *Energy & Environmental Science*, 5, 9653–9661, 2012.

- E. L. Warren, D. B. Turner-Evans, R. L. Grimm, H. A. Atwater, N. S. Lewis. Photoelectrochemical Characterization of Si Microwire Array Solar Cells. *Proceedings of the 38th IEEE Photovoltaics Specialist Conference*, Austin, Texas, 2012.

- A. C. Tamboli, C. T. Chen, E. L. Warren, D. B Turner-Evans, M. D. Kelzenberg, H. A. Atwater, and N. S. Lewis. Wafer-scale growth of Silicon Microwire Arrays for Photovoltaics. *Journal of Photovoltaics*, 2(3), 2012.

- S. W. Boettcher, J. M. Spurgeon, M. C. Putnam, E. L. Warren, D. B. Turner-Evans, M. D. Kelzenberg, J. R. Maiolo, H. A. Atwater, and N. S. Lewis. Energy-conversion properties of vapor-liquid-solid-grown silicon wire-array photocathodes. *Science*, 327, 185–187, 2010.

- J. R. McKone, E. L. Warren, M. J. Bierman, S. W. Boettcher, B. S. Brunschwig, N. S. Lewis, and H. B. Gray. Evaluation of Pt, Ni, and Ni-Mo Electrocatalysts for Hydrogen Evolution on Crystalline Si Electrodes. *Energy & Environmental Science*, 4, 3573–3583, 2011.

- S. W. Boettcher, E. L. Warren, M. C. Putnam, E. A. Santori, D. B. Turner-Evans, M. D. Kelzenberg, M. G. Walter, J. R. McKone, B. S. Brunschwig, H. A. Atwater, and N. S. Lewis. Photoelectrochemical Hydrogen Evolution Using Si Microwire Arrays. *Journal of the American Chemical Society*, 133(5),1216–1219, 2011.

- M. G. Walter, E. L. Warren, J. R. McKone, S. W. Boettcher, Qixi Mi, E. A. Santori, and N. S. Lewis. Solar water splitting cells. *Chemical Reviews*, 110(11), 6446–6473,

- E. L. Warren, S. W. Boettcher, M. G. Walter, H. A. Atwater, and N. S. Lewis. pH-Independent, 520 mV Open-Circuit Voltages of Si/Methyl Viologen$^{2+/+}$ Contacts

Through use of Radial n^+p-Si Junction Microwire Array Photoelectrodes. *The Journal of Physical Chemistry C*, 115(2), 594–598, 2010.

- E. L. Warren, S. W. Boettcher, J. R. McKone, and N. S. Lewis. Photoelectrochemical water splitting: silicon photocathodes for hydrogen evolution. *Proceedings of SPIE (7770)*, pp. 77701F–7, 2010.

- M. D. Kelzenberg, S. W. Boettcher, J. A. Petykiewicz, D. B. Turner-Evans, M. C. Putnam, E. L. Warren, J. M. Spurgeon, R. M. Briggs, N. S. Lewis, and H. A. Atwater. Enhanced absorption and carrier collection in Si Wire Arrays for Photovoltaic Applications. *Nature Materials*, 9(3), 239–244, 2010.

Other related publications:

- E. D. Kosten, E. L. Warren, and H. A. Atwater. Ray optical light trapping in silicon microwires: exceeding the $2n^2$ intensity limit. *Optics Express*, 19(4), 3316–3331, 2011.

- M. C. Putnam, S. W. Boettcher, M. D. Kelzenberg, D. B. Turner-Evans, J. M. Spurgeon, E. L. Warren, R. M. Briggs, N. S. Lewis, and H. A. Atwater. Si microwire-array solar cells. *Energy & Environmental Science*, 3, 1037–1041, 2010.

Chapter 1

Introduction

1.1 Solar energy conversion

Solar energy is the largest renewable energy resource on Earth. Radiation from the sun hits our planet at a rate of 1.76 x 10^5 TW (1 TW = 1 trillion joules per second). While not all of this energy can be easily captured in a form that is useful for humans, the accessible part of the solar energy resource still dwarfs that of wind, hydro, tidal, geothermal, biomass, and nuclear combined.[1] However, less than 1% of the utility scale electricity in the United States in 2011 was generated from solar power, due to the high cost of solar technologies relative to fossil fuels.[2] If solar energy is going to compete with energy generated from fossil fuels, the challenge is to develop technologies that can convert, store, and distribute solar energy in a cost-effective and environmentally benign way.[3]

Light can be converted into useful energy in several different ways, including solar thermal conversion, photovoltaics, photosynthesis, and photoelectrochemistry. Solar thermal systems use incident photons to create a temperature gradient which can be used to power an engine directly (a Stirling engine) or to drive a process fluid through a turbine to produce electricity.[4] Photovoltaic systems convert sunlight directly into electricity by controlling the separation of charges that are created when a photon is absorbed by a semiconductor. Photosynthesis, which supplies most of the energy used by life on our planet, uses photogenerated charges to create new chemical bonds which can be stored as fuels. Photoelectrochemical systems combine the principles of photovoltaics and photosynthesis by absorbing light with a semiconductor but transporting the energy by making and breaking chemical bonds rather then moving electrons through a circuit. Photoelectrochemical cells can be used directly to produce electricity or can be designed to create a chemical fuel.[5]

Solar radiation can only be captured when the sun is shining, so a storage system is needed to provide a continuous, stable energy supply. The first two technologies discussed above are unable to provide electricity at night without the use of expensive storage technology such as batteries or flywheels. Storing solar energy in chemical bonds is an attractive solution, but natural photosynthesis has very low overall efficiency; plants convert photons into useable biomass at a rate equivalent to less than 1 W m^{-2}.[3] Photoelectrochemistry has the potential to fill this void by using stable inorganic materials for the direct production of chemical fuels. Although there are several potential systems that can be used for photoelectrochemical energy generation, the photo-electrolysis of water to produce hydrogen and oxygen remains the holy grail of scientific research in this field.[6] In such a system, semiconductor electrodes use photogenerated carriers to reduce water to hydrogen at the photocathode and oxidize water at the photoanode.

1.2 Requirements for a solar fuel system

A true "artificial photosynthesis" device must be able to simultaneously drive the water oxidation and hydrogen evolution reactions without any assistance (either electrical bias or sacrificial reagents). The free energy change for the conversion of one molecule of H_2O to H_2 and $\frac{1}{2}$ O_2 under standard conditions is Δ G = 237.2 kJ mol^{-1}, which corresponds to Δ E = 1.23 V per electron transferred. To use a single semiconductor and drive this reaction with light, the semiconductor must absorb radiant light with photon energies of $>$ 1.23 eV ($\lambda < 1000$ nm) and convert the energy into H_2 and O_2. This process must generate two electron-hole pairs per molecule of H_2 (2 x 1.23 eV = 2.46 eV) and four electron-hole pairs per molecule of O_2 (4 x 1.23 eV = 4.92 eV). Theoretically, a single semiconductor material having a band gap energy (E_g) large enough to split water (1.23 eV) and the correct band edge positions could simultaneously drive the hydrogen evolution reaction (HER) and oxygen evolution reaction (OER) using photogenerated electrons and holes. However, in a real system, there are additional over-potential losses due to concentration gradients in the solution and kinetic limitations of catalysts to drive the fuel-forming reactions. These losses depend on the semiconductor material, device geometry and the catalyst material. When combining these over-potential losses with the energy lost due to thermalization of absorbed photons to the band edge, the total energy loss is expected to be $\sim$0.8 eV per photon, making the true bandgap requirement to drive water electrolysis 1.6–2.4 eV.

There are two approaches to calculate the maximum theoretical conversion efficiency for semiconductor-based water splitting devices. In the ideal limit, the conversion efficiency is calculated based only on the number of absorbed photons and the bandgap of the semiconductor. For a single semiconductor absorber with a bandgap of 1.6 eV and requiring two photons to produce one molecule of H_2 (classified as S2) the ideal limit on conversion efficiency is 30.7%.[7] Another approach is to combine two semiconductor absorbers in series, to more effectively utilize the solar spectrum (Fig. 1.1A). By optimizing the combination of absorption profiles it is possible to achieve an ideal theoretical efficiency of 46% with a tandem absorber system (Fig. 1.1B).[7] However, if the absorbers are connected in series (current matched), the ideal system has a top layer with a band gap of 1.7 eV (730 nm) and the bottom layer at 1.1 eV (1120 nm) for an ideal theoretical efficiency of 41%. Such a system can be classified D4, which indicates a system that requires four photons to produce one molecule of H_2.

To calculate a more realistic chemical conversion efficiency, the overpotential losses discussed above must be added. The chemical conversion limit for an D4 system (assuming a loss of 0.8 eV per photon) is 27.1%, while that for an S2 system is only 17.4% (for a 2.0 eV bandgap material). While there are no ideal materials for the S2 system or the wide band-gap absorber for the D4 system, Si has the correct bandgap and band energetics to serve as the bottom of the D4 system. Although many new materials are being investigated, one candidate photoanode material to integrate with Si is tungsten oxide (WO_3, $E_g = 2.7$ eV).[8] The complementary absorption characteristics of Si and WO_3 are shown in Fig. 1.1.

In addition to exhibiting an optimal band gap for solar absorption, semiconductor photoelectrodes must exhibit excellent oxidative/reductive stability in contact with aqueous electrolyte solutions. For thermodynamic stability, a semiconductors reductive and oxidative decomposition potentials must be more negative than the semiconductors conduction band-edge for water reduction or more positive than the semiconductor valence band-edge potential for water oxidation, respectively. Very few semiconductor materials exhibit the necessary requirements for electrode stability in aqueous electrolyte solutions simultaneously for both water oxidation and reduction.[9]

One of the motivations for developing standalone water-splitting devices is the potential to keep the system costs competitive with the alternative of using photovoltaic (PV) modules connected directly to electrolyzers and/or catalytic electrodes. Current estimates predict

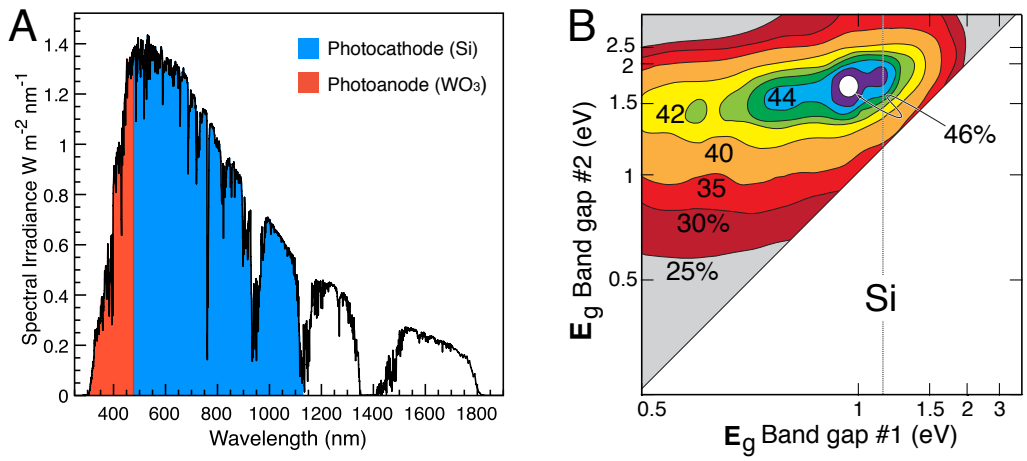

Figure 1.1. A) Solar spectrum with the absorption for a Si photocathode (blue) and a WO_3 photoanode (red). B) Contour diagram for ideal limiting efficiencies for a dual-bandgap absorber system, with the Si bandgap shown on the bottom. The two absorbers are optimized separately, and the efficiencies do not account for any energy losses to drive a fuel forming reaction.[7]

that at an electricity cost of \$0.043/kWh, the cost to produce H_2 will be $\sim$ \$3.00/kg.[10] Using the current cost of utility-scale solar systems (\$0.15/kWh as of March 2012), H_2 costs would rise to over \$7.00/kg, and this estimate does not account for the need to scale the system to match the peak solar flux which would drive the price even higher.[11] Water-splitting cells with direct semiconductor/liquid contacts are attractive because they have the potential to avoid significant fabrication and systems costs involved with the use of separate PV systems and electrolyzers. However, many challenges remain, both in the development of materials for sustained solar-driven water-splitting, and in the engineering of a deployable system. It is not clear how the constraints imposed on the band energetics of the materials and the need to physically capture product gases will affect the practical conversion efficiency and cost of a solar-fuel system. The development of a working prototype will help to answer these questions.

1.2.1 Calculating practical device efficiencies

For a system capable of generating the full potential needed to drive water-splitting, the solar-to-hydrogen conversion efficiency (η_{STH}) can be calculated by taking the ratio of the chemical power produced (the product of the operating current, J_{op} and the potential required to drive the reaction, 1.23 V) and the illumination power density using Eq. 1.1a. If any additional bias is applied to the cell, the efficiency must be calculated with Eq. 1.1b,

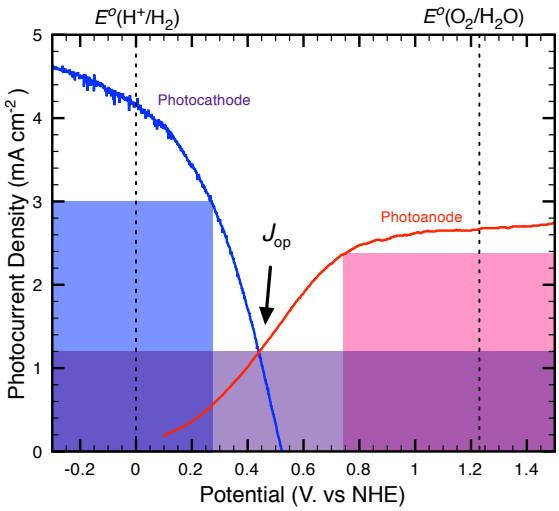

Figure 1.2. Overlaid $J - E$ data for a photoanode and photocathode. The system will operate at a current density where the two curves intersect.[8]

where V_{app} is the potential applied to the system.[12]

$$\eta_{STH} = \frac{J_{op} \cdot (1.23V)}{P_{in}} \tag{1.1a}$$

$$\eta_{STH,assisted} = \frac{J_{op} \cdot (1.23V - V_{app})}{P_{in}} \tag{1.1b}$$

The solar conversion efficiency of individual candidate photoelectrode materials that might be used in a multiple band gap photoelectrolysis cell to drive either the HER or OER can be calculated from current-voltage data obtained using a potentiostat in an illuminated three-electrode cell. It is useful to calculate efficiencies of a photoanode or photocathode separate from the other half of the water splitting reaction as they allow for optimization of materials independently. It is important to recognize that the photoelectrode efficiencies calculated by characterizing individual photoelectrodes based on the power they produce represent only a portion of the Gibbs free energy needed to drive the overall water-splitting reaction, with the rest of the energy being provided by a potentiostat.[13, 14]

Therefore, the open-circuit voltage (V_{oc}) and short-circuit current density (J_{sc}) are referenced to the thermodynamic potential of the water splitting reactions (H^+/H_2, O_2/H_2O) at the experimental pH. The calculation of individual photocathode conversion efficiency is discussed in more detail in Chapter 5.2.

By independently characterizing photoanodes and photocathodes, the expected performance of an integrated system with no external electronics can be directly calculated. Overall water splitting efficiencies for photoelectrolysis cells can be estimated by overlapping the individually tested $J-E$ data for each photocathode/anode (Fig.1.2).[15, 16] The intersection of the two curves indicates the maximum operating current density (J_{op}) for the complete cell, which can then be used to calculate the overall device efficiency from Eq. 1.1.

1.2.2 Photocathodes for hydrogen evolution

Photocathodes used for a water splitting cell need to supply sufficient cathodic current to reduce protons to H_2 and must be stable in aqueous environments. In addition, to successfully reduce protons to H_2, the conduction band edge of the photocathode must be more negative than the hydrogen redox potential. The mechanism for the HER is pH dependent: at low pH the HER proceeds primarily by the reduction of protons, whereas at high pH, water is primarily reduced to produce hydroxide ions.[17] The overall reactions are shown in Eqs. 1.2a and b.

$$2H^+ + 2e^- \rightarrow H_2 \text{ in acid} \tag{1.2a}$$

$$2H_2O + 2e^- \rightarrow H_2 + 2OH^- \text{ in base} \tag{1.2b}$$

When a semiconductor brought into contact with a liquid electrolyte phase, the Fermi level will equilibrate with the electrochemical potential (E_{redox}) of the liquid by transferring charge across the interface. For a p-type semiconductor, the bands bend in such a way that photogenerated electrons are driven toward the interface, while holes are swept into the bulk of the solid. Photoexcitation thus injects electrons from the solid into solution. This cathodic current may, to some extent, protect the surface of the semiconductor from oxidation. For this reason, p-type semiconductors can be expected to be more stable than their n-type counterparts, which have a tendency to photo corrode when photogenerated holes are generated near the interface. Several p-type semiconductors have been investigated as photocathodes for the HER, including GaP, InP [18], $GaInP_2$ [19], and Si [20, 21].

1.2.3 Coupling catalysts to photocathodes

Many materials (including Si) that are potentially useful as photocathodes for the HER do not have surfaces that are sufficiently electrocatalytic to support light-driven H_2 evolution without a large additional electrical bias. Overcoming this kinetic limitation requires a stronger driving force, i.e., an overpotential, to drive the desired chemical reaction. In turn, the overpotential lowers the usable voltage output, and hence lowers the efficiency of the photocathode.[22] Addition of a catalyst to the surface (often in the form of a nanoparticulate metal film) can improve the kinetics of the reaction.[23] However, the introduction of a metal at the semiconductor-liquid junction can also affect the band-bending energetics of the junction, affecting the driving force for the desired reaction (this issue will be discussed further in Chapter 8).

An ideal HER catalyst would be able to produce H_2 at low overpotential at a rate equal to the photo-generation rate in the semiconductor, and must also meet the same stability requirements as the semiconductor materials in the system. The HER is one of the most well-studied electrochemical reactions and many catalyst materials have been investigated for water-electrolysis systems.[24] For most catalysts, the reaction involves the creation of a metal-hydride bond (M-H), and maximum HER activity is observed in metals with intermediate bond strengths (noble metals such as Pt, Pd, and Ir have the highest activities, while Ni is the most active non-precious metal).[25] In this work we will investigate the Ni–Mo alloy as an alternative, earth-abundant catalyst which has shown potential as a stable catalyst in electrolyzer systems.[26]

1.3 Motivation for Si microwires

In a solar cell, incident photons with energy greater than the semiconductor band-gap generate excited electron-hole pairs that are collected as electric current (uncollected carriers recombine to produce heat). This is traditionally done by creating an electric field near the surface of the semiconductor that separates oppositely charged carriers. Any carriers generated far from this junction must diffuse until they reach the junction and can be collected. The distance a photo-excited carrier can travel before it recombines is called the minority carrier diffusion length (L_n for p-type materials and L_p for n-type). In traditional planar semiconductor junctions, the directions of light absorption and charge-carrier collection are

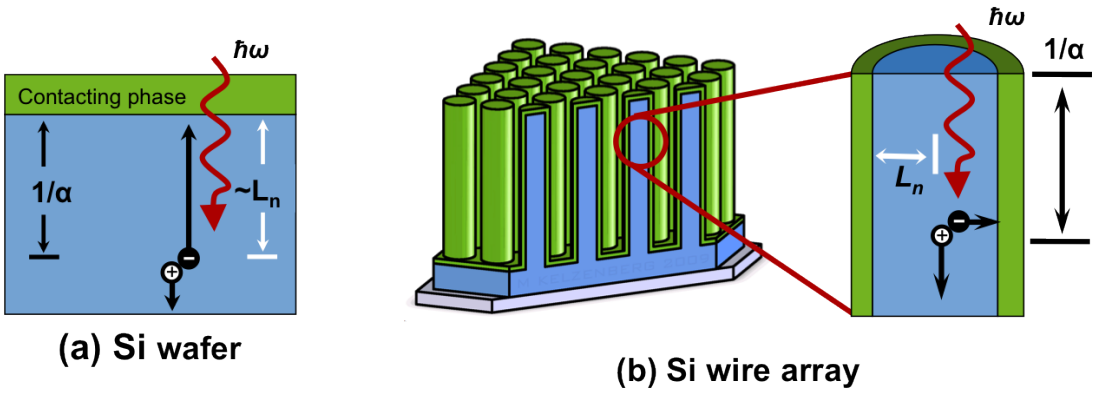

Figure 1.3. a) Schematic of a planar solar energy conversion device, which requires long diffusion lengths to collect photons absorbed far from the surface. b) Schematic of Si microwire array, where carriers only have to diffuse the radius of the wire before being collected at the junction. (Image credit: M. Kelzenberg)

the same, as shown in Fig 1.3a.

Planar crystalline Si (c-Si) and multi-crystalline (mc-Si) solar cells currently dominate the photovoltaics market, but the high cost of Si production and processing currently prevent Si-based PV from competing with utility-scale energy generation.[27] A significant part of this cost comes from the energy-intensive purification processes needed to produce the high-quality, long diffusion length material needed for solar cells. While the bandgap of Si (1.1 eV) is well matched to the solar spectrum, the fact that Si is an indirect absorber means a 100 μm penetration depth (also referred to as optical thickness, $1/\alpha$) is needed to absorb 90% of the solar spectrum. Hence, the diffusion length in a planar Si solar cell must long enough to collect carriers generated far from the junction.[28]

1.3.1 Radial geometry

In a radial geometry, the directions of light absorption and carrier diffusion are decoupled, which allows material with lower diffusion lengths to effectively capture all photogenerated carriers (Fig. 1.3b). The photo-excited carriers generated within the wire only have to diffuse the radius of the wire before they can be collected at the surface. A theoretical study of this geometry demonstrated that a radial wire-based devices can out-perform planar Si solar cells for material with short minority carrier diffusion length (assuming low recombination rates at the surface and in the depletion-region).[28] This study provided an important design rule for radial-junction solar cells: maximum efficiency is achieved when the radius of the wire is approximately equal to the minority carrier diffusion length. If

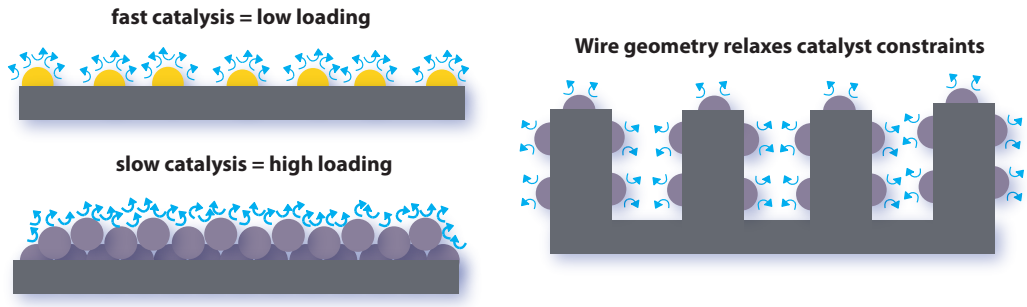

Figure 1.4. Left: Comparison of catalyst loading required for a fast and slow catalyst on a planar substrate. Right: A highly structured substrate allows the same catalyst loading, but without blocking all of the incident light from being absorbed by the semiconductor.

the radius is too small, surface and junction recombination begin to degrade the device performance, while if the radius is $>> L_n$ not all carriers will be collected. Equation 1.3 shows a modified form of the diode equation that can be used to account for the effect of increased surface area on device performance:

$$V_{oc} = \frac{nk_BT}{q} ln(\frac{J_{ph}}{\gamma J_o}) \tag{1.3}$$

where V_{oc} is the open circuit voltage, n is the diode quality factor, k_B is Boltzmanns constant, T is the temperature (in Kelvin), q is the (unsigned) charge on an electron, J_{ph} is the photocurrent density, J_o is the exchange current density, and γ is the ratio of the actual junction area to the projected surface area of the electrode, i.e., the roughness factor.[28] For narrow, closely packed wire arrays, the total surface area, and therefore γ, will be very large, increasing the dark current which ultimately will decrease the material's efficiency for solar energy conversion. Prior work has demonstrated minority carrier diffusion lengths $>$ 10 μm for un-passivated wires and $>$ 50 μm for wires passivated with SiN_x, which motivates the investigation of wires with diameters on the scale of microns.[29, 30]

Another advantage of the microwire geometry is that the enhanced surface relative to the projected area increases the available catalytic area and decreases the current density at each point on the surface. Both of these factors should enable earth-abundant catalysts to compete with noble metal catalysts to drive photoelectrochemical fuel forming reactions. On a planar substrate, to get the same catalytic performance out of a "slow" catalyst

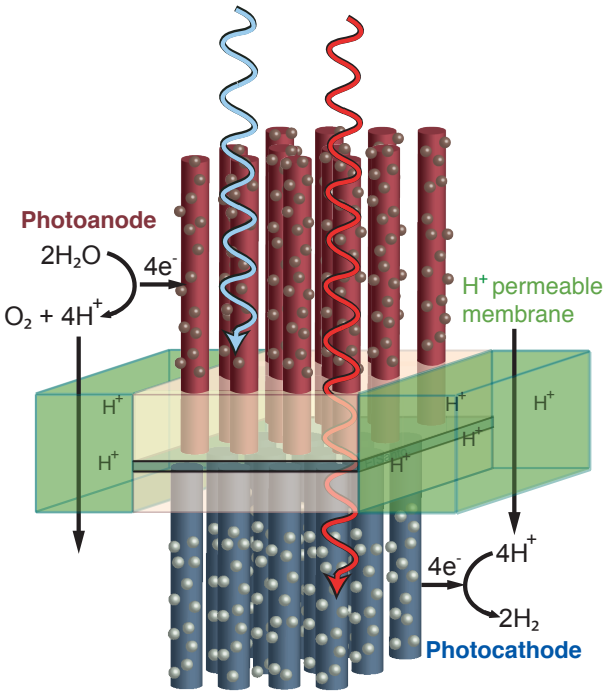

Figure 1.5. One proposed schematic of a membrane-based water splitting prototype design with microstructured semiconductor photoanode and photocathode materials decorated with OER and HER catalysts, respectively. (Image credit: E. A. Santori)

material, one would need to increase the catalyst loading which would block the light from getting absorbed in the semiconductor (left of Fig. 1.4). However, on a highly structured surface, the same catalyst loading can be achieved without blocking all of the light (right of Fig. 1.4).

1.3.2 Designing an artificial photosynthesis device

While there are many potential design prototypes for an artificial photosynthesis device, one design that has attracted a great deal of interest is a membrane-based system with tandem, microstructured, semiconductor absorbers. The schematic shown in Fig. 1.5 consists of earth-abundant photoanode and photocathode semiconductor absorbers, consist of high aspect ratio semiconductor components, with attached heterogeneous multi-electron transfer catalysts, that are needed to drive the oxidation or reduction reactions at low overpotentials. The high aspect-ratio semiconductor rod electrode architecture allows for the use of low-cost, earth-abundant materials without sacrificing energy conversion efficiency, due to the orthogonalization of light absorption and charge-carrier collection. As discussed above,

the high surface-area design of the rod-based semiconductor array inherently lowers the flux of charge carriers over the rod array surface relative to the projected geometric surface of the photoelectrode, thus lowering the photocurrent density at the solid/liquid junction, and allowing higher catalyst loading without blocking light absorption by the semiconductor.

1.4 Overview

The following chapters of this thesis will discuss the fabrication and characterization of Si MW energy conversion devices. Chapter 2 will overview the fabrication and growth of Si MW arrays, as well as prior work on their development as energy conversion materials. Chapter 3 focuses on the use of regenerative photoelectrochemistry to characterize the material quality of Si MW arrays and different processing steps used in the creation of energy conversion devices. Chapter 4 will discuss how the introduction of a n^+p junction affects the band energetics in of Si in an aqueous environment. Chapter 5 introduces the use of SiMW arrays as photocathodes to drive the hydrogen evolution reaction and then Chapter 6 will discuss the development of all earth-abundant photocathode systems consisting of n^+p-SiMW arrays coated with Ni–Mo catalysts. Chapter 7 focuses on the development of inexpensive fabrication techniques to improve the scalability of manufacturing Si MW arrays. Chapter 8 takes a slightly different direction and addresses preliminary investigations of the band energetics of semiconductor/catalyst interfaces. The final chapter will discuss future directions for all of the projects.

Chapter 2

VLS Si microwire arrays

The investigation of non-planar semiconductors as solar absorbers is not a new concept. Several different geometries have been proposed to decouple the requirements for light absorption and carrier extraction in photovoltaic materials.[31, 32] The foundation for the current research effort at Caltech has been built upon the early modeling work by Kayes et al. and a resurgence of interest by the material research community in the growth of one-dimensional nanostructures.[28] The experimental techniques used to fabricate and process arrays of vertically oriented wire arrays have been developed and refined by several generations of researchers at Caltech, and are only briefly summarized here. More detail is available in prior publications and dissertations.[30, 33–35]

2.1 The vapor-liquid-solid growth process

One-dimensional crystalline Si wires can be grown from gaseous precursors using the vapor-liquid-solid (VLS) growth process, a chemical vapor deposition (CVD) technique first reported in 1964 by Wagner and Ellis.[36] Wires ranging in diameter from nm to mm have been grown with this technique, with the size of the wire determined by the amount of metal catalyst used. Although VLS growth was first reported using Au as the metal catalyst, a variety of other metals have also been used to catalyze this growth process. At Caltech, Cu, Ni, Al have been successfully used to grow Si MWs from $SiCl_4$. Other research groups have used: Ag, Bi, Cd, Co Dy, Fe, Ga, Gd, In, Mg, Mn, Os, Pb, Pd, Pr, Pt, Ru, Sn, Te, Ti, and Zn to grow from SiH_4 or Si_2H_6 precursors.[37, 38]

During VLS growth, the growth substrate is heated to a temperature above the eutectic temperature for the metal/Si system, creating a liquid catalyst droplet. Gaseous precursors

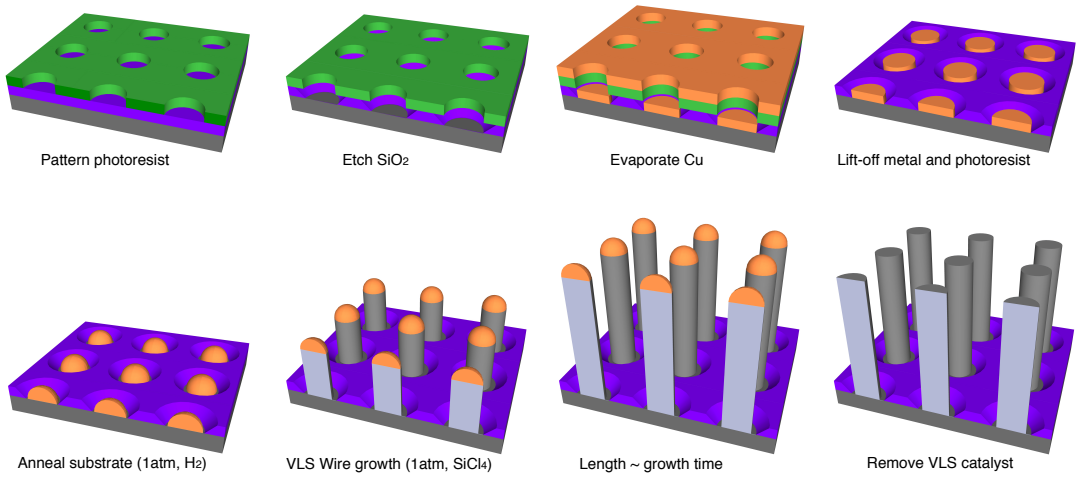

Figure 2.1. Schematic of fabrication steps used to fabricate vertically–oriented arrays of VLS Si MWs

($SiCl_4$ and small amounts of dopant such as BCl_3 or PH_3) are introduced to the reactor and decompose on the catalyst surface, super-saturating the eutectic mixture. The growth substrate provides a nucleation site for the Si to precipitate as an epitaxial crystal. The (111) crystal orientation is the preferred direction of growth, so by using a (111) oriented substrate, this process results in the formation of a wire of Si growing perpendicular to the substrate.

All of the devices discussed in this thesis are grown using Cu as the VLS catalyst. Studies on the effects of intentionally contaminating Si with different metals have shown that Si solar cells are much more tolerant of Cu impurities than any other methods.[39] In Si, Cu has a preferential interaction with B dopants, and has been shown to segregate into highly doped p-type regions of Si.[40] Growing lightly doped p-type wires on heavily doped p-type substrates, may help minimize the metal contamination in the photoactive region of the material.

2.2 Fabrication of substrates and wire growth

A process for the growth of patterned, vertically oriented arrays of Si microwire arrays was developed by Brendan Kayes et al.[31, 34] Two additional VLS reactors of different sizes and configurations have since been built, and while the flow rates and temperatures vary slightly from system to system, the basic procedure has proven to be very robust. The basic procedure for substrate preparation and growth is shown in the schematic in Fig. 2.1.

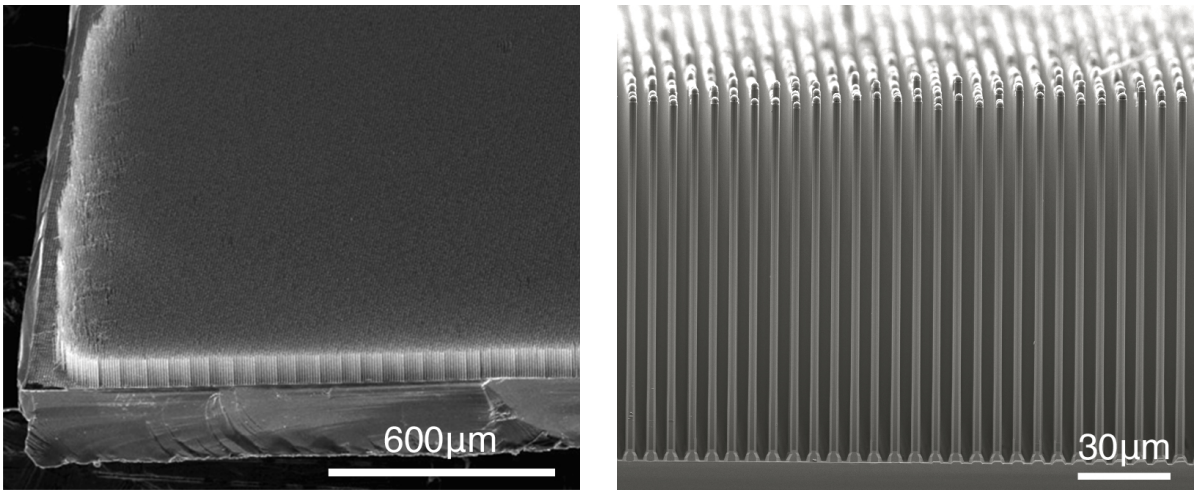

Figure 2.2. SEM images of VLS Si MW arrays grown from Cu and $SiCl_4$

Substrate preparation.

To produce substrates for the controlled growth of patterned p-type Si MWs, degenerately doped p-type (111)-oriented Si wafers with a resistivity of $\rho < 0.003$ Ω-cm and coated with 350–500 nm of thermally grown SiO_2 were patterned using standard photolithographic methods. (Degenerately doped, non-photoactive wafers were used to ensure the substrate does not contribute to photocurrents measured from these devices. The high doping also provided an ohmic back contact to the wires.) A positive photoresist layer (Shipley 1813, Microchem) was deposited on the oxide, with the photoresist exposed to produce an array of holes in the photoresist. The standard pattern used was an array of 3 μm diameter circulars, packed in a square or hexagonal array with a hole-to-hole pitch of 7 μm. The SiO_2 exposed through the holes in the photoresist layer was etched to expose the underlying Si substrate using buffered HF. 400–600 nm of Cu (EPSI 6N) was then thermally evaporated onto the substrate, and the excess metal and photoresist were removed by lifting-off in acetone. The wafer was then cut into smaller pieces before growth - the exact size determined by that of the reactor.

Wire growth. Si MW arrays were then grown by the VLS growth method, by annealing the samples in a H_2 atmosphere at 1000°C for 20–25 min, followed by exposure to flowing $SiCl_4$ (Strem, 6N) saturated in He or H_2 , BCl_3 (0.25% in H_2), and H_2, into the reaction chamber at a ratio of approximately 50:0.5–2:500. The length of the wires was controlled

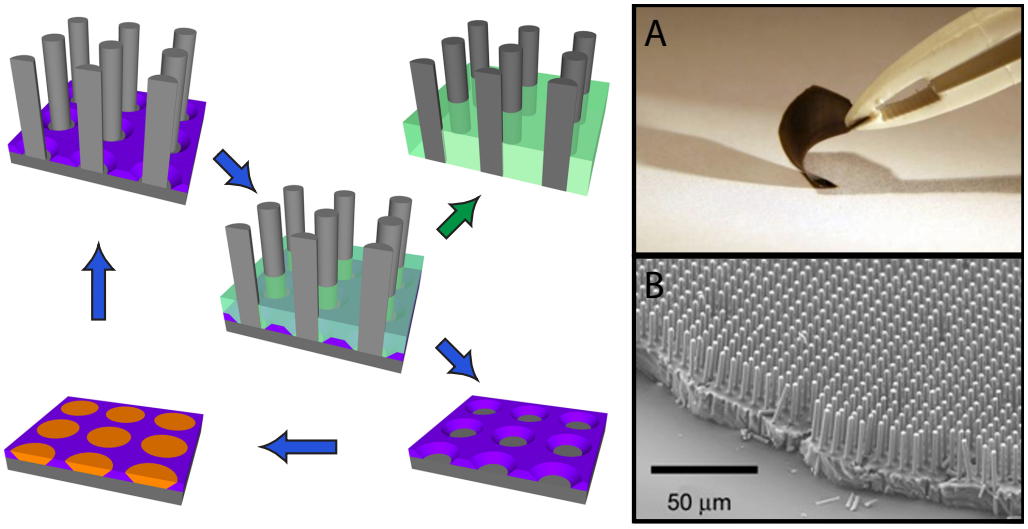

Figure 2.3. Schematic of peeling polymer-embedded Si MW arrays and reusing the growth substrate. A shows a photograph of a flexible polymer-embedded wire array and B shows an SEM image of a similar array.[43]

by the growth time as well as by the position of the substrate in the reactor. After wire growth, the samples were cooled to ∼600 °C under H_2, then cooled to room temperature under N_2 or He at ambient pressure, and removed from the reactor.

Catalyst removal.

After growth the VLS growth catalyst is removed from the tips of the wires using a RCA2 etch (5:1:1 H_2O: HCl:H_2O_2 at 70 °C). Etching for 20–30 minutes in a 20 wt% $FeCl_3$ solution was investigated as an alternative [41], but the potential impact of Fe contamination on subsequent processing steps prevented the wide-spread adoption of this etching technique.[39] The remaining impurities in the wire arrays were investigated by Putnam et al. using nano-scale secondary ion mass spectroscopy (nano-SIMS), which indicated that there was a thin region on the edge of the wire that was heavily contaminated with metal.[42] To remove this layer, samples were etched for 20–30 s in 4 M KOH (aq) (semiconductor grade), and then rinsed with copious amounts of 18 MΩ-cm H_2O. If samples were to undergo further processing, a second 10–15 min RCA2 etch is performed.

2.3 Flexible, polymer-embedded wire arrays

The current VLS growth methodology requires an expensive Si wafer to serve as the epitaxial growth substrate, which would increase the manufacturing costs for Si MW energy

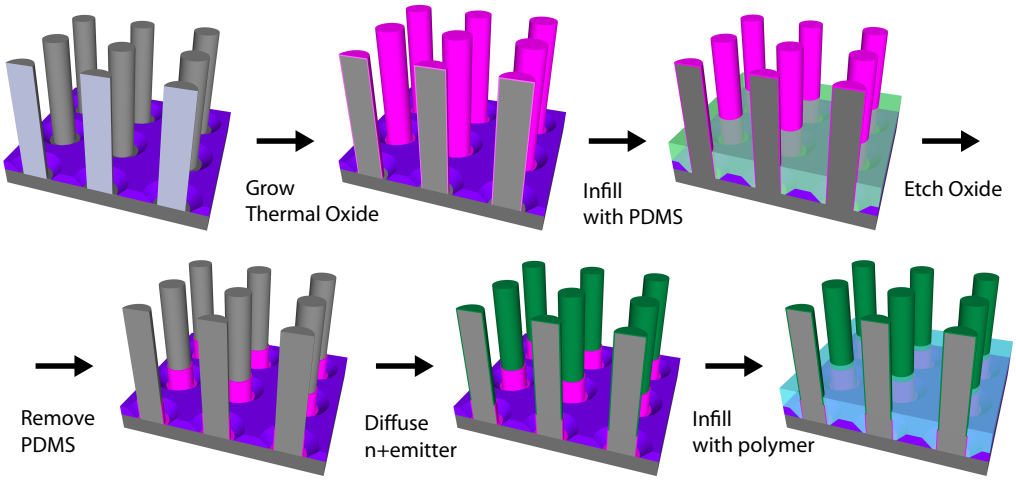

Figure 2.4. Schematic of fabrication steps used to fabricate radial p-n junctions in SiMW arrays

conversation devices. To address this issue, methods were developed to embed the wire arrays in a flexible polymer, such as PDMS (polydimethylsiloxane), and then physically peel the wire/PDMS membrane from the substrate using a razor blade.[43] It was also demonstrated that after removal of the wires, the original substrate could be reused to grow wires by selectively etching away the base of the wires, and then electrodepositing new VLS metal catalyst into the holes in the patterned SiO_2 (Fig. 2.3).[44]

2.4 Radial p-n junction Si microwire devices

2.4.1 Fabrication of solid-state p-n junction devices

To create a solid-state solar cell device, it is necessary to create a p-n junction to separate oppositely charged photo-excited carriers. A robust process was developed to control the junction area of the diffused n^+-emitter layer on the wires by use of an SiO_2 "boot" to protect the base of the wires and the substrate during the doping process. The process used to fabricate radial p-n junctions on the Si MW arrays is outlined in Fig. 2.4.

Oxidation. After the catalyst was removed from the wires as discussed in Section 2.2, a dry thermal oxide was grown over the surface of the wires. Oxidation at 1100°C for 2 hrs followed by a slow cool down produced a conformal SiO_2 diffusion barrier (170–200 nm) over the surface of the wire array.

PDMS infill. The wire arrays were then infilled with uncured PDMS by spin-coating the samples with a mixture of PDMS (10:1 Sylgard 184) and toluene. The height of the PDMS layer was controlled by varying the amount of toluene and spin speed. A ratio of 4:1 toluene:PDMS and 1500 rpm produced 10–20 μm thick layers of PDMS at the base of the wires. The PDMS was allowed to cure either on a hotplate at 150°C for 30 min, or in a vacuum oven at 80°C overnight. The SiO_2 was etched off the top of the wires using buffered HF, and then the PDMS was removed from the wires by etching in a mixture of tetrabutylammonium fluoride (TBAF) and 1-methyl-2-pyrrolidone (NMP) (3:1; v/v; NMP/ 75% TBAF in water).[45] A Piranha etch (4:1 H_2SO_4:H_2O_2) was used to remove any organic residue from the wires.

n^+-emitter formation. Emitter layers were formed by heating the Si substrates between solid CeP_2O_{14} doping wafers (Saint-Gobain, PH-900 PDS). The samples were annealed for 10–15 min at 850°C. On planar devices, this process produced a 100–150 nm-thick n^+ emitter layer that had a sheet resistance of 95–120 Ω sq^{-1}. The Si MW arrays were immersed for 30 s in buffered HF, to remove from the Si surface the P_2O_5 glass that formed during doping. The most consistent results were achieved when samples underwent a full RCA1 and RCA2 clean immediately prior to doping.

2.4.2 Characterization of solid-state p-n junction devices

Single-wire solar cells were fabricated by removing the wires from the growth substrate contacting each using photolithographic techniques (see Section 7.6.1). The photovoltaic performance, spectral response characteristics, and effect of surface passivation were investigated, and the champion devices (passivated with a SiN_x antireflective coating) had conversion efficiencies of 9.0% (AM 1.5G, 100 mW cm^{-2}).[30] Large area solar cells of vertically-aligned radial p-n junction were also fabricated. The first generation devices had solar conversion efficiencies of 3.81%, but the addition of a back reflector and scattering particles improved the efficiency to 7.9% (AM 1.5G, 100 mW cm^{-2}).[46]

Chapter 3

Regenerative photoelectrochemical characterization of Si MW arrays

3.1 Introduction

Many proposed next-generation photovoltaic and photoelectrochemical devices have complicated nano- and micro-structured architectures that are designed to simultaneously optimize carrier collection and light absorption.[28, 47] Characterization of the electrical properties of these highly structured materials can be challenging due to the difficulty of creating electrical contacts, as well as the need to decouple the properties of the contact from that of the semiconductor. Regenerative photoelectrochemistry is a powerful technique to characterize the electrical properties of such systems, providing a conformal liquid contact that can be ohmic or rectifying, depending on the system used.[48]

In a regenerative photoelectrochemical system, a redox couple (consisting of a donor/electron pair with rapid charge-transfer kinetics) is dissolved in a liquid electrolyte. The electrochemical potential, $E(\mathrm{A/A^-})$, i.e., the Fermi level, of the liquid phase is given by the Nernst equation:

$$E(A/A^-) = E^{o'}(A/A^-) + \frac{RT}{nF} ln\left(\frac{[A]}{[A^-]}\right) \tag{3.1}$$

where $E^o(\mathrm{A/A^-})$ is the formal potential of the redox couple $(\mathrm{A/A^-})$ under standard conditions, R is the ideal gas constant, T is temperature, n is the stoichiometric number of electrons involved in the reaction, F is Faraday's constant, and [A] and $[\mathrm{A^-}]$ are the concentrations of the oxidized and reduced form of the redox species, respectively.[49] When in contact, Fermi level of the semiconductor will equilibrate with that of the contacting liquid

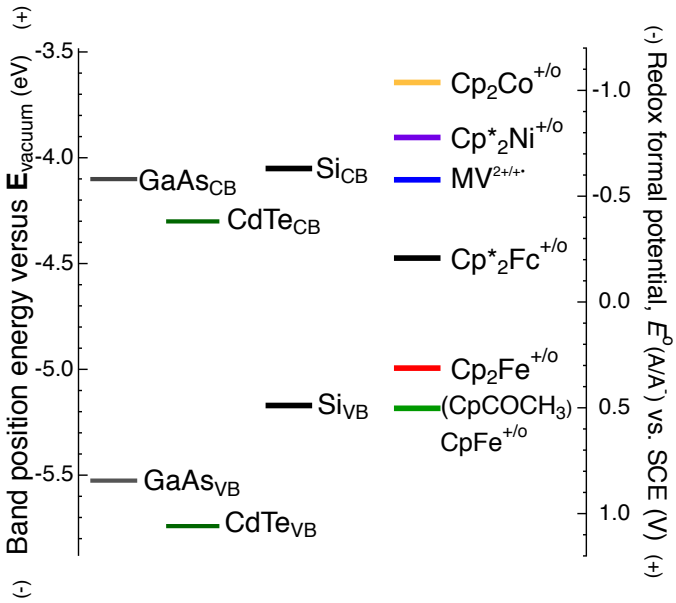

Figure 3.1. Energetics of different semiconductor band edges and redox couples [56]

phase, with most of the charge dropping across the semiconductor, inducing band bending within the semiconductor.[50] The barrier height of the resulting junction is given by the difference between the Fermi level of the semiconductor and the liquid phase. The choice of the redox couple and electrolyte system is based on the stability of the semiconductor and the desired barrier height of the system. Not all semiconductor-liquid systems exhibit stable, ideal diode behavior, but a variety of materials have been well characterized by electrochemical methods in the literature: Si [51, 52], InP [53], GaAs [54], CdX (X = Te, Se, S) [55]. Figure 3.2 shows the formal potentials of a variety of different redox couples that have been used to photoelectrochemically characterize semiconducting materials.[56]

3.1.1 Methyl viologen

Methyl viologen (N,N'-dimethyl-4,4'-bipyridinium dichloride, trade name Paraquat, abbreviated here as: $MV^{2+/+}$) is a one-electron, outer-sphere, redox couple that can be used in both aqueous and non-aqueous electrolytes. The first reduction of the MV^{2+} cation to $MV^{+\cdot}$ has a redox potential of -0.69 V vs. a saturated calomel reference electrode (SCE) and is highly reversible (Fig. 3.1). The $MV^{2+/+}$ redox system generally forms a high barrier height with p-type semiconductors, and forms an ohmic contact to n-type systems.[57] ($MV^{2+/+}$ can also be used to characterize n^+p diffused junctions, by serving as an ohmic

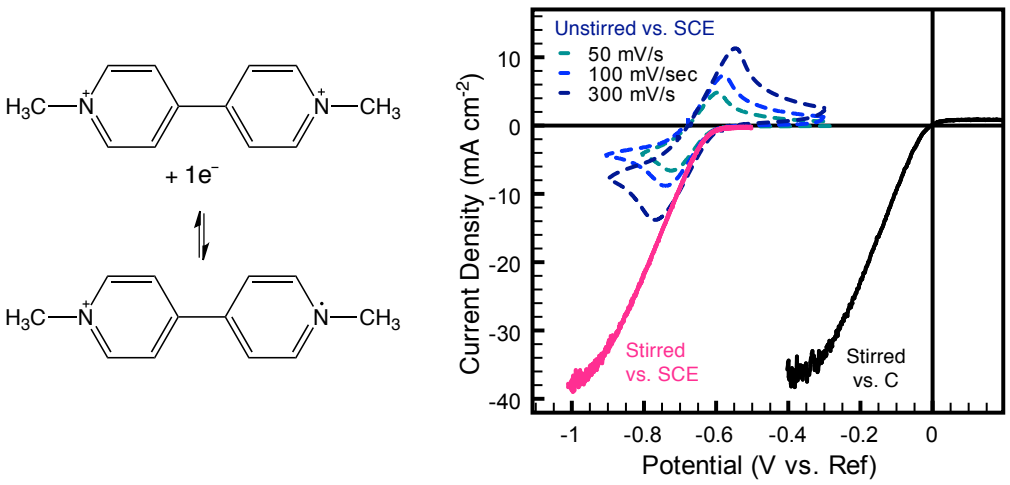

Figure 3.2. Left: Schematic of first reduction of the MV cation. Right: Cyclic voltammogram of a glassy carbon electrode in $MV^{2+/+}$ electrolyte: dashed = unstirred vs. SCE, pink = stirred vs. SCE (MV^{2+} only), black = stirred vs. a carbon cloth electrode (E_{sol} = -0.59V vs. SCE)

contact to the heavily n-type emitter layer). This redox couple has been used to look at the band energetics of functionalized Si surfaces [58, 59], to characterize porous Si [60], and investigate the performance of p-type GaP as a photocathode.[61] A second reversible reduction to MV^0 has been reported at potentials ranging from -1.1 to -1.35 V vs. SCE, but this reaction is complicated by the formation of $(MV^+)_2$ dimers and the fact that the MV^0 species formed at the electrode is insoluble.[62]

3.2 Experimental setup

The standard method for characterizing the photoelectrochemical performance of a semiconductor material in contact with a liquid redox couple is a 3-electrode setup controlled by a potentiostat. The semiconductor serves as the working electrode (WE), and the potentiostat controls the electrochemical potential of the WE relative to a reference electrode (RE), while measuring the amount of current passed between the WE and a counter electrode (CE). This 3-electrode arrangement is useful for isolating the the properties of the WE, and not indirectly measuring artifacts of the other circuit elements (resistance in the electrolyte, etc.).[49] For characterizing Si electrodes using the $MV^{2+/+}$ system, the standard electrolyte is a 0.1 M pH = 2.9–3.0 phthalate buffer with 0.5 M K_2SO_4 added as supporting electrolyte before the final pH adjustment.

Because the solution potential of a redox couple depends on the relative concentrations of the reduced and oxidized forms of the redox couple, both species must be present in the solution to extract stable photovoltage measurements. The reduced form $MV^{+\cdot}$ can be electrochemically generated in-situ to maintain a constant solution potential during experiments. One challenge in this experimental system is that the $MV^{+\cdot}$ species is highly absorbing at visible wavelengths, which makes it impossible to accurately measure the photovoltage of a semiconductor under broad spectrum illumination. The spectra of various laboratory light sources is compared to the air mass 1.5 global spectrum (AM 1.5G, the standard spectrum used for photovoltaic testing) on the left of Fig. 3.3. To balance the light absorption effects with concentration overpotential effects, a 50 mM concentration of $MV^{2+}Cl_2$ is used for most experimental applications. The absorbance for a 50 mM $MV^{2+/+}$ solution that has been reduced to various solution potentials (measured relative to SCE) is shown on the right of Fig. 3.3. At a solution potential of -0.6 V vs. SCE, the concentration of $MV^{+\cdot}$ is $\sim$ 3 mM, and has an absorbance greater than one across most of the visible spectrum. To obtain useful data from this system, monochromatic 808 nm illumination from a diode laser can be used to photoexcite Si devices through the highly absorbing $MV^{2+/+}$ solution.

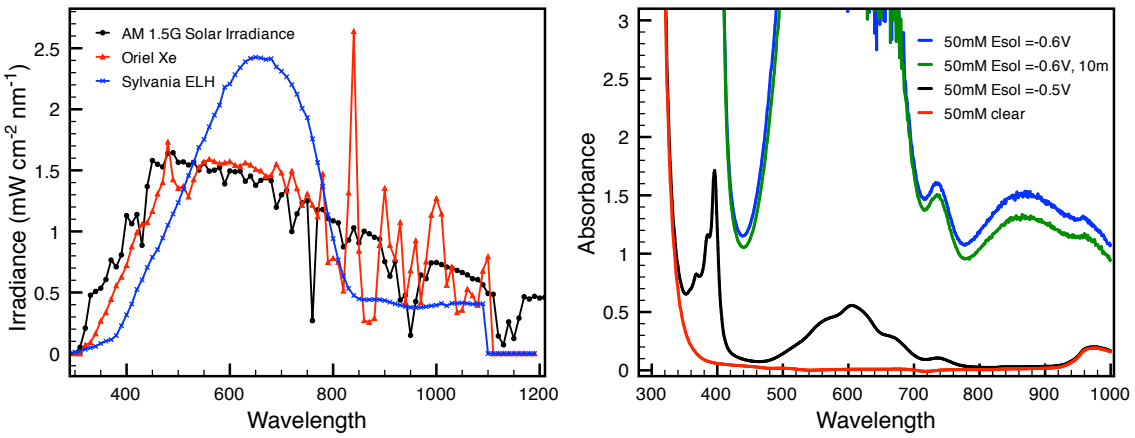

Figure 3.3. Left: Comparison of different broad-spectrum illumination sources used to characterize photovoltaic materials. Right: Absorbance data for a 50 mM $MV^{2+/+}$ solution before any $MV^{+\cdot}$ is generated (red), after being reduced to -0.5 V vs SCE (black), and after being reduced to -0.6 V vs SCE (blue). The green data were collected 10 minutes the blue curve, showing that the solution composition is quite stable in the ambient environment over time scales relevant to experimental testing.

3.2.1 Methyl viologen cell set-up

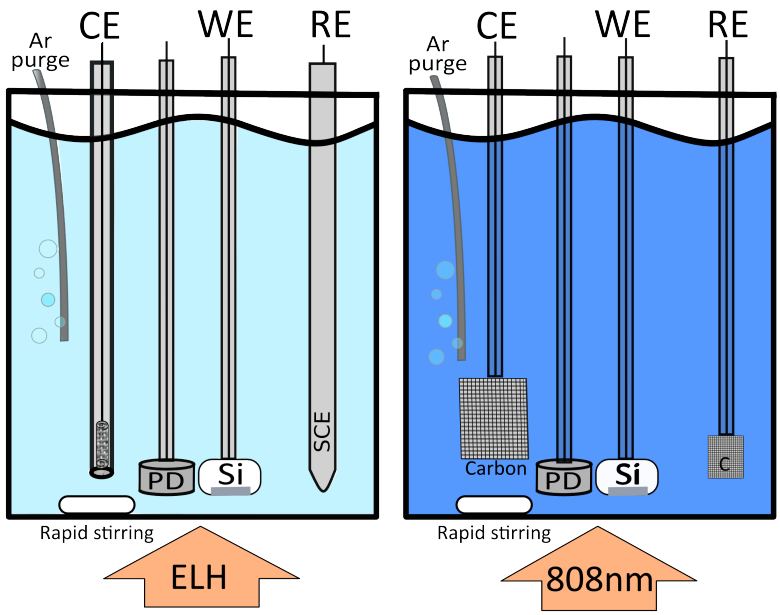

Figure 3.4. Schematic of $MV^{2+/+}$ photoelectrochemical cell. Left: With only MV^{2+} in solution, the solution is not highly absorbing so simulated solar illumination can be used. An SCE is used as the reference electrode because the solution potential is not well defined. Because there is only a tiny amount of the reduced species available to be oxidized in the "clear" electrolyte, the counter electrode is a Pt mesh inside a fritted compartment, which can maintain charge neutrality by oxidizing water. Right: After generation of the $MV^{+\cdot}$ species, carbon cloth electrodes are used as the counter and reference electrodes.

The methyl viologen cell can be operated with both forms of the redox couple present by using 60 mW cm^{-2} of 808 nm illumination to approximate the photon flux from AM 1.5G illumination. The system can also be operated under "clear" conditions (without generating any of the reduced $MV^{+\cdot}$ species) to confirm short-circuit behavior of a semiconductor electrode using simulated broad-spectrum sunlight. To monitor the illumination intensity incident onto the sample, a photodiode was placed in the solution at a height parallel to that of the sample (PD in Fig. 3.4). To avoid oxygen contamination, the system is continuously purged with high-purity Ar, which was run through an H_2O bubbler upstream of the cell. To minimize mass-transport effects, the solution was stirred vigorously. The best results were achieved using a magnetic train motor coupled to a diametrically magnetized neodymium ring magnet to drive a PTFE coated stir-bar inside the cell. Especially in wire arrays, rapid stirring is important, because high local concentrations of $MV^{+\cdot}$ can lead to further

reduction reactions that can complicate interpretation of cyclic voltammograms.[60]

When running the an electrochemical reduction reaction without generating the $MV^{+\cdot}$ species in-situ, a well-defined reference electrode, such as an SCE must be used, since the solution potential will not be well-defined by the Nernst equation. Since there is very little of the reduced species in solution, a Pt-mesh, separated from the bulk solution by a ground-glass frit, serves as the counter electrode, where it can satisfy the requirement of charge neutrality by oxidizing $MV^{+\cdot}$ or producing O_2.

Data collected in "clear" $MV^{2+/+}$ can be used to verify the current densities measured with both forms of the redox couple present. If the WE and PD are not properly aligned with the illumination source or the stir-motor is positioned too close to the WE or PD, the PD may not accurately measure the light hitting the sample, leading to erroneous current density measurements. Careful calibration of the electrode positions and illumination intensity are required to generate meaningful data with this experimental setup.

To generate the reduced species in-situ, a large (2–5 cm^2) carbon cloth electrode was used as the WE, and was held at a potential between -0.6 and -0.7 V vs. SCE (CE = Pt through frit) until the desired solution potential was attained. The solution potential was measured relative to SCE using a second small carbon cloth reference electrode.

3.2.2 Electrode fabrication

To fabricate electrodes for photoelectrochemical testing, Si MW array samples were either cut directly into electrodes (with areas 0.02–0.10 cm^{-2}) or were peeled from the substrate before use. Back contacts were made to the on-substrate wire samples using Ga/In eutectic to contact the degenerately doped Si substrates. To protect wire array samples from breaking during back contact formation, the front edges of the electrode chip were isolated with epoxy and allowed to dry before scratching the back of the substrate. For planar samples, 100 nm of Al was deposited on the back of the sample, and the wafer was then annealed under forming gas at 800°C for 10 min, to create a p^+ back surface field. All electrodes were mounted onto coiled wire using Ag paint, and were sealed into a glass tube using insulating epoxy (Loctite 9460 and/or Hysol 1C).

Carbon cloth electrodes were fabricated to serve as the reference and counter electrodes. The carbon cloth was cut into small squares and directly attached to a small piece of Pt wire in one corner. This junction was covered in Hysol 1C epoxy to prevent any liquid-to-metal

contact. After the epoxy dried, the Pt wire was soldered onto a longer Cu/Sn wire, and the whole assembly was epoxied into a glass tube or protected from solution using heat-shrink tubing.

3.2.3 Photoelectrochemical data collection

Electrodes were dipped in buffered or 10% HF to remove native oxide layers before electrochemical testing. Data was collected in a 3-electrode configuration using a small carbon RE and a large carbon CE and a Princeton Applied Research 273 Potentiostat. The solution potential was constantly monitored by measuring the carbon RE vs. an SCE in solution, and maintained between -0.59 and -0.60 V vs. SCE. The potential was periodically readjusted by re-reducing the solution as described above. The illumination was also continuously monitored and adjusted before data collection to control the amount of light hitting the WE. Cyclic voltammetry data was collected at a rate of 20–30 mV s^{-1}.

3.2.4 Correction for series resistance and concentration overpotential

Although the experimental setup described here allows for the rapid screening of multiple semiconductor samples, the geometry of the cell (Fig. 3.4) introduced a dependence of the measured electrical performance on the mass transport of the redox species through the liquid electrolyte. These mass transport effects create concentration over-potential losses in the cell. These losses, along with series resistance losses in the electrolyte, decrease the apparent performance of the photoelectrode relative to its true performance. Standard electrochemical methods allow for the correction of these artifacts to isolate the performance of the semiconductor, and thus provide a more accurate measurement of how the material would behave in a photovoltaic system.[63]

$$\eta_{conc} = \frac{k_B T}{nq}\left[ln\left(\frac{J_{l,a}}{-J_{l,c}}\right) - ln\left(\frac{J_{l,a} - J}{J - J_{l,c}}\right)\right] \tag{3.2a}$$

$$E_{corr} = E - iR_{cell} - \eta_{conc} \tag{3.2b}$$

To perform the corrections, a glassy carbon electrode in the same position as the semiconductor sample was used as the WE and swept between the mass-transport-limited anodic and cathodic current ranges. Standard data collection consisted of the following potential

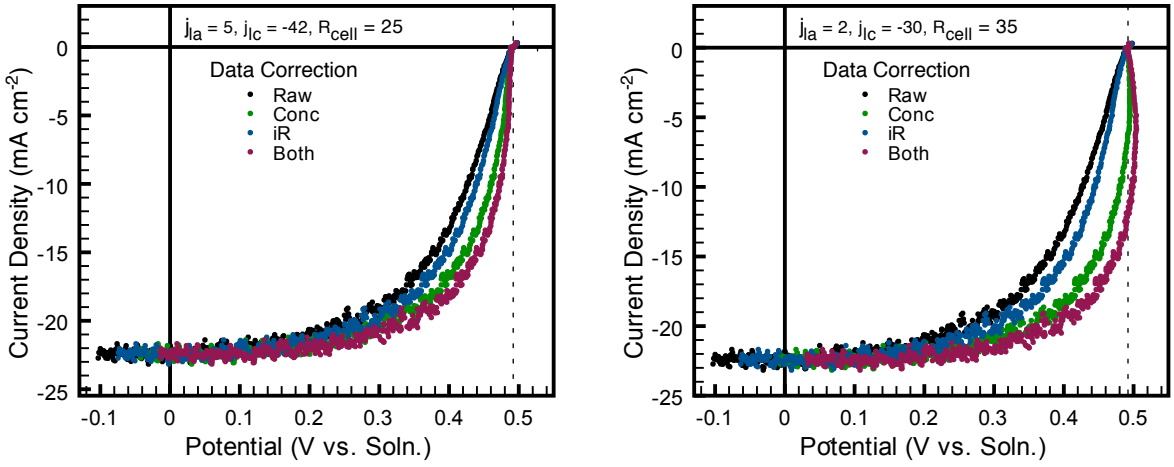

Figure 3.5. Raw and corrected $J-E$ data for a planar p-Si electrode in $MV^{2+/+}$. Left: Properly corrected data; Right: Over-corrected data

sweep: 0.0 V, -0.4 V, +0.2 V vs. E_{sol} (carbon cloth RE). The $J-E$ data was then analyzed to determine the anodic ($J_{l,a}$) and cathodic ($J_{l,c}$) limiting currents. The glassy carbon data was then corrected at each data point for concentration overpotential effects using eqn. 3.2a, and the slope of the corrected curve was used to calculate R_{cell}.

These correction values ($J_{l,a}$, $J_{l,c}$, and R_{cell}) were then used to correct the potential data for semiconductor samples run under the same cell conditions. In order to ensure that this data correction procedure did not over-correct experimental data, a planar control sample was analyzed for the contribution of each component of the data correction (Fig. 3.5). Both graphs show the raw data collected for a planar p-Si electrode, as well as the same data with the iR_{cell} correction, the concentration overpotential correction, and the combined corrections. The corrections applied to the left graph ($J_{l,a}$ = 5 mA cm^{-2}, $J_{l,c}$ = -42 mA cm^{-2}, and R_{cell} = 25 Ω) are based on the experimentally measured limiting currents measured with glassy carbon. These corrections improve the fill factor, but do not change the V_{oc} or J_{sc} and do not introduce any non-physical effects to the data. The data on the right is over-corrected using $J_{l,a}$ = 2 mA cm^{-2}, $J_{l,c}$ = 30 mA cm^{-2}, and R_{cell} = 35 Ω. This is most clearly seen by the fact that the data has been shifted so much that some of the potential data has been shifted to values larger than V_{oc}.

3.2.5 External quantum efficiencies

When using a monochromatic illumination source, it is appropriate to describe the current in terms of the quantum yield (EQY or Φ_{ext}) instead of current density. The external quantum yield is the fraction of photons incident on the semiconductor that produce minority carriers that are collected as current. Since the absorption of photons and thermalization losses in a semiconductor are both wavelength dependent, the current density will vary with wavelength, even if the illumination intensity is kept constant. Φ_{ext} values can be directly compared between different wavelengths of illumination (as is done for spectral response experiments) making it a more useful metric for characterizing semiconductors under monochromatic illumination. The current density measured for a given electrode can be converted to Φ_{ext} using the following equation:

$$\Phi_{ext} = \frac{\left(\frac{i}{qA_{Si}}\right)}{\left(\frac{P}{A_{PD}}\right)\left(\frac{\lambda}{hc}\right)} \tag{3.3}$$

where i is the current in mA, q is the unsigned electronic charge, A_{Si} and A_{PD} are the areas of the Si working electrode and the photodiode detector, respectively, P is the power incident on the photodiode in mW, λ is the wavelength in nm (808 nm in this work), h is Planck's constant, and c is the speed of light. The number of incident photons is calculated from the current density of the calibrated Si photodiode parallel to the working electrode.

3.2.6 Calculating figures of merit

The figures of merit used to characterize the photo-conversion efficiency of semiconductor electrodes were calculated using the equations below. Potentials were referenced to the solution potential, $E(\mathrm{MV}^{2+/+})$, measured by the carbon cloth reference electrode.

The open circuit voltage (V_{oc}) of the devices is the maximum free energy generated by the device relative to the potential of the contacting solution. The value of V_{oc} is calculated as the difference between the potential where the photoelectrode passed no current (E_{oc}) and the reference electrode (E_{sol}) (Eq. 3.4). The short-circuit current density (J_{sc}) is the measured current density of the device at E_{sol} (Eq. 3.5), while the Φ_{ext} is calculated from Eq. 3.3. The fill factor (*ff*) of the device quantifies how the maximum power density (P_{max})

attained by the device compares to the product of the V_{oc} and J_{sc} (Eq. 3.7). The device efficiency was calculated as the ratio of P_{max} to the incoming light intensity, which can be equivalently defined in terms of the *ff*, V_{oc}, and J_{sc} (Eq. 3.8).

$$V_{oc} = E_{oc} - E_{sol} \tag{3.4}$$

$$J_{sc} = \left|J\right|_{E_{sol}} \tag{3.5}$$

$$\Phi_{ext,max} = \Phi_{ext}\big|_{E_{sol}} \tag{3.6}$$

$$ff = \frac{P_{max}}{V_{oc} \cdot J_{sc}} \tag{3.7}$$

$$\eta_{808} = \frac{P_{max}}{P_{in}} = \frac{ff \cdot V_{oc} \cdot J_{sc}}{P_{in}} \tag{3.8}$$

3.3 Photoelectrochemical characterization of VLS Si MW arrays using $MV^{2+/+}$

Photoelectrochemical characterization has provided a useful platform for understanding the material quality and energy conversion properties of VLS-grown Si MW arrays. Using the $MV^{2+/+}$ system, we have investigated the effects of in-situ dopants, wire length and diameter, reactor design, different cleaning and processing steps, and the spectral response of the wire arrays. The sections below focus on three studies that used $MV^{2+/+}$ to characterize VLS-grown Si MW arrays.

3.3.1 Boron-doped Si MW arrays

The $MV^{2+/+}$ redox couple played an important role in verifying the material quality of the first intentionally boron-doped Si MW arrays grown at Caltech. Prior growths of VLS Si wire arrays were unintentionally doped and displayed n-type behavior with widely varying resistivities.[32] Cu-catalyzed VLS-grown p-type Si MW arrays with dopant densities of $\sim$ 1 x 10^{17} cm^{-3} in contact with $MV^{2+/+}$ in an aqueous potassium hydrogen phthalate (KHP) electrolyte produced high photovoltages and fill factors relative to a similarly doped p-type Czochralski-grown (CZ) Si wafer.[41] Figure 3.6 shows data for planar and MW p-Si electrodes measured in aqueous $MV^{2+/+}$ with and without the data corrections. The

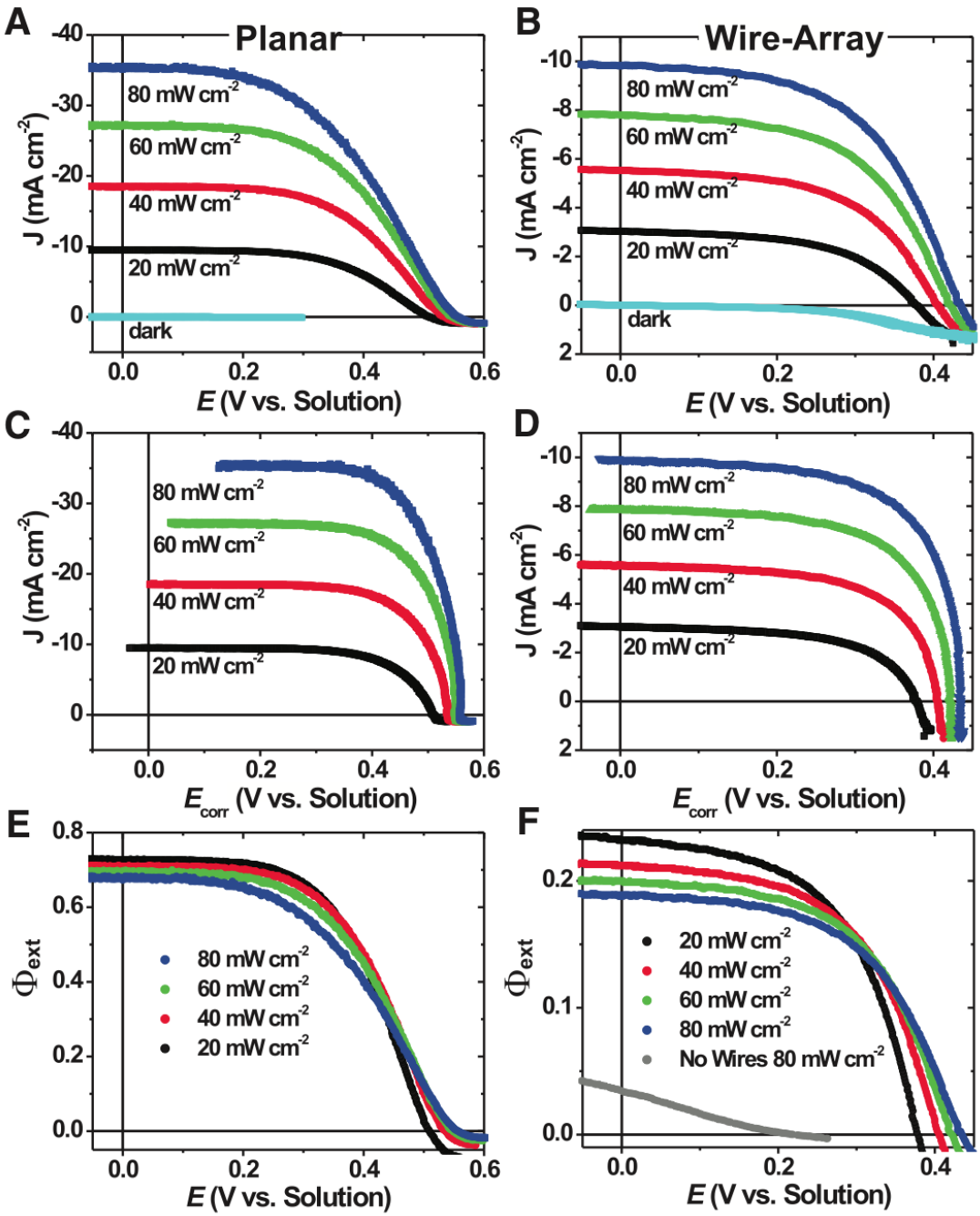

Figure 3.6. $J - E$ data for planar and p-Si MW electrodes. A,B: raw data. C,D: corrected for concentration overpotential and solution resistance losses (equation 3.2). E,F: converted to external quantum yield using equation 3.3 (grey line shows performance of substrates after wires were scraped off). Wire array pattern = 3 x 7 μm square packing.[41]

Table 3.1. Figures of merit for planar and Si MW electrodes in $MV^{2+/+}$ [41]

	V_{oc} (mV)	J_{sc} (mA cm^{-2})	$\Phi_{ext,max}$ –	*ff* (%)	η_{808}
planar p-Si (raw)	555 ± 15	27.9 ± 0.8	0.71 ± 0.02	0.51 ± 0.05	12.9 ± 1.0
planar p-Si (corr.)	–	–	–	0.68 ± 0.05	17.4 ± 1.0
p-SiMW (average)	410 ± 4	7.7 ± 0.9	0.2 ± 0.02	0.5 ± 0.1	2.6 ± 0.4
p-SiMW (best)	420	7.9	0.2	0.55	3.0
p-SiMW (best, corr.)	–	–	–	0.65	3.6

All data reported under 60 mW cm^{-2} 808 nm illumination

50 mM $MV^{2+/+}$ in pH = 2.9 KHP buffer with 0.5 M K_2SO_4 supporting electrolyte

only processing performed on the wire arrays was catalyst removal using aqueous $FeCl_3$ to remove the Cu and KOH etching to remove the outer ∼50 nm of Si. The figures of merit for both types of electrodes under normal incidence are listed in Table 3.1.

3.3.2 Large area VLS growth of Si MW arrays

The $MV^{2+/+}$ system has also been used to verify the material quality of p-Si MWs grown over large areas (150 mm wafers). Figure 3.7A shows the schematic of a cold-wall RF-heated reactor capable of growing wires on a 6" substrate.[35] The growth conditions in this reactor were slightly different than those discussed in Chapter 2 due to the much faster temperature ramping allowed by the RF heating mechanism. A typical growth consisted of a 5 min ramp to 1000°C under H_2, a H_2 anneal for 10 min at 1000°C, and 10–30 min of growth, depending on the desired wire length, with the following gas flow rates: 10 slm H_2, 2 slm H_2 through the $SiCl_4$ bubbler at room temperature, and a variable flow (∼ 100 sccm) of BCl_3 for p-type doping, diluted to 5% in H_2. Typical growth rates were about 3–5 μm/min, depending on the precise growth conditions. After growth samples were cooled to 700°C under H_2 over ∼ 15 minutes so that any Cu in the wires would diffuse to the surface, where it could later be removed by a chemical etch. Figure 3.7B shows an entire 6 inch wafer of VLS-grown Si MWs, and Fig. 3.7C shows an SEM of the wires.

The energy conversion properties of these Si MW arrays are shown in Fig. 3.7D. Even though 4-point measurements on single wires revealed the doping density of these wires was

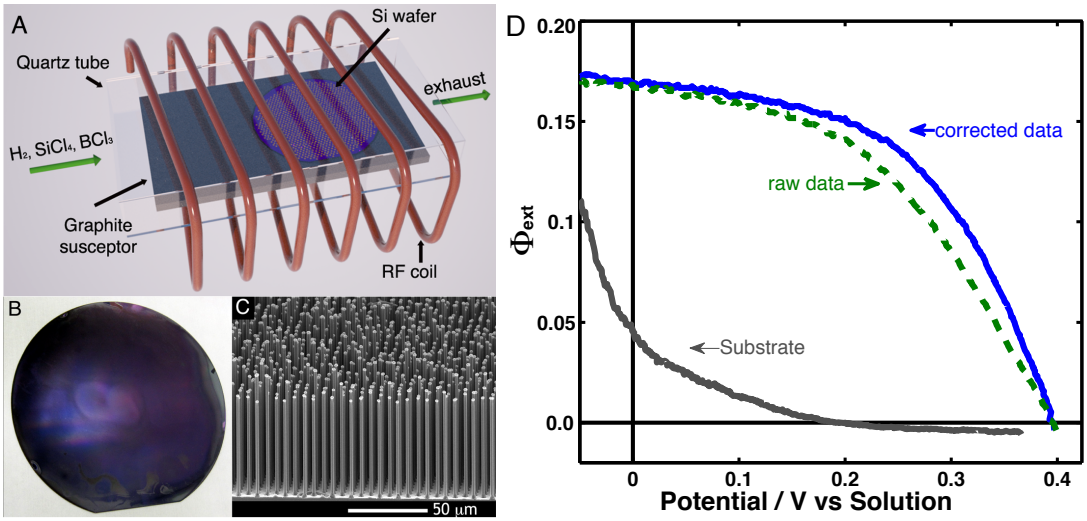

Figure 3.7. A: Schematic of RF-heated, large-area VLS reactor. B: Photograph of a six-inch wafer covered in Si microwires. C: SEM image of these Si MWs. D: External quantum yield vs. solution potential for an electrode grown in the large-area reactor under standard $MV^{2+/+}$ conditions. Data shown before (green) and after (blue) correcting for resistance losses in the solution, and after the wires were scraped off the electrode (gray). The wire arrays were grown from a patterned 3 x 7 μm hexagonally packed pattern and the bases of the wire arrays were embedded in PDMS. Data collected under 60 mW cm^{-2} of 808 nm illumination.

2 x 10^{18} cm^{-3}, the performance is similar to that for wires with lower doping. The addition of the PDMS infill helped to improve the current density in the wires and was needed to prevent shunting between the p-Si wires and the p^+ substrate.

3.3.3 Processing of radial p-n junction Si MW arrays

Semiconductor photoelectrochemistry also allows for high-throughput characterization of the effects of variation of a single parameter of interest such as the length of the wires or the doping density. Such experiments allow for optimization of a material parameter without the need for subsequent processing into an electrochemical device or solid-state photovoltaic cell.[64]

Figure 3.8 shows a comparison of three different p-Si MW arrays that were grown from similar substrates, under the same conditions, but for different periods of time, resulting in different wire heights. The current density increased with the length of the Si MWs: J_{sc} = 4.8 mA cm^{-2} (H = 60 μm), 8.1 mA cm^{-2} (H = 120 μm), 10.0 mA cm^{-2} (H = 150 μm). The measured V_{oc} values are not identical for these samples, but only vary from 405 mV to 440 mV relative to the solution potential, similar to previous reports.[41] The

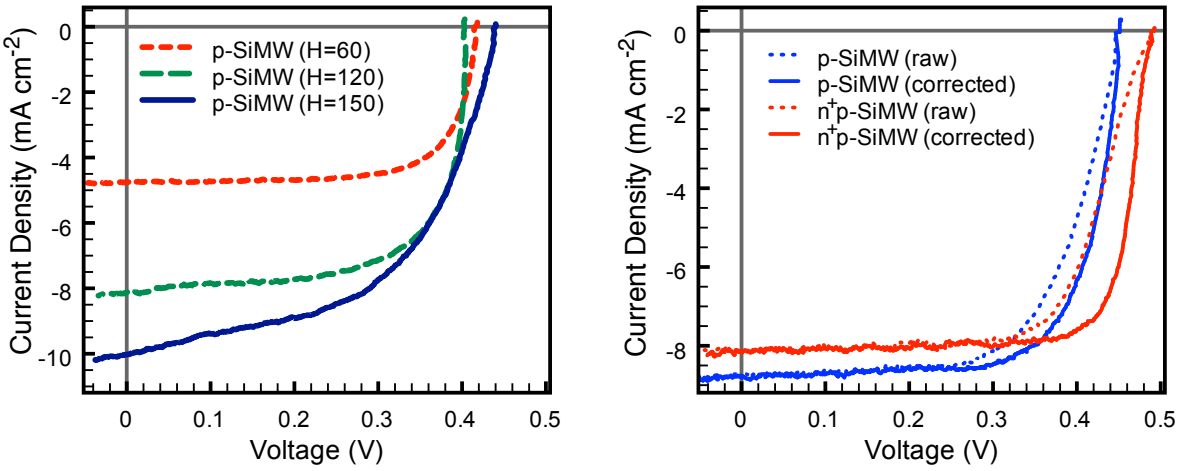

Figure 3.8. Left: $J-E$ data for Si MW arrays (3 x 7 μm square packing) of varying heights: 60, 120, and 150 μm. All wires were grown from the same substrate and had diameters of 1.8–2 μm (3 x 7 μm square packing). Right: $J-E$ data for a wire array before and after the formation of a n^+p radial junction. All of the data were collected under 60 mW cm^{-2} of 808 nm illumination.

right side of Fig. 3.8 shows $J-E$ data for a "booted" p-type wire array before and after the introduction of an n^+-emitter. For this sample, the emitter layer improved the V_{oc} but also increased parasitic absorption so decreased the attainable J_{sc}, showing that the emitter thickness is very important to optimize the overall energy conversion of these highly structured materials.

A liquid contact can also be used to decouple inherent properties of the semiconductor from effects due to formation of the top contact material or other processing steps. Figure 3.9A compares the performance of a Si MW array solar cell characterized using methyl viologen electrochemistry relative to the measured performance of a solid-state device. The blue curve shows the data of the p-Si MW with oxide boots, and the red curve depicts the performance of the polymer-embedded n^+-p junction in contact with $MV^{2+/+}$. The light and dark data for the polymer-embedded solid-state device with a AgNW-based top contact (Fig. 3.9B) are shown by the black solid line and the navy dotted line, respectively.[65] The figures of merit for each of the devices are depicted in Table 3.2.

The introduction of a radial p-n junction (as discussed in Section 2.4.1) increased the photoelectrochemically measured V_{oc} by 70 mV, and also improved the fill factor. The electrical properties of this sample were measured with the wires infilled with polymer, which tended to increase the absorption due to increased scattering, so the decrease in photocur-

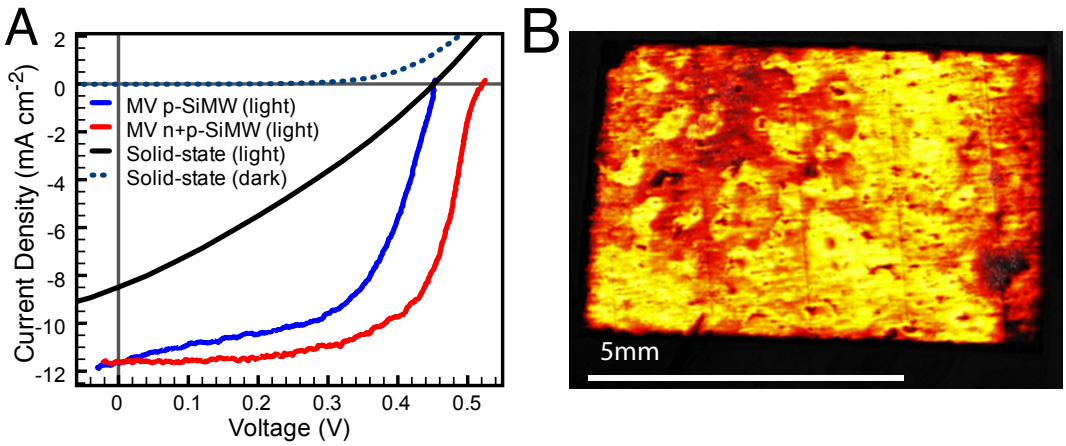

Figure 3.9. A.) $J-V$ data for the same Si MW array at different stages of device processing. The blue and red data show $MV^{2+/+}$ data collected under 60 mW cm^{-2} of 808 nm illumination; the solid-state measurements were performed under 100 mW cm^{-2} of AM 1.5G illumination. B. LBIC map of solid-state device (black data in A) used to calculate the device area. [64]

Table 3.2. Figures of merit at different processing steps in the fabrication of SiMW solar cells

	V_{oc} (mV)	J_{sc} (mA cm^{-2})	*ff* –	$\eta_{808/AM1.5}$ (%)
$MV^{2+/+}$: p-SiMW	453	11.6	0.57	5.0
$MV^{2+/+}$: n^+p-SiMW	521	11.6	0.65	6.3
Solid State: n^+p-SiMW	440	8.49	0.33	1.22

Note: efficiencies for $MV^{2+/+}$ devices are reported for 808 nm illumination while the solid-state devices are based on AM 1.5G illumination.

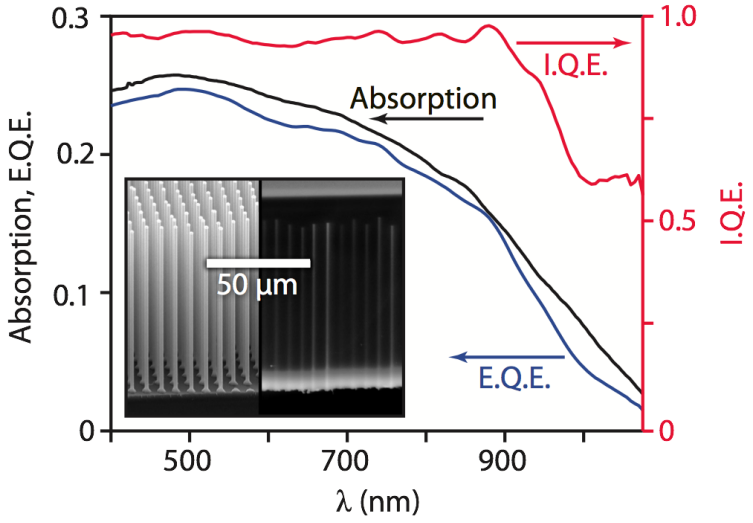

Figure 3.10. Internal quantum efficiency of a VLS grown Si MW array: (blue) the EQY, measured in 10 mM $MV^{2+/+}$ in pH=1 electrolyte; (black) the absorption measured for a peeled wire array; and (red) the IQY calculated as the ratio of the EQY and absorption.[66] (Image credit: M. Kelzenberg)

rent noted in Fig. 3.8 was not as significant here. The light-beam-induced current (LBIC) map in Fig. 3.9B showed that the current density was not uniform across the sample, but LBIC cannot quantify the fundamental cause of the performance loss. The solid-state data shown in Fig. 3.9A, while not indicative of the best cells measured in our labs, exhibited much lower V_{oc} and fill factors then the same device measured photoelectrochemically before addition of the top contact. This behavior demonstrates that the top-contact, and not the material quality of the Si MW array or doping profile, was limiting device performance. The fabrication of good electrical contacts to highly structured photovoltaic materials can be challenging, so it is useful to be able to monitor the semiconductor device quality independent of the choice of contacting material.

3.3.4 Measurement of internal quantum yield

The $MV^{2+/+}$ system was also used to verify the internal quantum yield (IQY) of the Si MW arrays. By comparing the EQY with the measured absorption of wires that have been peeled from the substrate, it is possible to calculate what fraction of the absorbed photons are converted to do useful work. As part of a comprehensive study on the optical properties of VLS Si MW arrays, the EQY was measured in "clear" $MV^{2+/+}$ as a function of wavelength (electrolyte = 0.1 M $MV^{2+}Cl_2$ in 0.5 M KCl(aq) adjusted to pH =1 with

HCl). Data were collected under short-circuit conditions compared to the absorbance of wires grown at the same time and peeled using the procedure in Section 2.3 (Fig. 3.10).

The IQY exceeded 0.9 for most above-bandgap photon energies (λ = 400–900 nm), in good agreement with radial junction theory, which predicts a near-unity IQY for any wire having a radius less than the minority-carrier diffusion length. Although the reported I.Q.E. declined at longer wavelengths, the measured absorption and measured EQY did not vary from each other by more than 5%. This provides strong evidence that the Si MWs do not have defects that cause parasitic absorption.[66]

3.4 Conclusions

Regenerative photoelectrochemical systems are a useful tool for characterizing highly structured semiconducting materials. We have demonstrated the use of this approach for p-type Si MWs grown by the VLS process and the methyl viologen redox couple. The methyl viologen system, in conjunction with other redox systems such as dimethylferrocene/dimethylferrocenium (which makes a high barrier-height contact to n-type Si) has provided a comprehensive understanding of the energy conversion properties of VLS-grown Si MW arrays.[41, 52, 66, 67] In addition, the ability to make a reproducible high-barrier height contact allowed us to quantify the effect of each processing step during the fabrication of flexible Si MW photovoltaic cells, and compare the measured EQY with absorption data. The technique can directly be applied to other photovoltaic materials in various nanowire, nanocone, nano-porous, or other highly structured architectures that are designed to increase the light trapping and carrier collection in next-generation photovoltaic and photoelectrochemical energy conversion devices.

Chapter 4

pH independence of radial n^+p Si microwire array photocathodes

4.1 Introduction

To make an effective photocathode for a solar-driven water-splitting device, it is critical to demonstrate that the photocathode material is stable in an aqueous environment, and can produce some of the photovoltage necessary to drive the desired reaction. P-type silicon is a promising material for the H_2-producing photocathode of a dual photosystem water-splitting device, because p-Si has a bandgap (1.1 eV) that is thermodynamically ideal for an optimized dual bandgap solar water-splitting system [7], the band edges of Si span the H^+/H_2 redox potential, and p-Si is purportedly stable in water under cathodic conditions. However, the literature shows that planar p-type Si electrodes yield significantly smaller photovoltages in contact with the H^+/H_2 redox system than the > 500 mV photovoltages achievable in contact with redox species such as $MV^{2+/+}$.[21, 48] The potential of the H^+/H_2 redox couple, $E(H^+/H_2)$, can be manipulated relative to a fixed reference potential by changing the pH of the solution, but the band-edge positions of Si in H_2O are also sensitive to pH, resulting in a nearly constant photovoltage as the pH of the contacting solution is varied.[68]

If the band-edge positions of the Si could be controlled to eliminate the dependence on pH, the photovoltage of Si/ H^+/H_2(aq) contacts could be increased by simply increasing the pH of the aqueous electrolyte. Functionalization of n-Si surfaces with methyl groups, through two-step chlorination/alkylation chemistry, has been shown to largely eliminate the pH dependence for planar Si electrodes.[59] However, the surface-dipole produced by methyl

termination shifts the Si band edges towards the vacuum level, decreasing the attainable photovoltage for a photocathode.[58, 69] Another approach would involve formation of a p-n homojunction in the Si, to thereby physically separate the rectifying junction from the liquid contact and from any surface-attached catalysts. Consistently, planar p-n Si junctions[70] and micro-particulate crystalline Si homojunction systems[71] have been reported to exhibit increased photovoltages in contact with an electrolyte, relative to the analogous Si/liquid contacts.

To gain insight into this phenomenon, we investigated the pH dependence of the photoelectrode behavior of VLS-grown Si microwire photocathodes (and planar p-Si controls) with and without radial diffused n^+ emitters in aqueous electrolyte. Methyl viologen ($MV^{2+/+}$) is a water-stable, single-electron, outer-sphere redox couple whose reduction potential is independent of pH. The energetics of the direct p-Si / $MV^{2+/+}$ contact should change as a function of pH, due to the well-known dependence of the flat-band potential of Si on the pH of the solution. In contrast, introduction of an n^+-doped emitter layer to create a buried junction, should decouple the band banding, and thus the photovoltage, of the photoelectrode from the energetics of the semiconductor/liquid contact. The ability to decouple the photovoltage of a Si photocathode from the pH of the contacting aqueous solution should increase the versatility of these materials for use in photoelectrochemical fuel-forming systems.

4.2 Experimental setup

The photoelectrochemical setup used in these experiments was the same as that discussed in Chapter 3, using $MV^{2+}Cl_2$ dissolved in an aqueous electrolyte. Three different buffer solutions were prepared by literature methods to compare the performance of the electrodes at different pHs: phthalate (pH 2.9), and phosphate (pH 5.9 and 8.9) with 0.5 M K_2SO_4(aq.) added as a supporting electrolyte before the final pH adjustment with 0.1 M KOH or 0.1 M H_2SO_4.

4.2.1 VLS wire growth and processing

The wires used in this study were grown from $SiCl_4$ with in-situ doping from BCl_3 using Cu as the VLS catalyst. The wires were 50–70 μm in length and 2.0–2.5 μm in diameter.

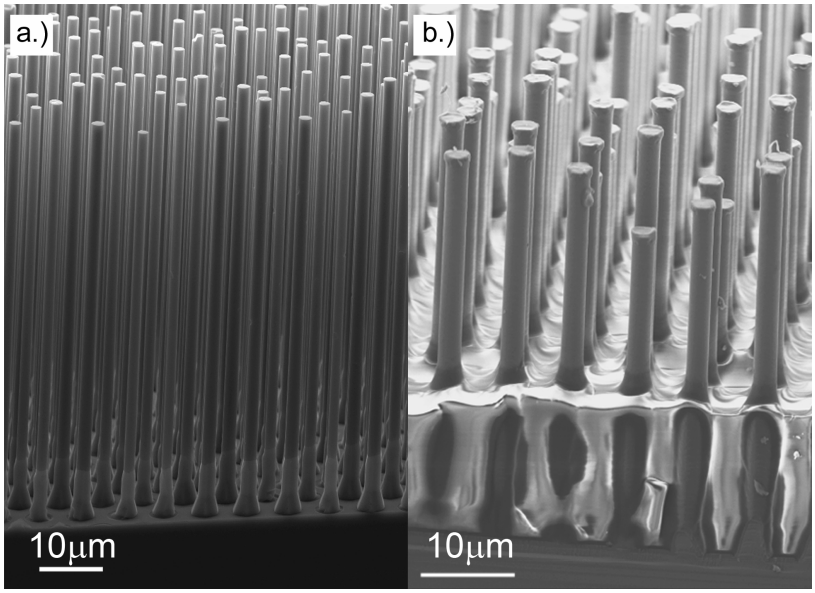

Figure 4.1. SEM images of a.) p-Si microwires with an oxide boot at the base of the wires and b.) of a diffused n^+p Si microwire array infilled with mounting wax (to prevent shunting)

The doping density of the wires was 2 x 10^{17} cm^{-3}, as determined by four-point probe measurements on single microwires.[29, 72] As discussed in Section 3.3.3, an oxide boot was used to define the area of the n^+-emitter region. To create the n^+ emitter layer, the samples were then etched for 30 s in BHF, rinsed in H_2O, and dried with N_2. Samples were loaded onto a quartz boat in-between solid source CeP_5O_{14} diffusion wafers (Saint-Gobain, PH-900 PDS) and heated at 850 °C for 15 min under a N_2 ambient in a tube furnace. Samples were then etched in BHF for 30 s to remove the dopant glass from the surface. To keep the processing as similar as possible between samples, the oxide boot was left on the p-Si MW arrays for photoelectrochemical testing, while the n^+p junction arrays were infilled with mounting wax to prevent shunting. Figure 4.1 shows SEM images of the p-Si and n^+p-Si wire arrays.

4.2.2 Fabrication of planar controls

Prior to diffusion of the n^+ emitter, boron-doped p-Si (ρ = 0.7 Ω-cm) wafers were cleaved into 3 cm x 3 cm chips and cleaned using an RCA etch: (15 min in 6:1:1 by volume H_2O:H_2O_2 (30 % in H_2O):conc. (aq) NH_4OH at 75°C (RCA 1), followed by 15 min in 6:1:1 by volume H_2O:H_2O_2 (30% in H_2O):conc. (aq) HCl at 75 °C (RCA 2). The chips were then rinsed with water and loaded into the diffusion furnace using the same procedure as

for the wire-array samples. A back ohmic contact was made by evaporating ∼100 nm of Al onto the back surface, and then annealing the wafers at 800 °C for 10 min to drive the Al through the thin n^+ layer.[73] Spreading resistance measurements indicated that the surface concentration of phosphorus was $> 1 \times 10^{19}$ cm^{-3} and the n^+ emitter layer was 150–200 nm thick.

4.2.3 Photoelectrochemical measurements

Substrates were cleaved into electrodes with areas of ~ 0.05 cm^2, and connected to tinned Cu wire using Ga/In eutectic and Ag paint. Electrode areas were defined with Loctite 9460 epoxy and allowed to fully cure before photoelectrochemical measurements. All electrochemical measurements were carried out in a cylindrical, flat-bottomed cell equipped with four ground-glass ports. Each experiment used $\sim$ 50 mL of buffer solution and 50 mM $MV^{2+}Cl_2$, and was purged with Ar for 10 min prior to use. Ar continuously blanketed the cell during all experiments. The three-electrode setup consisted of a small carbon cloth reference electrode, a large carbon-cloth counter electrode, and the Si working electrode. The solution potential, $E(A/A^-)$, was kept at between -0.60 and -0.59 V vs. a saturated calomel electrode (SCE) by bulk electrolysis of MV^{2+} to $MV^{+\cdot}$. $E(A/A^-)$ was continuously monitored by measuring the potential at the carbon reference electrode vs. an SCE in contact with the solution. The solution was continuously stirred using a magnetic stirbar placed directly adjacent to the working electrode. Each electrode was tested several times over a period of several days, to ensure that the measured performance was reproducible.

The illumination source was a 1 W, 808 nm diode laser (Thor Labs L808P1WJ). To calibrate the light intensity incident upon the Si sample, a Si photodiode (UDT UV-005) was mounted in solution parallel to each down-facing electrode. The laser beam was expanded to fill the entire area of both the working electrode and calibrated photodiode. Photoelectrochemical data were compared at an incident 808 nm light intensity of 60 mW cm^{-2}, because the maximum short-circuit current density obtainable for Si under such conditions is similar to the maximum short-circuit current density obtainable for Si under 100 mW cm^{-2} of AM 1.5G solar illumination. For all electrodes, the cathodic limiting current density measured in the solution containing 3 mM $MV^{+\cdot}$ was directly compared to that measured in a solution that contained no $MV^{+\cdot}$ to ensure that light intensity was correctly measured.

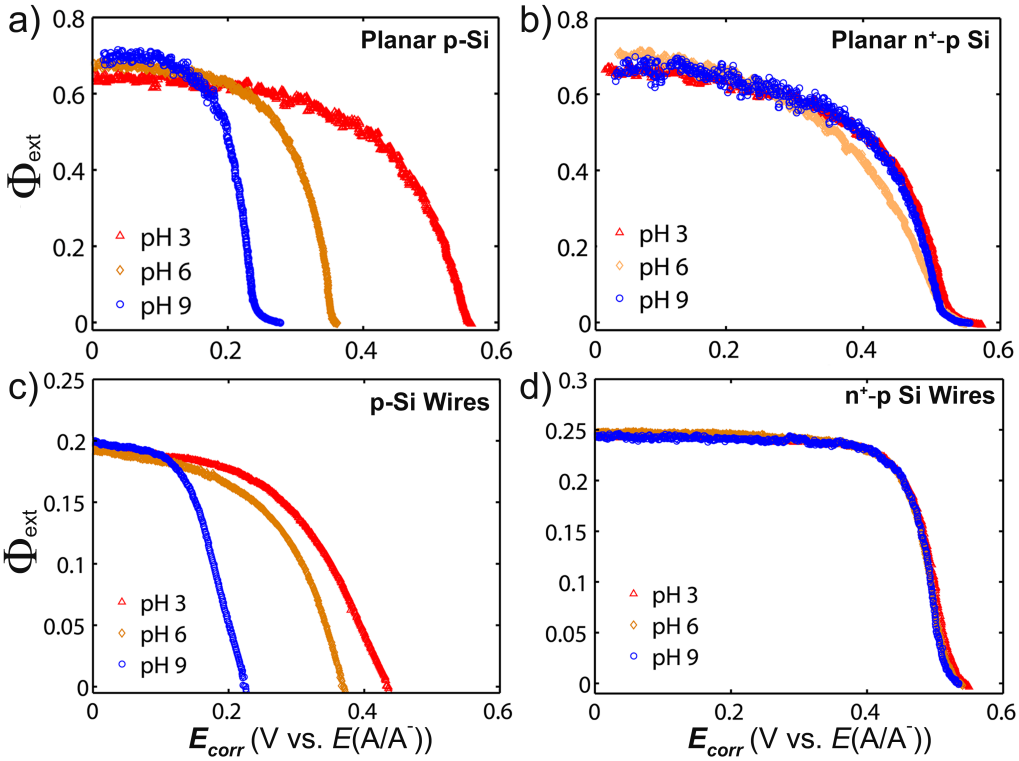

Figure 4.2. Each subfigure (a–d) shows EQY vs. potential data for a single electrode measured at three different pHs. The data is corrected for concentration overpotential and series resistance losses.

4.3 Results

Figure 4.2 shows representative external quantum yield (Φ_{ext}) vs. potential (E) data for (a.) planar p-Si, (b.) n^+p planar Si, (c.) p-Si wire array, and (d.) n^+p wire array structures in contact with 47 mM MV^+ / 3 mM MV^{2+} (aq) under 60 mW cm^{-2} of 808 nm illumination. Each plot shows the Φ_{ext} vs. E data for a representative electrode in buffered solutions at pH 2.9, 5.9, and 8.9, respectively, measured vs. the solution potential, $E(A/A^-)$. Si has a high kinetic overpotential for H_2 evolution, so none of the photocurrent measured is attributable to H_2 production in the potential range of interest.[23] The performance of p-Si wire array electrodes at pH 2.9 was very similar to previously reported data for Si wires that did not contain the oxide boot structure: $V_{oc} = 0.42 \pm 0.01$ V, external quantum yield at short circuit, $\Phi_{ext,sc} = 0.19 \pm 0.01$, fill factor, $ff_{808} = 0.45 \pm 0.02$, and an energy conversion efficiency, $\eta_{808} = 2.3 \pm 0.2\%$. After correcting the data for concentration overpotential and uncompensated resistance losses in the cell (see Section 3.2.4) the corrected photoelectrode fill factor and efficiency were $ff_{808,corr} = 0.48 \pm 0.02$ and $\eta_{808,corr} = 2.5 \pm$

	V_{oc} / mV	J_{sc} / mA cm^{-2}	$\Phi_{ext,\,sc}$	ff_{raw}	ff_{corr}	$\eta_{808,\,raw}$	$\eta_{808,\,corr}$
	n$^+$-p Si Wire Array (best)						
pH 2.9	545	9.69	0.25	0.65	0.72	5.8%	6.4%
pH 5.9	537	9.62	0.25	0.65	0.71	5.6%	6.1%
pH 8.9	535	9.45	0.25	0.65	0.73	5.5%	6.2%
	n$^+$-p Wire Array Electrodes (average)						
pH 2.9	527 ± 25	7.75 ± 2.74	0.20 ± 0.07	0.62 ± 0.05	0.67 ± 0.07	4.3 ± 2.0%	4.7 ± 2.3%
pH 5.9	519 ± 26	7.95 ± 2.37	0.20 ± 0.06	0.64 ± 0.01	0.69 ± 0.03	4.4 ± 1.6%	4.8 ± 1.8%
pH 8.9	518 ± 23	7.78 ± 2.36	0.20 ± 0.06	0.62 ± 0.05	0.68 ± 0.07	4.2 ± 1.8%	4.7 ± 2.1%
	p-Si Wire Array Electrodes						
pH 2.9	418 ± 14	7.31 ± 0.50	0.19 ± 0.01	0.45 ± 0.02	0.48 ± 0.02	2.3 ± 0.2%	2.5 ± 0.2%
pH 5.9	378 ± 15	8.21 ± 1.07	0.21 ± 0.03	0.44 ± 0.02	0.48 ± 0.03	2.2 ± 0.3%	2.5 ± 0.3%
pH 8.9	228 ± 8	8.31 ± 0.73	0.21 ± 0.02	0.40 ± 0.01	0.53 ± 0.03	1.3 ± 0.1%	1.7 ± 0.3%
	n$^+$-p Si Planar Electrodes						
pH 2.9	560 ± 19	24.0 ± 4.5	0.61 ± 0.12	0.45 ± 0.02	0.58 ± 0.04	10.2 ± 2.0%	13.5 ± 2.6%
pH 5.9	550 ± 15	27.4 ± 1.0	0.70 ± 0.02	0.38 ± 0.03	0.52 ± 0.04	9.5 ± 1.0%	13.5 ± 1.4%
pH 8.9	554 ± 13	25.8 ± 0.4	0.66 ± 0.01	0.41 ± 0.00	0.61 ± 0.05	9.8 ± 0.1%	13.8 ± 0.5%
	p-Si Planar Electrodes						
pH 2.9	530 ± 34	22.2 ± 3.2	0.57 ± 0.08	0.55 ± 0.05	0.63 ± 0.06	10.8 ± 2.0%	12.4 ± 2.6%
pH 5.9	371 ± 17	22.7 ± 4.6	0.58 ± 0.12	0.43 ± 0.00	0.58 ± 0.03	6.0 ± 1.0%	8.2 ± 1.8%
pH 8.9	264 ± 8	20.1 ± 3.4	0.41 ± 0.18	0.24 ± 0.05	0.41 ± 0.13	2.1 ± 0.8%	3.8 ± 1.9%

Table 4.1. Photoelectrochemical performance data for each type of electrode measured under 60 mW cm^{-2} of 808 nm illumination in aqueous solution with 50 mM $MV^{2+/+}$

0.2%, respectively. Under the same conditions, the best performing n$^+$p radial junction wire array electrodes yielded $V_{oc} = 0.55$ V, $ff_{corr} = 0.72$, $\Phi_{ext} = 0.25$ and $\eta_{808,corr} = 6.4\%$. The key energy-conversion parameters for all four types of electrodes are reported in Table 4.1.

Figure 4.3 shows the trend in the measured V_{oc} at pH 2.9, 5.9, and 8.9, respectively, under 60 mW cm^{-2} of 808 nm illumination for an average of 3–5 runs for each type of electrode. The diffused n$^+$p junctions displayed nearly identical behavior at all pH values investigated. In contrast, the planar and wire samples that did not contain diffused junctions showed V_{oc} values that strongly depended on pH.[58] The diode quality factor, n, was also calculated for each type of electrode, from the slope of V_{oc} vs. the log of the photocurrent at different illumination intensities:

$$V_{oc} = \frac{nk_BT}{q} ln\left(\frac{J_{ph}}{J_o}\right) \tag{4.1}$$

where k_B is Boltzmanns constant, T is the absolute temperature, q is the (unsigned) charge

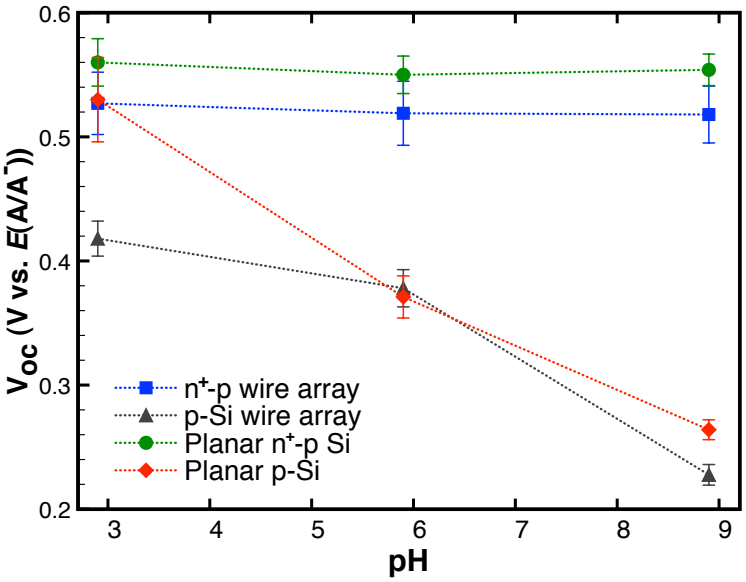

Figure 4.3. The dependence of V_{oc} on solution pH for radial n^+p-Si junction wire arrays, p-Si wire arrays, n^+p planar Si, and planar p-Si electrodes in contact with $MV^{2+/+}$(aq) under 60 mW cm^{-2} 808 nm illumination

of an electron, J_o is the exchange current density, J_{ph} is the photocurrent density, and n is the diode quality factor. Planar p-Si electrodes, and both planar and radial diffused junctions, exhibited n = 1.1–1.2, whereas the diode quality factors for the p-Si wire arrays were 1.5–1.6.

4.4 Discussion

All of the electrodes showed rectifying behavior, consistent with a large barrier height at either the Si/liquid or the n^+p-Si interface. The measured V_{oc} depends primarily on the band-edge positions of the semiconductor, but also on the kinetics of interfacial electron transfer, carrier generation, and carrier recombination.[74, 75] The prominent dependence of V_{oc} on pH, characteristic of p-Si/ $MV^{2+/+}$ contacts, was essentially eliminated by the formation of diffused n^+p junctions, which decouple the carrier-separating junction from the solid/liquid interface, in both planar and wire array photoelectrodes.

The dependence of V_{oc} on pH for the p-Si (planar and wire array) electrodes can be understood from Fig. 4.4. Before contact, the bands in the semiconductor are flat (a), but upon contact with the electrolyte, electrons will flow into the semiconductor to equilibrate the Fermi levels across the junction, causing band bending in the semiconductor (b). The barrier height, Φ_b, i.e., the difference between the valence-band edge of the semiconductor

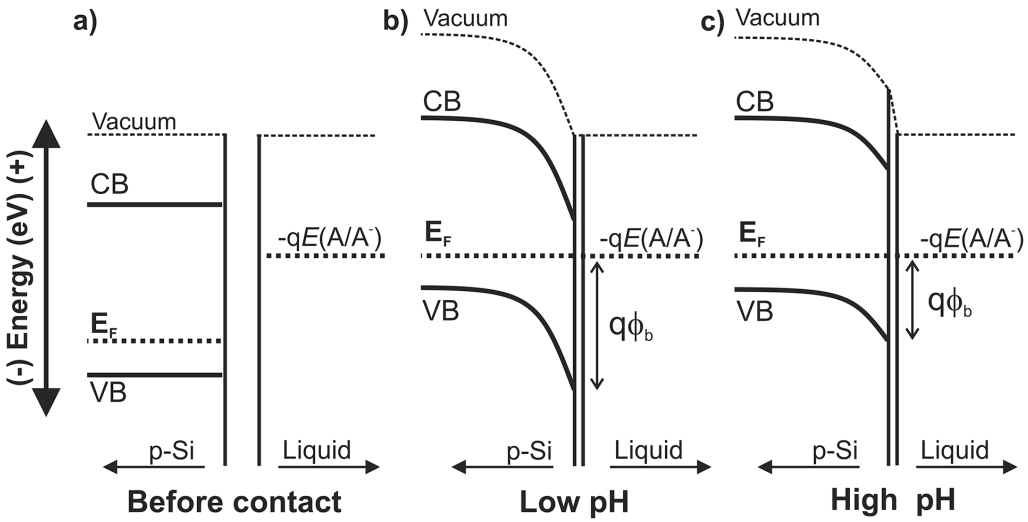

Figure 4.4. Energy vs. position diagrams for a p-type semiconductor in contact with a liquid electrolyte in the dark: a) before contact, b) after contact with a low-pH electrolyte, c) after contact with a high-pH electrolyte. The Fermi level (E_F) of the semiconductor will equilibrate with the solution potential, regardless of where the band positions are located. Because increases in the pH will shift the band edges of Si closer to the vacuum level, for a fixed solution potential, such as that of $MV^{2+/+}$, the barrier height, Φ_b, will decrease, which decreases the open-circuit voltage under illumination.

and $qE(A/A^-)$, sets an upper limit on the maximum attainable V_{oc}. The flat band potentials of Si in contact with aqueous electrolytes have been previously reported to vary by 30 mV / pH unit, as revealed by differential capacitance measurements of the semiconductor electrode as a function of pH.[68] This pH dependence is plausibly the result of the acid/base equilibria of surface H and OH groups changing the voltage drop across the double layer at the semiconductor/liquid junction. At higher pH (Fig. 4.4c), the shift of the Si band edges towards the vacuum level decreases the barrier height in the system, which should correspond to a decrease in the measured V_{oc}, because $E(MV^{2+/+})$ is independent of pH. The results for both planar p-Si and the p-Si wires support this hypothesis, showing decreased V_{oc} at higher pH. For the planar p-Si samples, V_{oc} shifted by (44 ± 4) mV / pH unit, which corresponds well to recent photoelectrochemical measurements of H-terminated p-Si in contact with $MV^{2+/+}$.[58] The open-circuit voltages of p-Si wire array electrodes showed non-linear behavior with respect to pH, which, along with their higher diode quality factors, suggests the presence of trap states or defects at the wire surface.

The Φ_{ext} vs. E data for both the radial and planar n^+p-Si/ $MV^{2+/+}$ junctions were nearly identical at all pH values. Electrodes were tested at different pHs over a period

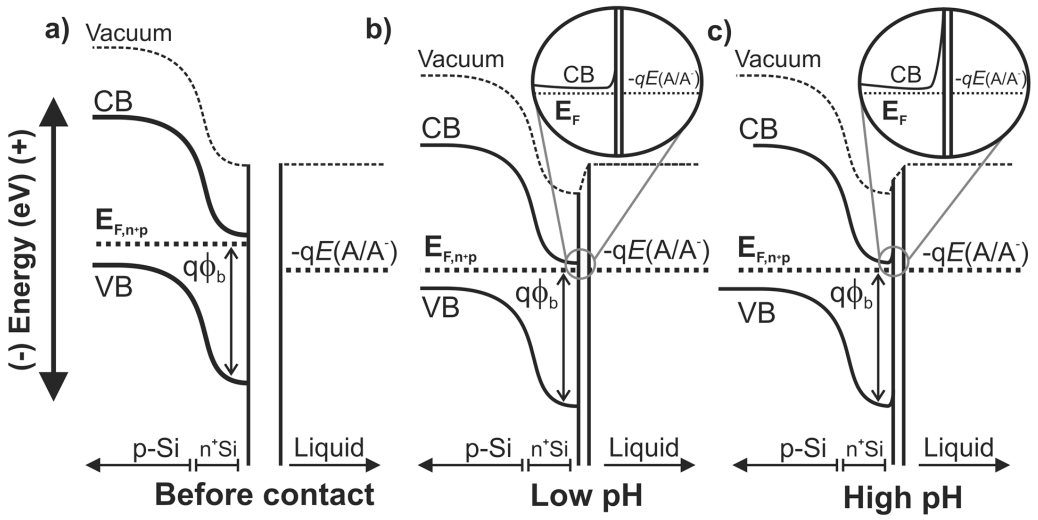

Figure 4.5. Energy vs. position diagram for a n^+p-Si junction in contact with a liquid electrolyte in equilibrium in the dark: a) before contact, b) in contact with a low-pH electrolyte, and c) in contact with a high-pH electrolyte. The inset indicates that the surface energetics of the n^+-Si have shifted as in Fig. 4.4c, except that the high doping of the semiconductor creates a very narrow depletion region, so charged carriers can easily tunnel across the junction. For a n^+p buried junction, Φ_b and the open-circuit voltage under illumination are decoupled from the pH of the liquid electrolyte.

of several days, with negligible variation in observed performance. Because the n^+ emitter layer was deliberately not passivated, the band-edge positions of the semiconductor should thus move with pH (Fig. 4.5). However, the high doping of the emitter gives this contact metallic character, so the band bending occurs across a narrow region of the semiconductor (Fig. 4.5c inset). Based on the surface phosphorus dopant density measured by the spreading resistance ($N_D \sim 10^{19}$ cm^{-3}), the depletion width at the liquid interface should be $\sim$ 10 nm, which is thin enough that photogenerated carriers can efficiently tunnel across the junction.[76] Hence, the n^+p junction is effectively a floating diode, similar to the GaAs/$GaInP_2$ photocathode device reported by Khaselev and Turner.[77] The invariance in the $J-E$ data relative to a fixed reference potential, across six pH units, provides strong evidence that high photovoltages will be achievable when these wire arrays are decorated with electrocatalysts and used, for example, as photocathodes for solar water-splitting or CO_2 reduction. The Φ_{ext} values of the wire arrays of this particular filling fraction are limited by optical absorption at normal incidence, which can be improved by the introduction of scatterers as well as by other methods.[46, 66]

Increasing the attainable photovoltage, and removing the band-edge dependence from Si

microwire photocathodes as described herein, could greatly increase conversion efficiency of a hydrogen generating system, which requires a total photovoltage of 1.23 V. Most reports in the literature on p-Si photocathodes for solar water-splitting use noble metal catalysts (Pt, Pd) in acidic electrolytes, but most earth-abundant HER catalysts are not stable at low pH. Hence the ability to operate Si microwire arrays under neutral or alkaline conditions increases the versatility of possible design strategies for use of Si as a water-splitting photocathode. The same principles should apply to buried-junctions in other semiconductors, allowing the creation of devices that decouple the semiconductor energetics from the solution/catalyst interface.

4.5 Conclusion

The effects of introducing an n^+-doped emitter layer was evaluated for both planar Si photoelectrodes and for radial junction Si MW array photoelectrodes. In contact with the pH-independent $MV^{2+/+}$ system, both planar and wire array p-Si photoelectrodes yielded open-circuit voltages that varied with the pH of the solution. The highest V_{oc} values were obtained at pH = 2.9, with V_{oc} = 0.53 V for planar p-Si electrodes and V_{oc} = 0.42 V for VLS p-Si microwire array samples, under 60 mW cm^{-2} of 808 nm illumination. Increases in the pH of the electrolyte produced a decrease in V_{oc} by approximately -44 mV/pH unit for planar electrodes, with similar trends observed for the Si microwire array electrodes. In contrast, introduction of a highly doped, n^+ emitter layer produced V_{oc} = 0.56 V for planar Si electrodes and V_{oc} = 0.52 V for Si microwire array electrodes, with the photoelectrode properties in each system being essentially independent of pH over six pH units ($3 < pH < 9$).

The invariance of the photoelectrode performance with respect to pH demonstrates that such an approach can decouple the band-edge energetics of the semiconductor from the pH of the solution. High photovoltages can thus be obtained from buried junctions in redox systems that, due to non-optimal band-edge positions, inherently yield low photovoltages at Si/liquid contacts, such as p-Si/H^+-H_2(aq) contacts, which are limited to photovoltages of 300 mV regardless of the pH of the electrolyte. The observations thus suggest a route to the development of efficient buried junction Si microwire photocathodes that can operate efficiently under a wide variety of conditions for fuel-forming reactions, such as photoelectrochemical hydrogen evolution or CO_2 reduction.

Chapter 5

Silicon photocathodes for hydrogen evolution

5.1 Introduction

Silicon is a promising material to serve as a photocathode for solar hydrogen production. It is earth abundant, widely used and well-characterized in photovoltaic systems, and also has the appropriate band energetics to drive the reductions of protons to form H_2 as part of an overall water-splitting device. The Si surface, however, has poor kinetics for the hydrogen evolution reaction (HER), and requires a catalyst to achieve efficient solar energy conversion.[21] There are several accounts in the literature of Si-based photocathodes, but most devices have relied on noble metal catalysts such as Pt or Pd, that are too rare and expensive to be viable options for a low-cost water-splitting device.[78]

The structuring of light absorbers, such as Si, into microwire and/or nanowire-based morphologies orthogonalizes the directions of light absorption and carrier collection, and thus provides an opportunity to obtain high solar energy-conversion efficiencies with low purity semiconductor materials.[28] Accordingly, we have demonstrated high conversion efficiencies in regenerative electrochemical cells and solid-state devices for p-Si and n^+p SiMW arrays.[30, 41, 46] For photoelectrochemical applications, the high surface area of MW array structures facilitates a high catalyst loading onto a given projected area of the electrode. On a projected-area basis, this increased loading allows, in principle, non-precious metal electrocatalysts to yield comparable performance to noble-metal catalysts, such as Pt, for multi-electron-transfer processes such as H_2 production from H_2O.[79, 80]

This chapter will discuss the development of Si-based photocathodes as hydrogen evolution photocathodes. Both p-Si and n^+p-Si systems were investigated to understand the performance limitations of each system when coupled to different HER catalysts. Section

5.2 will focus on the experimental setup and efficiency calculations for the three-electrode characterization of photocathodes for solar fuels. We will then focus on the different catalyst systems investigated, and compare their performance on planar and structured Si electrodes. The effect of introducing a radial p-n junction will be discussed as a proof of concept for improving HER photocathode performance.

5.2 Electrochemical characterization

Many semiconductor materials, including Si, have attractive features for driving photochemical reactions, but do not have bandgaps large enough to drive the unassisted water-splitting reaction. As discussed in Chapter 1, it is still possible to characterize semiconductor materials as photoelectrodes using a potentiostat to drive the other half of the desired reaction at a counter electrode while measuring the potential of the material of interest relative to a known reference.

5.2.1 Photoelectrochemical cell setup

All experiments were carried out in a glass electrochemical cell with a flat, side facing window, three electrode ports, and one gas inlet port. An SCE electrode was used as the RE and either Pt or carbon cloth mesh was used as the CE, but separated from the cell using a porous glass frit. Electrodes were prepared in the same way as for regenerative electrochemical testing (Section 3.2.2), except all electrodes for H_2 evolution were made side-facing to ensure that bubbles were not trapped on the electrode surface.

In order to ensure reproducible results, particularly when investigating non-Pt catalysts, all components of the cell were thoroughly cleaned before use. Glassware and PTFE-coated stir bars were soaked in aqua regia (3:1 HCl:HNO_3) for 2–24 hrs and then rinsed copiously with 18 MΩ-cm water. To maintain a well-defined Nernstian $E(H^+/H_2)$ redox potential, the cell was purged with H_2 continuously during experimentation. When driving reductions reactions such as the HER, it is possible that trace ions in solution will also be deposited on the working electrode, which can either lead to fouling or may enhance the apparent catalytic activity of the working electrode. Electrolytes were prepared from the highest purity materials possible, and made in batches larger than what is required for a single run to ensure consistency between different days of experimentation. To verify

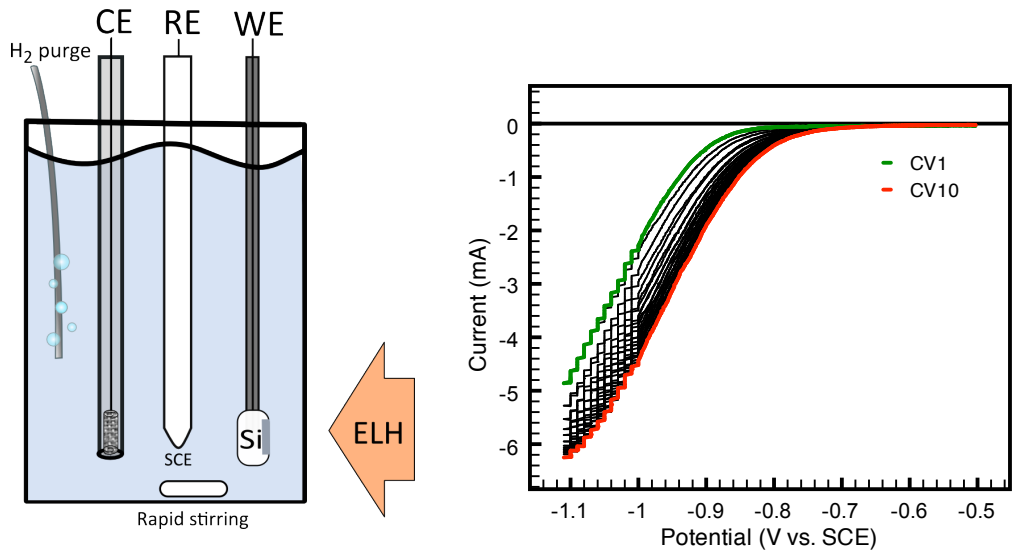

Figure 5.1. Left: Schematic of cell for HER photoelectrochemistry. Right: $I - E$ data for a bare p-Si electrode in clean aqueous electrolyte (pH = 4 KHP, 0.5 M K_2SO_4. $E(H^+/H_2)$ = -0.51 V vs. SCE). Data collected at 100 mV s^{-1}

that the system was not contaminated with trace metals, a clean p-Si electrode was usually cycled 10–100 times over the potential range to be used in experiments. If the onset of H_2 evolution improved significantly during this test, the electrolyte was replaced and/or the cell components were re-cleaned. An example of a standard cleaning sweep is shown in Fig. 5.1. After data collection, the RHE potential can be determined by taking linear sweep voltammetry (LSV) data with a polished Pt-button electrode.

5.2.2 HER photocathode efficiency calculations

The performance of each electrode was evaluated using standard performance metrics for photovoltaic devices, with potentials calculated relative to the reversible hydrogen electrode (E_{RHE}). Referencing data to RHE accounts for the fact that the thermodynamic potential for the H_2/H^+ redox couple is pH dependent, and allows data taken under different pH conditions to be compared directly.

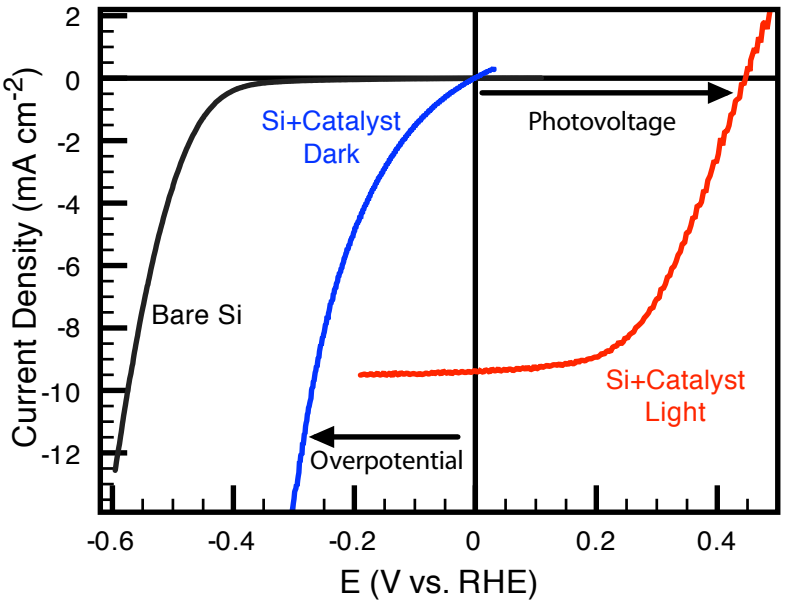

Figure 5.2. $J-E$ data for a bare p-Si electrode under illumination (black), a catalyst-coated p-Si electrode in the dark (blue), and a catalyst-coated Si electrode under illumination (red)

$$V_{oc} = E_{oc} - E_{RHE} \tag{5.1}$$

$$J_{sc} = \left|J\right|_{E_{RHE}} \tag{5.2}$$

$$ff = \frac{P_{max}}{V_{oc} \cdot J_{sc}} \tag{5.3}$$

$$\eta_{H_2} = \frac{P_{max}}{P_{in}} = \frac{ff \cdot \ V_{oc} \cdot J_{sc}}{P_{in}} = \frac{-i_{max}(E_{max} - E_{RHE})}{P_{in} \cdot A} \tag{5.4}$$

The open circuit voltage (V_{oc}) of the devices is the maximum free energy generated by the device relative to the thermodynamic HER potential under the specified experimental conditions. The value of V_{oc} is calculated as the difference between the potential where the photoelectrode passed no current (E_{oc}) and the real hydrogen electrode potential (E_{RHE}) measured during the experiments (Eq. 5.1). The short-circuit current density (J_{sc}) is the measured current density of the device at E_{RHE} (Eq. 5.2). The fill factor (*ff*) of the device quantifies how the maximum power density (P_{max}) attained by the device at potentials positive of E_{RHE} compares to the product of the V_{oc} and J_{sc} (Eq. 5.3). The photocathode efficiency was calculated as the ratio of P_{max} to the incoming light intensity, which can be equivalently defined in terms of the *ff*, V_{oc}, and J_{sc} or in terms of the current and voltage

measured at the maximum power point (i_{max} and E_{max}) (Eq. 5.4). The errors reported in all measured values represents 1σ confidence intervals.

Efficiencies that are calculated in this fashion do not include resistance losses that would be present in a two-electrode cell, nor do these efficiencies account for polarization losses at the counter electrode. The values are thus reported as single photoelectrode efficiencies for the working electrode, as opposed to efficiencies for the overall water-splitting reaction. In this work, the calculated photoelectrode efficiencies are referenced directly to the behavior of an ideally nonpolarizable working electrode, and thus all photoelectrode potentials are referenced to the thermodynamically reversible potential, E_{RHE}. The use of a thermodynamically measured reference allows facile and consistent comparison between the behavior of semiconductor–catalyst composites with varying compositions and in various electrolytes, provided that E_{RHE} is well defined for the electrolyte system of interest. Coupling the single-electrode measurements used herein with analogous measurements for photoanodes also allows prediction of the operating current density, and overall efficiency, of a tandem water-splitting cell.[8]

The maximum power point for fuel-forming photocathodes has alternatively been calculated by comparing the behavior of the photo-responsive working electrode to the $J - E$ behavior of a clean Pt working electrode measured under nominally the same conditions as the photoelectrode.[18, 81] These "power saved" efficiencies are therefore subject to the properties of the working electrode and electrochemical cell that has been selected to be the "reference system." Efficiency values that are calculated in this alternative fashion are higher than the ones quoted herein because the "power saved" efficiencies account for kinetic and concentration overpotential losses at the selected Pt working electrode as well as for uncompensated resistance losses in the electrolyte.

5.3 Hydrogen evolution catalysts

The behavior of a catalytic material is often discussed in terms of the overpotential needed to drive a chemical reaction at a given current density. Accounting for the fact that the theoretical operating current density for an ideal solar-water-splitting device is 10–30 mA cm^{-2} and that there will also be overpotential losses from the OER reaction and the electrolyte, a design goal for the HER catalyst is to be able to operate at J_{op} with < 100 mV overpotential.[82]

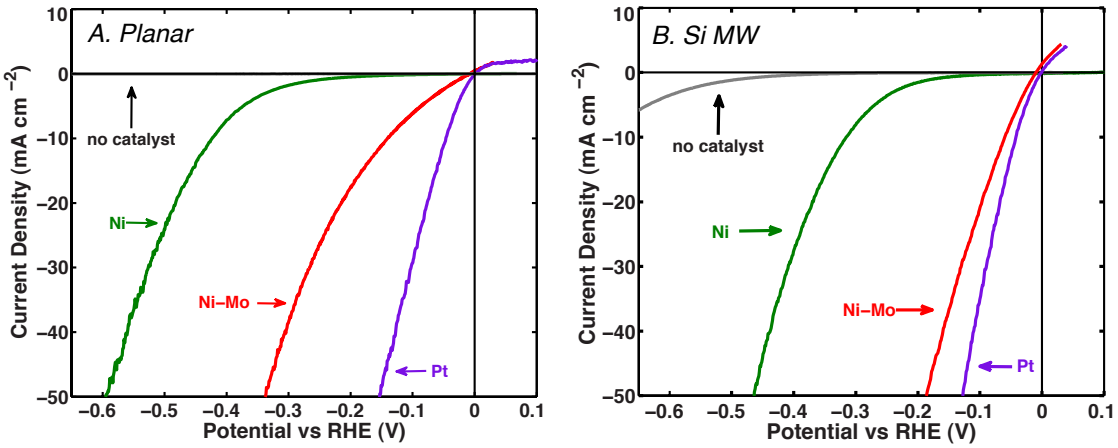

Figure 5.3. A. Catalytic HER onset data for Pt, Ni, and Ni–Mo on degenerate planar Si substrates. B. Catalytic HER onset data for Pt, Ni, and Ni–Mo on degenerate Si MW substrates. Data collected in H_2-purged pH 4.5 KHP buffer.[79]

While many materials have been investigated as catalysts for the HER, the current work focuses on mixed-metal catalysts based on Ni, which have been shown to have high performance comparable to noble metal catalysts. Alloys of Ni and Mo (Ni–Mo) have been reported to achieve current densities of 1 A cm^{-2} for the HER under alkaline conditions at overpotentials of < 100 mA.[26] In our group, methods were developed to electrodeposit Ni–Mo at milder pH conditions that are more compatible with Si photoelectrochemistry.[79] Stability testing of this electrodeposited material revealed that it was catalytically active, and stable over extended periods of time in pH 4.5 KHP buffer.

To investigate whether the use of the highly structured Si MW arrays could further improve the performance, the performance of Ni, Pt and Ni–Mo alloy catalysts were compared on planar and Si MW substrates. Figure 5.3A shows the HER polarization behavior of planar, degenerately doped Si electrodes with no catalyst, Ni, Ni–Mo, or Pt. While not as good of a catalyst as Pt, the Ni–Mo alloy catalyst significantly out-performs Ni alone. Figure 5.3B shows the HER polarization performance of the same catalysts, but this time on degenerately doped Si MW arrays. The increased surface area of the Si MW arrays allows higher catalyst loading, so that Ni–Mo and Ni improve significantly. The performance of Pt does not improve, because as a very fast catalyst, its loading is likely not the limiting factor under these conditions.

5.4 p-Si HER photocathodes

Based on promising performance of the p-Si MW in regenerative electrochemical cells discussed in Chapters 3 and 4, and the dark catalytic performance discussed above, p-Si planar and MW array electrodes with various HER catalysts were investigated as photoelectrodes for hydrogen evolution.

Due to the differences in light absorption and diffusion within an array of Si wires relative to the planar samples, new deposition conditions were needed to control the particle size and uniformity for the high aspect-ratio wires. Uniform distributions of Pt, Ni, and Ni–Mo metal nanoparticle films were produced by electrodeposition and by using galvanic displacement deposition, in which metal ions from solution are reduced as the Si is slowly etched by hydrofluoric acid (HF) without any external bias.[83]

5.4.1 Catalyst deposition

By modifying the deposition procedures from the literature, we were able to achieve uniform distribution of nanoparticles of several metals that have high HER exchange current densities on the high aspect ratio Si microwires.

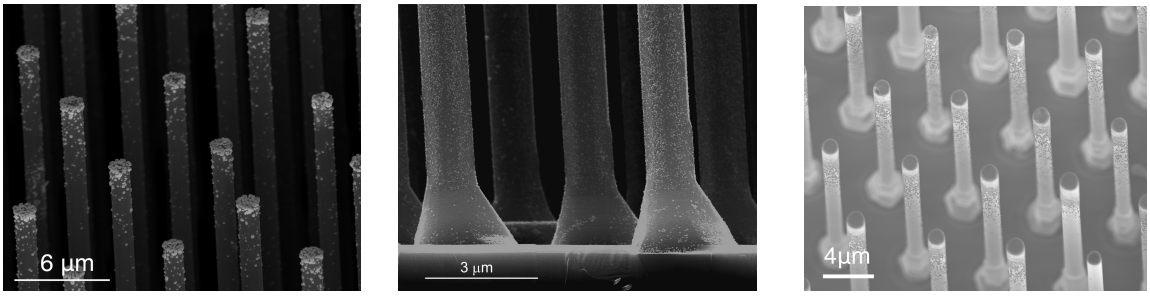

Figure 5.4. SEM images of (L to R): Pt, Ni, and Ni–Mo nanoparticles deposited on p-Si MW arrays

Pt deposition. Pt nanoparticles were deposited from an aqueous solution of hydrofluoric acid and chloroplatinic acid (H_2PtCl_6) or K_2PtCl_6.[78] The HF concentration in the plating bath was varied between 0.25 M and 1.0 M, while the concentration of Pt salt was varied between 0.25 and 1 mM. Decreasing the concentration of HF increased the uniformity of deposition along the length of the wires, while decreasing the Pt salt concentration resulted in more uniform particle sizes. Pt has been shown to follow a progressive nucleation

mechanism, so at higher concentrations, new particles are continuously forming on the surface.[84] Further experiments used 0.5 M HF and 1.0 mM K_2PtCl_6. Deposition was carried out by immersing the electrode in the plating solution for 2 minute increments, and then testing the electrochemical performance of each electrode. The optimal deposition time (maximized catalytic activity without adding too much catalyst to block the light) was between 4 and 6 min. Pt was also evaporated onto p-Si samples using an e-beam evaporator, but no photovoltage was observed for any of the samples with evaporated Pt.

Ni deposition. Ni was deposited onto electrodes using either electrodeposition or electroless displacement. Nanoparticles were electrolessly deposited from an aqueous solution of ammonium fluoride (NH_4F) and nickel sulfate ($NiSO_4$). Due to the instantaneous nucleation method for Ni, the particle sizes were much smaller than observed for Pt (center image Fig. 5.4).[85] Deposition was carried out by immersing the Si sample in the electroless deposition bath for 4 min and then testing the electrochemical performance. Ni electrodeposition was carried out by depositing Ni from a bath that contained 1.3 M Ni^{II} sulfamate and 0.5 M H_3BO_3. Depositions were carried out galvanostatically under illumination (20 mA cm^{-2} for 0.5 to 5 s).[79]

Ni–Mo electrodeposition. Ni–Mo was electrodeposited from a bath that contained 1.3 M Ni^{II} sulfamate, 0.5 M H_3BO_3, and 20 mM Na_2MoO_4, with the pH adjusted to be $\sim$ 4.5 using KOH.[79] Electrodeposition was performed using a PAR 273 potentiostat, in a one-compartment cell, using a large area Ni foil counter-electrode and an Ag/AgCl reference electrode. Samples were immersed in the deposition solution and illuminated at high intensity ($\sim$ 400 mW cm^{-2}) with an ELH-type tungsten-halogen lamp. Ni–Mo was deposited under galvanostatic conditions: 20 mA cm^{-2} for 20–30 s (right image Fig 5.4).[79]

5.4.2 Planar Si with HER catalysts

Initial photoelectrochemical experiments were performed using planar p-Si electrodes coated with electrolessly deposited Pt nanoparticles in contact with acidic (pH = 2) electrolyte (Fig. 5.5). Performance was optimized at this pH between the catalytic activity of Pt (better in acid) and the measured V_{oc}, which decreased in more acidic electrolyte.[86] The electrodes showed an onset in photocurrent positive of RHE, which varied with illumination intensity,

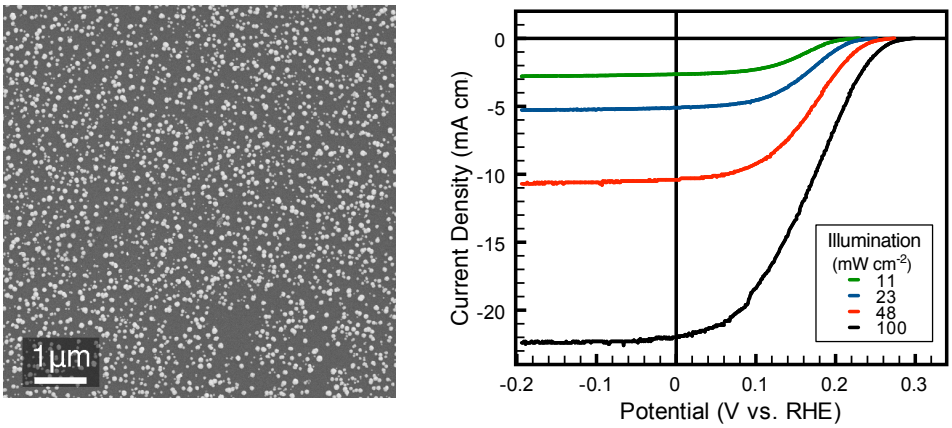

Figure 5.5. Left: SEM image of electrolessly deposited Pt on planar p-Si. Right: $J-E$ data for planar p-Si electrodes with electroless Pt as the HER catalyst in a pH = 2 aqueous solution (0.5 M K_2SO_4 adjusted with H_2SO_4). Scan rate = 20 mV s^{-1}. The cell was purged with H_2 and the data are referenced to RHE = -0.362 V vs. SCE. Illumination = ELH-type solar simulation (intensity adjusted using neutral density filters).

but produced less than 300 mV V_{oc} under 1 Sun illumination, similar to reports in the literature. All of the figures of merit for these devices are listed in Table 5.1.

To compare the performance of different catalysts on planar p-Si, electrodes were tested in pH = 4.5 KHP with 0.5 M K_2SO_4 supporting electrolyte to ensure stability of all catalysts. The left of Fig. 5.6 compares all three catalysts under 1 Sun ELH illumination.

5.4.3 p-Si MW with HER catalysts

Similarly, p-Si MW electrodes were compared with each of the catalysts under 1 Sun illumination in pH = 4.5 KHP with 0.5 M K_2SO_4 supporting electrolyte. Electrodes were fabricated from p-type Si MW arrays after catalyst removal, and then coated with catalyst immediately before electrochemical testing. The electrodes were tilted slightly to maximize the measured J_{sc}. Figure 5.6 shows $J-E$ data for similar wire arrays coated with different catalysts. While all of the catalysts increased the onset of the HER by over 500 mV relative to bare p-Si MW arrays, the photovoltage generated positive of $E(H^+/H_2)$, never exceeded 300 mV under 1 Sun illumination. The V_{oc} for Ni–Mo electrodes was similar to that of Ni, but less than that of Pt, even though the catalytic onset and *ff*s were better than pure Ni. Due to the small photovoltages generated, the overall energy conversion efficiencies for catalyst-decorated p-Si MW electrodes never exceeded 1%.

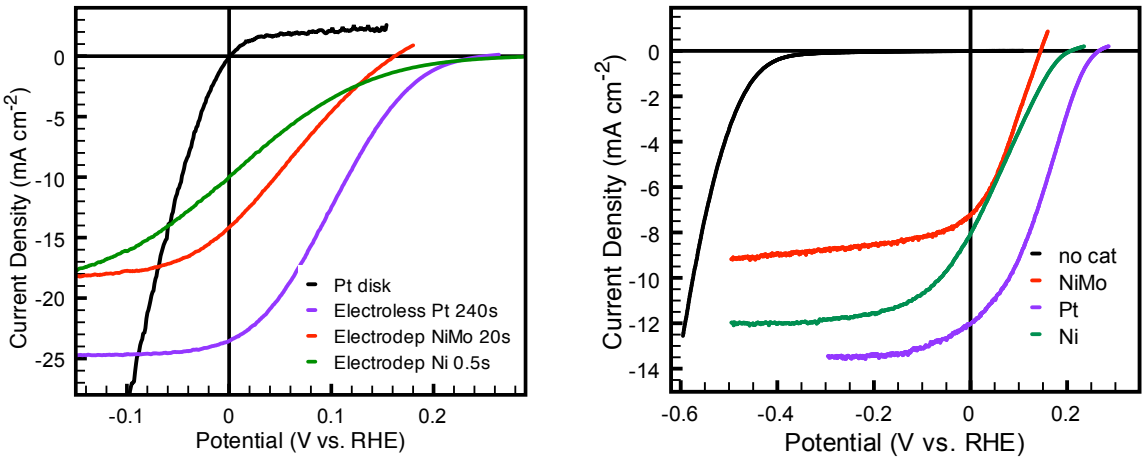

Figure 5.6. Left: $J - E$ data for planar p-Si electrodes with Pt, Ni, or Ni–Mo as the HER catalyst. Right: $J - E$ data for Ni, Ni–Mo, and Pt on p-Si MW electrodes. All data collected in a H_2-purged pH = 4.5 KHP buffer and are referenced to the reversible hydrogen potential in the solution ($E(H^+/H_2)$ = -0.51 V vs. SCE).[79]

5.5 n^+p Si MW photocathodes with Pt

To demonstrate that high photovoltage could be achieved independently of catalyst effects, the HER chacteristics of radial n^+p junction SiMW arrays coated with Pt catalysts were investigated. As demonstrated in Chapter 4 the introduction of a heavily doped emitter layer decouples the photovoltage generated by the semiconductor from the contacting metal or solution. The general scheme for fabricating a p-n junction is the same discussed in Chapter 2, with the additional requirement that the interface between the p-Si base and the n^+ emitter be protected to avoid shunting in the device.

As a proof of concept, such n^+p radial junction Si MW array electrodes were fabricated, and then Pt was evaporated onto the wires to serve as the HER catalyst. The base of the wire array was infilled with mounting wax, which was removed from the tips of the wires by plasma ashing. Control devices that used Pt as a HER catalyst were produced by using e-beam evaporation to deposit 1.5 – 2 nm planar equivalents of high-purity Pt (Kurt Lesker, 4N) at a rate of 0.01–0.05 nm s^{-1} onto the Si wire arrays. Immediately before deposition, the Si MW array samples were briefly etched in buffered HF, to remove native oxides. Figure 5.7 compares the performance of planar (red) and Si MW (blue) n^+p junction HER photoelectrodes. The figures of merit for both p-Si and n^+p junction planar

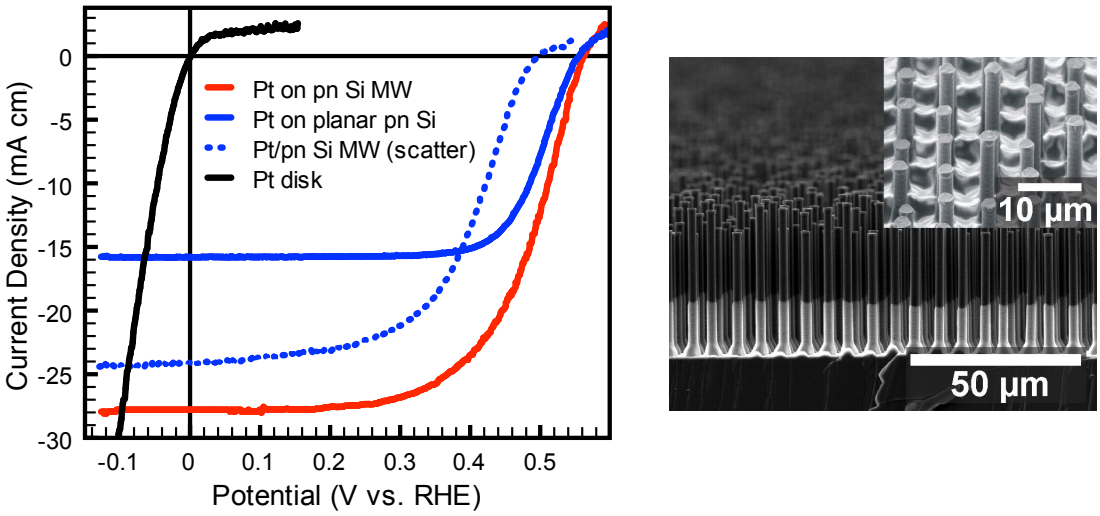

Figure 5.7. Left: $J-E$ data for Pt on planar and Si MW n^+p junctions. Data obtained in ultrapure aqueous 0.5 M H_2SO_4 and are referenced to the reversible hydrogen potential in the solution ($E(H^+/H_2)$ = -0.27 V vs. SCE). Right: SEM image of Pt/n^+p Si MW array [86]

and MW electrodes is shown in table 5.1. The measured V_{oc} for the wire array device (540 mV) is almost as high as the planar control (560 mV), but the J_{sc} is much lower due to the absorption limits in the wire array.

Table 5.1. Figures of merit for Pt-decorated planar and Si MW HER photocathodes.[86]

	V_{oc} (V)	J_{sc} (mA cm^{-2})	*ff* –	η_{HER} (%)
Pt/planar p-Si	0.3	23	0.3	2.1
Pt/ p-SiMW	0.16	7.3	0.18	1.6
Pt/n^+p planar	0.56±0.01	28±1	0.60 ± 0.02	09.6±0.9
Pt/n^+p SiMW	0.54±0.01	15±2	0.71±0.02	5.8±0.5
Pt/n^+p SiMW (scatter)	0.49	24.5	0.55	6.6

All data reported under 100 mW cm^{-2} ELH illumination and 1 atm H_2. p-Si electrodes measured in pH = 2 (H_2SO_4, 0.5 M K_2SO_4 electrolyte); n^+p electrodes measured in 0.5 M H_2SO_4

The H_2-evolving Pt/n^+p-Si wire-array electrodes were relatively stable under cathodic conditions. After 22 h of continuous operation under 1 sun illumination, with the electrode

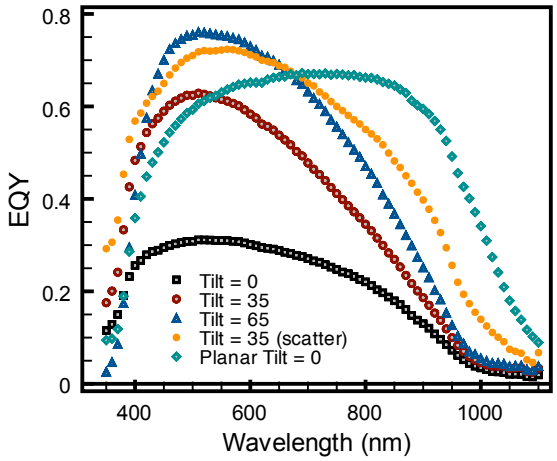

Figure 5.8. Spectral response data for the HER performance of Pt-coated planar and Si MW n^+p junction electrodes. Data obtained in ultra-pure aqueous 0.5 M H_2SO_4 while holding the electrode under short circuit conditions (0 V vs. RHE = -0.27 V vs. SCE).[86]

poised potentiostatically near the maximum power point (0.4 V vs. RHE), the *ff* of the Pt/n^+p-Si wire array electrode decreased slightly, from 0.67 to 0.62. Etching the electrode for 5 s in 10% aqueous HF restored the *ff* to 0.65, indicating the possible formation of a thin surface oxide due to incomplete cathodic protection. Additional efforts to protect the Si surface from oxidation should improve the durability of this system, as has been shown for Si microsphere photocathodes producing H_2 in aqueous HBr.[87]

5.5.1 HER spectral response

Integrating sphere measurements have shown that tilting the angle of the Si MW array relative to an direct illumination source can maximize their absorption.[66] This phenomenon was confirmed by measuring the J_{sc} while holding the sample at different angles relative to the illumination source. The data in Fig. 5.7 was collected by tilting the sample to $\sim 35°$. Figure 5.8 shows the spectral response data for n^+p Si MW array electrodes at a variety of angles as well as a planar sample at normal incidence. The highest Φ_{ext} value achieved for a highly tilted sample was 0.74, which sets a lower bound on the internal quantum yield (IQY) for the device.[86] Prior work by Kelzenberg et al. demonstrated that light absorption could be increased by introducing a silver back reflector and dielectric scattering particles at the base of the wire arrays.[66] The dashed blue line in Fig. 5.7 shows the performance of the SiMW arrays with enhanced light absorption. Although the J_{sc} increased

from 15.0 to 24.5 mA cm^{-2} the additional processing steps decreased the attainable V_{oc} and *ff* of the device. The spectral response data for the sample with enhanced absorption is shown in orange in Fig. 5.8. This system, with an HER photocathode efficiency of 6.6% demonstrates that it is possible to directly produce solar hydrogen from Si MW devices at reasonable efficiencies.[86]

5.6 Conclusions

Silicon is a good model system for investigating the effects of micro-structuring semiconductor photoelectrodes for solar-fuel applications. For dark catalysis, we have demonstrated that earth-abundant Ni–Mo HER catalysts perform almost as well as Pt when loaded onto highly structured Si MW electrodes. We have investigated directly coupling HER catalysts to p-Si electrodes, and found, similar to previous reports, that these systems only produce small photovoltages relative to RHE. However, by introducing an n^+ emitter layer, it is possible to decouple the band energetics of the Si photovoltaic device, from the HER catalysis at the surface. The device efficiency can be further increased by introducing light-trapping features into the wire array. While the results discussed so far have used Pt as the catalyst as a proof of principle, Chapter 6 focuses on integrating earth-abundant Ni–Mo catalysts with radial n^+p junction electrodes. This approach should be applicable to other catalyst/semiconductor systems as well.

Chapter 6

Earth-abundant Si microwire/Ni–Mo photocathodes

6.1 Introduction

Earth abundant catalysts have previously been coupled, through a conductive overlayer, to commercial photovoltaic cells to drive the overall water splitting reaction.[88, 89] However, earth-abundant catalysts directly coupled to semiconductor absorbers have not yet exhibited the ability to simultaneously drive the HER and to generate a significant portion of the photovoltage that is necessary to spontaneously drive the water-splitting reaction.[80, 90, 91]

In this work, Ni–Mo has been deposited onto n^+p Si MW arrays, with the goal of creating efficient H_2-evolving photocathodes that consist only of earth-abundant materials. The effects of catalyst loading, morphology, and semiconductor device characteristics on the photocathode performance have been investigated for Ni–Mo-coated n^+p junction Si MW arrays attached to a degenerately doped (photo-inactive) Si growth wafer, for Ni–Mo-coated n^+p planar junctions and p-Si MW arrays, as well as for Pt-coated n^+p-Si MW arrays. We have also prepared free-standing polymer-supported membranes based on Ni–Mo-coated n^+p Si MW microwire arrays, and have compared the performance of such systems to the behavior of the Si MW arrays that were physically connected to the crystalline Si growth substrate.

6.2 Experimental

Si MW arrays were grown using the VLS process following the same procedure detailed in Chapter 2. Figure 6.1 displays the fabrication process that was used to prepare the n^+p-Si MW array photocathodes, along with SEM images of representative Si MW arrays

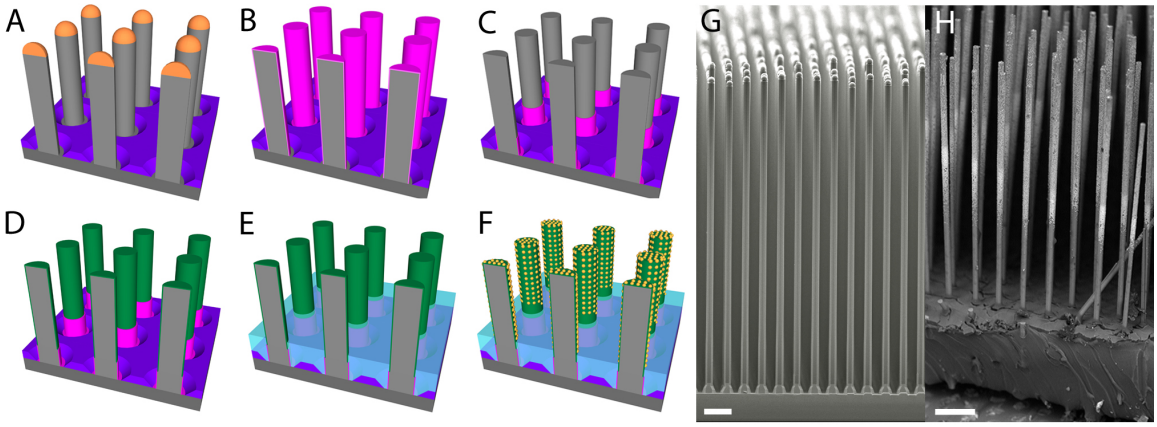

Figure 6.1. Schematic of device fabrication. A: As-grown VLS Si MW wire array. B: VLS wires after catalyst removal and thermal oxide growth. C: p-Si MW array with oxide boots. D: n^+p Si MW array after diffusion. E: n^+p Si MW array infilled with scattering particles and PDMS. F: n^+p Si MW devices with electrodeposited Ni–Mo catalyst (peeled devices were removed from the substrate before catalyst deposition). G: SEM image of as-grown wires (schematic A). H: SEM image of a fully processed device (schematic F). All scale bars are 10 μm.[92]

at the initial and final stages of device processing. The as-grown wires were 1.8–2.3 μm in diameter and ranged in height from 60–100 μm (Fig. 6.1A). Before formation of an n^+p junction onto these Si MWs, the Cu VLS catalyst was removed, and a thermal oxide was grown over the wires (Fig. 6.1B). The bottom 10–20 μm of each wire was then protected with PDMS, and the oxide was etched off the tops of the wires (Fig. 6.1C). After doping to form an n^+-Si emitter (Fig. 6.1D), the bases of the Si MW arrays were infilled with either alumina (Sasol Cerelix APA 0.5AF) or titania-based (DuPont Ti-Pure R-105) scattering particles, embedded in PDMS (30–50 μm) (Fig. 6.1E). The PDMS protected the p-Si/n^+-Si interface from exposure to the electrolyte. PDMS was removed from the tips of the wires by a 60–180 s etch in an O_2 plasma (300 mW, 300 mTorr), followed by a 30 sec dip in the PDMS etch solution, and then by a 60 s immersion in buffered HF. The doping density of as-grown wires, and the diode behavior of n^+p radial junction wires, was measured by lithographically defining contacts to the ends of individual Si wires that had been scraped from the surface.[72]

Samples were then fabricated into electrodes, either on the substrate or peeled from the substrate (not shown), before the catalyst material was deposited (Fig. 6.1F). Freestanding polymer-supported membranes were fabricated by mechanical removal of the PDMS-embedded wire arrays from the growth substrate with a razor blade. Ohmic contact was

made to the peeled membranes by electron-beam evaporation (TES, Inc.) of 200–300 nm of Au (Lesker 5N) onto the back of the peeled membrane. Ag paint was then used to mount the membranes onto a Ti foil, and electrodes were fabricated in the same way as for substrate-attached Si MW arrays. Figure 6.1G is an SEM image of the as-grown wires, and Fig. 6.1H is an SEM image of the n^+p-Si MW with deposited Ni–Mo catalyst.

6.2.1 Photoelectrochemical characterization

Photoelectrochemical HER experiments were carried out using the procedure discussed in Section 5.2. Illumination was provided by either a 300 W tungsten-halogen ELH lamp (OSRAM) or by a Newport Oriel Xe lamp that was equipped with an AM 1.5G filter. The illumination intensity was varied by use of neutral density filters (Newport). The spectral irradiance of these light sources is shown in Fig. 3.3. The light intensity was calibrated using a Si photodiode (Thorlabs UDT UV-005) that had been mounted in the same orientation as the Si working electrodes. The electrolyte was stirred continuously with a magnetic stir bar, to minimize mass-transport limitations and formation of bubbles on the electrode surface.

Before each set of experiments, all glassware in contact with the electrolyte was cleaned by soaking overnight in room-temperature aqua regia (3:1 HCl:HNO_3) and thoroughly rinsing with 18 MΩ-cm resistivity water. After each set of experiments, a polished Pt disk was used to verify that the thermodynamic potential of the proton-hydrogen (H^+/H_2) redox couple was in agreement with that calculated by the Nernst equation. All potentials are reported relative to the reversible hydrogen electrode (RHE), which has a value of -0.51 V vs. SCE for an aqueous solution at pH 4.5. Before and after each set of experiments, a fresh planar p-Si electrode (0.1 Ω-cm) was cycled electrochemically 20–100 times at 100 mV s^{-1} between 0 and -0.6 V vs. RHE, to verify that no electrochemically active contaminants in the electrolyte were electrodeposited onto the working electrode under reducing conditions.

6.2.2 Characterization of the n^+p junction

The doping densities and electrical properties of the n^+p-Si MW devices were characterized by solid-state measurements. Four-point probe measurements indicated that the electronically active dopant densities of the as-grown p-Si wires were $N_A = 1.5\ x\ 10^{17}$ cm^{-3}. Two-point measurements made on single n^+p junction wires by separately contacting the n^+-Si

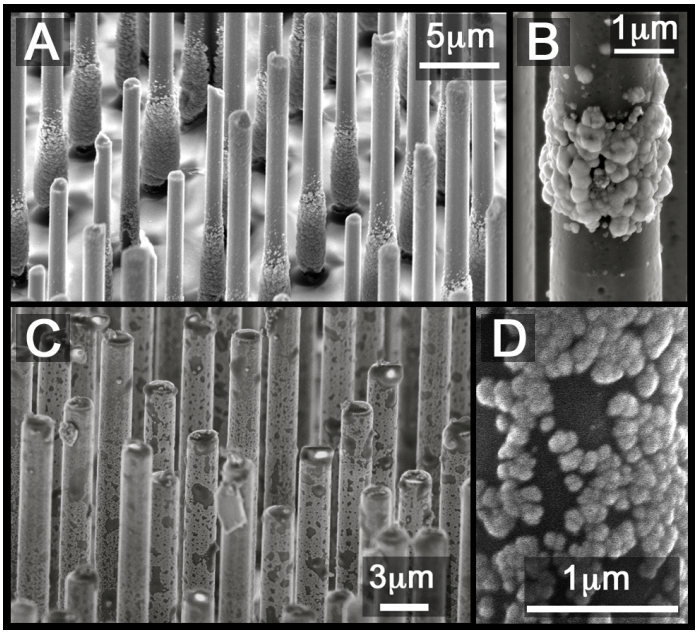

Figure 6.2. SEM images of Ni–Mo particles on n^+p Si MWs under different deposition conditions. A: Galvanostatic deposition (all catalyst at bottom), B: Deposition with no infill (Ni–Mo deposits at junction), C: Potentiostatic deposition (uniform catalyst coverage), D: High-magnification image of Ni–Mo from potentiostatic deposition

emitter and the p-Si base produced open-circuit voltages of 489 ± 12 mV and fill factors of 0.73 ± 0.04 under simulated AM 1.5G solar illumination.

6.2.3 Ni–Mo catalyst deposition

Prior to electrodeposition of a catalyst, electrodes were treated in an O_2 plasma asher (March PX-500) at 300 W for 3 min under 300 mTorr of O_2, or were treated for 5–10 min in an UV/ozone cleaning system (BioForce UV/Ozone Procleaner Plus). Both processes removed residual PDMS from the Si surface and reacted with the PDMS infill in such a fashion to allow the aqueous electrolyte to penetrate between the wires. To remove any native surface oxides, the electrodes were then etched for 10 s in 10% HF(aq).

Ni–Mo was electrodeposited from a bath that contained 1.3 M Ni^{II} sulfamate, 0.5 M H_3BO_3, and 20 mM Na_2MoO_4, with the pH adjusted to be $\sim$ 4.5 using KOH.[79] Electrodeposition was performed using a Princeton Applied Research Model 273 potentiostat, in a one-compartment cell, using a large area Ni mesh counter-electrode and an Ag/AgCl reference electrode. Samples were immersed in the deposition solution and illuminated at high intensity ($\sim$ 400 mW cm^{-2}) with an ELH-type tungsten-halogen lamp. Ni–Mo was

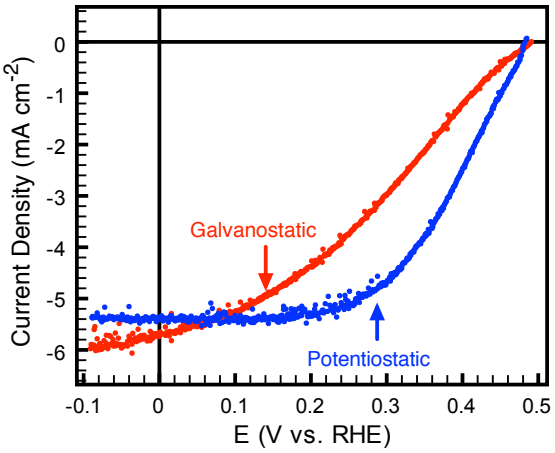

Figure 6.3. HER $J - E$ data for n^+p Si MW arrays with Ni–Mo deposited by galvanostatic (red) or potentiostatic (blue) methods. The wire arrays are not infilled with scattering particles. $J - E$ data were collected under 1 Sun illumination and are referenced to the reversible hydrogen potential in the solution ($E(H^+/H_2)$ = -0.51 V vs. SCE).

deposited using both galvanostatic and potentiostatic deposition methods. For galvanostatic depositions, the cathodic current densities were maintained at 20 mA cm^{-2} until a given total charge had passed (0.2–0.5 C cm^{-2}). Generation of 20 mA cm^{-2} of current density from the Si MW electrodes during electrodeposition of the catalyst resulted in a working electrode potential of -0.7 V vs. Ag/AgCl. For potentiostatic depositions, samples were held at -1 V vs. the reference electrode until 0.2–0.5 C cm^{-2} of charge density had passed. Under potentiostatic conditions at these more negative electrode potentials (-1 V vs. Ag/AgCl), the deposition proceeded at higher current densities (80–100 mA cm^{-2}) and required a much shorter period of time (1–3 s) to pass the specified amount of cathodic charge density.

Control devices that used Pt as an HER catalyst were produced by using electron-beam evaporation to deposit 1.5–2 nm planar equivalents of high-purity Pt (Kurt Lesker, 4N) at a rate of 0.01–0.05 nm s^{-1} onto the Si wire arrays. Immediately before deposition, the Si MW array samples were briefly etched in buffered HF, to remove native oxides.

For both p-Si MW and n^+p Si MW devices, under galvanostatic conditions the catalyst material was observed to deposit predominantly at the base of the wires (Figure 6.2A). This morphology resulted in catalytic performance with low fill factors during the electrochemical characterization of the devices (Figure 6.3). If the polymer infill did not cover the interface between the p-Si and n^+-Si emitter, Ni–Mo preferentially deposited at this junction, and

shunting of the device was observed (Fig. 6.2B). Under potentiostatic deposition, the Ni–Mo deposition proceeded more uniformly across the surface of the wire, possibly due to tuning of the interplay between hydrogen evolution and metal deposition (Fig 6.2C). Potentiostatic deposition from the Ni–Mo bath produced a uniform morphology of 100–200 nm diameter clumps, with a slightly higher catalyst loading at the tops of the wires (Fig. 6.2C and 6.2D). Optimal catalyst loading was achieved by passage of 0.2 to 0.5 C cm^{-2} of cathodic charge density during catalyst deposition. When the nominally identical potentiostatic deposition protocol for Ni–Mo was performed on planar n^+p junction Si photocathodes, the current density of the deposition exceeded 100 mA cm^{-2}, and the catalyst material readily delaminated from the surface, resulting in unstable HER activity. In contrast, when the catalyst was deposited by pulsed potentiostatic depositions (cycled between applying -1 V vs. Ag/AgCl for 0.05 C cm^{-2} and holding the electrode at open circuit for 3 s) or was deposited by galvanostatic deposition at -20 mA cm^{-2}, Ni–Mo adhered well to planar electrodes. Energy dispersive spectroscopy measurements indicated that the deposited Ni–Mo alloys were $\sim$ 85% Ni and $\sim$ 15% Mo. The Ni–Mo electrodeposition process did not allow for significant tuning of the composition of the Ni–Mo. Little or no active catalyst deposition was observed when the deposition potential was varied or when the ratio of Ni sulfamate to Na_2MoO_4 was changed in the plating bath.

6.2.4 Current density vs. potential behavior

Figure 6.4 displays representative $J-E$ data for 80–90 μm long n^+p Si MW arrays that had been coated with Ni–Mo, while Table 6.1 contains the data for all of the types of electrodes tested. Under 100 mW cm^{-2} of ELH illumination, the champion device exhibited V_{oc} = 0.485 V, J_{sc} = 10.3 mA cm^{-2}, ff = 0.45, and a solar-to-hydrogen photocathode energy-conversion efficiency, η_{H2}, of 2.2%. The average performance of Ni–Mo-coated n^+p Si MW electrodes (V_{oc} = 0.46 V , J_{sc} = 9.1 mA cm^{-2} , ff = 0.46, η_{H2} = 1.9%) was comparable to Si MW array electrodes that had Pt as the HER catalyst under the same conditions (V_{oc} = 0.44 V , J_{sc} = 13.2 mA cm^{-2}, ff = 0.47, η_{H2} = 2.7%). In contrast, Ni–Mo coated p-Si MW arrays (that did not have an n^+ emitter layer) exhibited V_{oc} = 0.14 V, J_{sc} = 6.7 mA cm^{-2}, ff = 0.24 and η_{H2} = 0.22% (Table 6.1).

The current density vs. potential behavior of representative Si MW array samples was also examined before and after catalyst deposition in contact with pH = 4.5 aqueous KHP

Illumination (mW cm^{-2})	V_{oc} (mV)	J_{sc} (mA cm^{-2})	*ff*	η (%)	#
Ni-Mo / n$^+$p Si MW (with scatterers) – Best Device					
100	485	10.3	0.45±	2.2	1
Ni-Mo / n$^+$p Si MW (with scatterers)					
100	457 ± 34	9.1 ± 2.11	0.46 ± 0.03	1.9± 0.4	5
Ni-Mo / n$^+$p Si MW (no scatterers)					
100	496 ± 5	5.5 ± 0.6	0.42 ± 0.08	1.1 ± 0.2	6
Ni-Mo / p Si MW					
100	139 ± 31	6.7 ± 0.6	0.24 ± 0.03	0.22 ± 0.1	3
Ni-Mo / n$^+$p Si Planar					
100	526 ± 23	22.3 ± 2.6	0.31 ± 0.03	3.6 ± 0.01	5
Ni-Mo / n$^+$p Si MW - peeled					
100	475 ±11	0.33 ± 0.20	0.46 ± 0.1	0.1 ± 0.04	3
Pt / n$^+$p Si MW					
100	441 ± 14	13.2 ± 5.8	0.47 ± 0.08	2.7 ± 1.3	5
Pt / n$^+$p Si Planar					
100	537 ± 19	32.3 ± 4.0	0.44 ± 0.07	7.54 ± 0.4	3

Table 6.1. Figures of merit for representative HER photocathodes, measured in H_2-purged pH 4.5 KHP buffer under 100 mW cm^{-2} ELH-type solar illumination. The error reported represents a 1σ confidence interval. For all Ni–Mo data, the catalyst was electrodeposited onto the Si device. For all devices with Pt, 1.5- 2.0 nm of Pt catalyst was evaporated using an e-beam evaporator immediately before electrochemical testing. The devices with Pt were tested after all of the Ni–Mo devices, to minimize any Pt contamination of the electrolyte used to measure the properties of the Ni–Mo films.

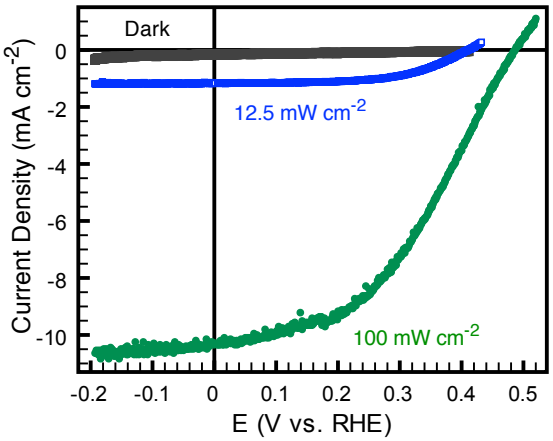

Figure 6.4. $J - E$ data for a representative Ni–Mo-coated n^+p Si MW array photocathode measured in H_2-purged pH 4.5 KHP buffer under ELH-type solar illumination (grey = 0, blue = 12.5, green = 100 mW cm^{-2}). The $J - E$ data were collected by sweeping the potential from negative to positive at 30 mV s^{-1}, and are referenced to the reversible hydrogen potential in the solution ($E(H^+/H_2)$ = -0.51 V vs. SCE).[92]

solutions. Under 100 mW cm^{-2} of ELH-type illumination, n^+p Si MW photocathodes without any catalyst exhibited light-limited photocurrent densities (J_{ph}) of 16.4 ± 1.8 mA cm^{-2} (at -0.6 V vs. RHE) whereas n^+p planar Si photocathodes exhibited J_{ph}= 29.6 ± 1.5 mA cm^{-2} (at –0.8 V vs. RHE, Fig. 6.5A). After the arrays were scraped from the degenerately doped Si(111) growth substrates, the substrates themselves exhibited negligible photoactivity for H_2 evolution.

When Ni–Mo was coated onto Si MW array electrodes, a tradeoff was observed between obtaining optimal electrocatalytic properties for H_2 evolution and the minimization of undesirable optical absorption and reflection due to the catalyst particles. Even with the addition of scattering particles, the highest observed J_{sc} value for Ni–Mo coated Si MW array electrodes was $\sim$ 10 mA cm^{-2}, whereas Pt-coated electrodes Si MW array electrodes under the same illumination conditions exhibited J_{sc} = 13.2 mA cm^{-2}. Ni–Mo-coated Si MW devices without scattering particles at the bases of the Si MWs exhibited $J_{sc} \sim$ 5 mA cm^{-2} (Table 6.1). Optimally performing devices had catalyst loadings that decreased J_{sc} by only 25–35% relative to the light-limited current density that was measured before catalyst deposition, with the heavier catalyst loadings producing significant decreases in both photocurrent density and energy-conversion efficiency.

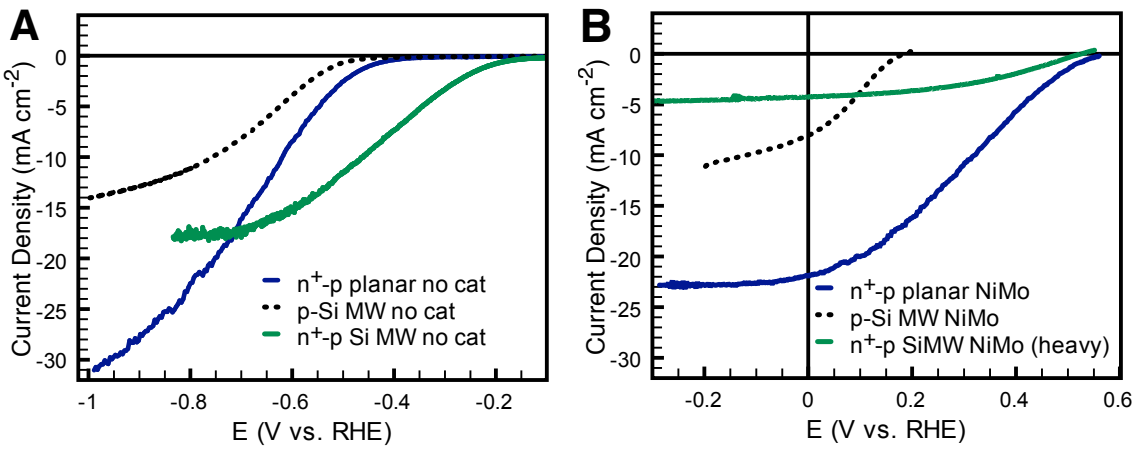

Figure 6.5. A: $J - E$ data for a representative n$^+$p planar (blue), p-Si MW (dashed) and n$^+$p Si MW electrodes with no HER catalyst. B: $J - E$ data for the same sample times in A, but with Ni–Mo catalyst. The low current density for the n^+-p Si MW electrode is due to heavy emitter doping and heavy catalyst loading. All samples measured in H_2-purged pH 4.5 KHP buffer under 100 mW cm^{-2} ELH-type solar illumination and all $J-E$ data are referenced to the reversible hydrogen potential in the solution ($E(H^+/H_2)$ = -0.51 V vs. SCE).

6.2.5 Stability

Figure 6.6 shows the performance of a representative Ni–Mo-coated n$^+$p Si MW photoelectrode that was held at E = 0.0 V vs. RHE for $>$ 60 min under 100 mW cm^{-2} of ELH illumination, with a full set of $J - E$ data collected at 10 min intervals. Over this time period, the V_{oc} remained nearly constant, but J_{sc} decreased from 10.1 to 9.2 mA cm^{-2}. The inset shows the current density vs. time for steady-state operation in which the potential of the electrode was maintained E = 0.0 V vs. RHE.

6.2.6 Spectral response

Photoelectrochemical spectral response measurements were performed using illumination from a 150 W Xe lamp that was passed through an Oriel monochromator (0.5 mm slits), then chopped at 30 Hz, and focused to a beam spot that slightly under-filled the electrode area ($\sim$ 0.05 cm^2) in solution. A calibrated Si diode was used to measure the light intensity incident on the electrode. Another Si photodiode was used to measure a beam-split portion of the illumination, and served as a continuous calibration of the output light intensity from the monochromator. A potentiostat (Gamry Series G 300) was used to maintain the potential of the Si working electrode at the formal potential for H_2-evolution (E = 0 vs.

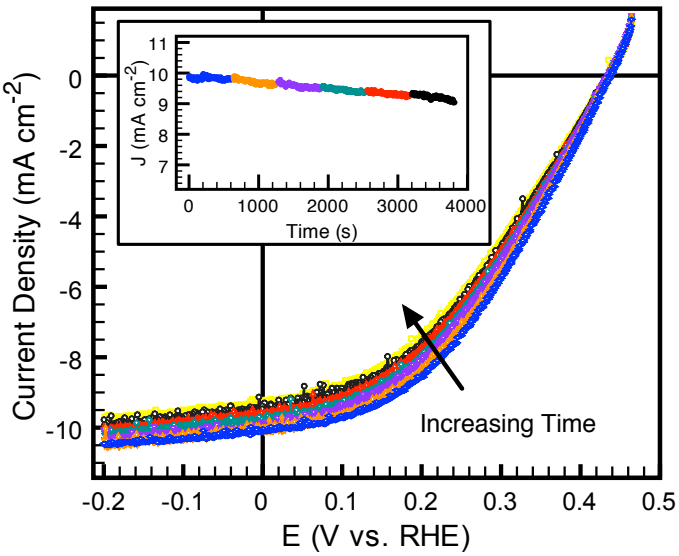

Figure 6.6. Stability testing of a representative Ni–Mo-coated n^+p Si MW photoelectrode tested in H_2-purged pH 4.5 KHP buffer. $J - E$ data were taken every 10 min. under 100 mW cm^{-2} of ELH –type illumination. The electrode was held at short circuit, i.e., at 0 V vs. RHE, between each data set (shown in inset).[92]

RHE) and to record the current produced by the sample. The chopped components of the signals were measured by use of independent lock-in detection of the sample channel (potentiostat analog output) and the calibration channel (beam-split illumination on photodiode), respectively.[86]

Figure 6.7A shows the external quantum yield (EQY) of Ni–Mo coated n^+p junction Si MW array and planar electrodes as a function of wavelength. The external quantum yield of vertically oriented Si MW arrays depends on the angle of illumination, so the electrodes were tilted slightly to maximize their current densities. After recording the spectral response data, the performance of the photocathodes was measured with cyclic voltammetry under 100 mW cm^{-2} of ELH-type illumination (Fig. 6.7B). For comparison, data are also depicted for a planar n^+p junction that had light (0.15 C cm^{-2}) and heavy (0.3 C cm^{-2}) catalyst loadings, respectively. At light loadings of Ni–Mo, the planar sample exhibited $J_{sc} = 21.8$ mA cm^{-2}, $V_{oc} = 560$ mV, $ff = 0.28$, and $\eta_{H2} = 3.5\%$. At heavier catalyst loading, $J_{sc} = 8.6$ mA cm^{-2}, $V_{oc} = 469$ mV, $ff = 0.45$, and $\eta_{H2} = 1.8\%$. After measurement of the spectral response, the Ni–Mo-coated n^+p-Si MW device exhibited $J_{sc} = 9.4$ mA cm^{-2}, $V_{oc} = 447$ mV, $ff = 0.51$, and $\eta_{H2} = 2.1\%$.

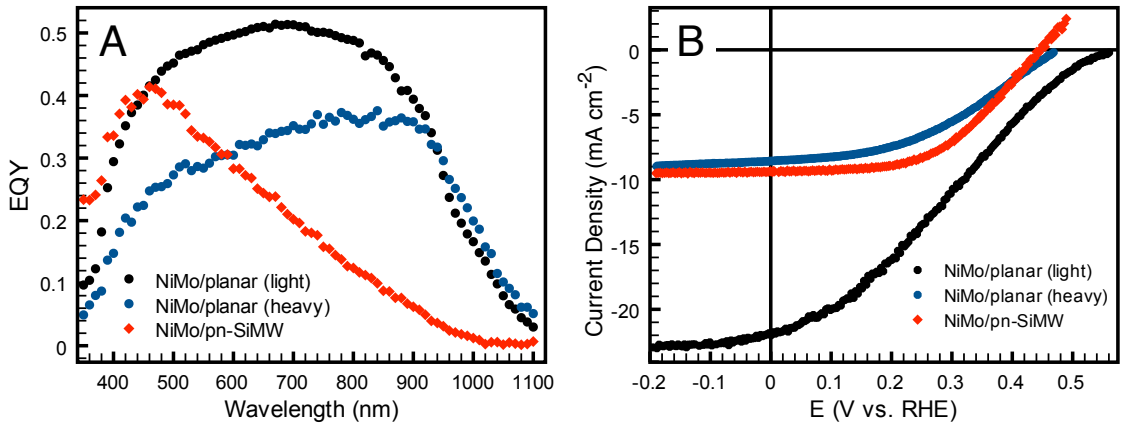

Figure 6.7. A: Spectral response (EQY vs. wavelength) data collected for Ni–Mo-coated n^+p Si MW photocathodes (red diamonds), and planar Ni–Mo-coated n^+p-Si photocathodes under high (blue circles) and low (black circles) catalyst loading. B: Corresponding $J - E$ data for the same electrodes under 100 mW cm^{-2} of ELH-type illumination. All of the data were collected in H_2-purged pH 4.5 KHP buffer.[92]

6.2.7 Free-standing polymer-supported photoactive membranes

A membrane-based artificial photosynthesis assembly would allow the photoanode and photocathode materials to be in electrical contact, while separating the gaseous products and allowing ions to pass in order to maintain charge neutrality.[1] Si MW arrays have been embedded in a membrane consisting of Nafion (a perfluorosulfonic acid polytetrafluoroethylene copolymer) and poly(3,4-ethylenedioxythiophene)–poly(styrene sulfonate) (PEDOT–PSS), and have been shown to be mechanically stable and to exhibit limited hydrogen-crossover.[93] Si MW arrays have also previously been removed from the growth substrate and evaluated as photocathodes in a flexible, free-standing membrane that contained a polymer support and embedded Si MW.[94]

Freestanding polymer-supported membranes were fabricated by peeling the PDMS-embedded wire arrays from the growth substrate with a razor blade. Back contact was made to the peeled films by e-beam evaporation of 200–300 nm of Au (Leskar 5N) onto the backs of the wire arrays. The films were then mounted onto a Ti foil using Ag paint, and electrodes were fabricated in the same way as for substrate-attached wire arrays.

When these flexible, polymer-supported Ni–Mo-coated n^+p-Si MW array structures were tested as photocathodes, the measured V_{oc} (475 ± 11 mV) was higher than that measured for substrate-attached Si MW arrays (Fig. 6.8). The measured photocurrents for these devices (0.44 ± 0.05 mA cm^{-2}) were significantly lower than for the substrate-attached

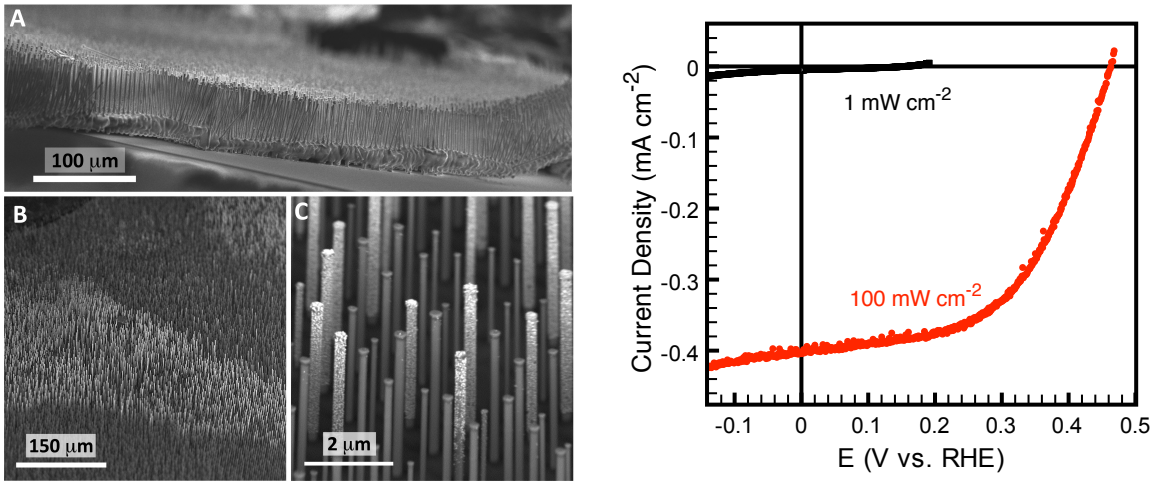

Figure 6.8. Left: SEM images of free-standing, polymer embedded n^+p-Si MW arrays. A: Si MW/PDMS film before catalyst deposition; B: Peeled film after catalyst deposition—lighter areas indicate where catalyst was deposited C: Higher magnification images of B, to show distinction between coated and uncoated wires.

Si MW arrays, but the non-uniformity of the catalyst deposition suggests that not all the wires were successfully back-contacted. Improvement in the electrical contacting scheme for a flexible membrane therefore remains of interest in the development of a complete artificial photosynthetic device.[95, 96]

6.3 Discussion

The introduction of an emitter, to produce radial n^+p junctions on the p-Si MWs, increased all of the figures of merit for photoelectrochemical hydrogen production relative to p-type Si MW arrays that did not contain the emitter layer (Table 6.1). This decoupling of the voltage-producing junction from the catalytic reaction thus provides more control over the design of the MW array electrodes for solar-fuel generation. Formation of a Si n^+p homojunction produces a photovoltage that is not dependent on the pH of the electrolyte.[97] The V_{oc} measured for the Si MW array photoelectrode was within 40 mV of V_{oc} measured for the Si MW array solid-state device. The high photovoltages observed for the free-standing, polymer-supported membrane-based devices, and the lack of observable photocurrent from the degenerately doped planar Si substrates after removal of the wires, demonstrates that the photovoltage was predominantly produced by the n^+p Si MW array portion of the device.

Many prior reports of Si-based photocathodes for the HER have used noble metals as the HER catalyst, and data were reported under strongly acidic conditions. However, in general, non-noble metal electrocatalysts for the HER exhibit limited stability under acidic conditions. The pH = 4.5 electrolyte was chosen so that the resulting photocathode performance data could be directly compared to prior electrochemical studies of the same catalyst for the HER (See Chapter 5.4.3). Polarization data measured with a Pt disk yielded a much slower onset of HER current density in pH 4.5 KHP buffer than in 0.5 M H_2SO_4 (Fig. 6.9).[98] At this nearly neutral pH, the reaction mechanism is potentially complex, because both H_2O and H_3O^+ can serve as the proton source for the generation of H_2.[8] This change in electrolyte pH accounts for the change in fill factor between the data presented here relative to prior reports of similar structures, which have displayed fill factors of 0.7, in 0.5 M H_2SO_4. Identification of the conditions that optimally balance the stability of the catalyst/semiconductor system, while maximizing the behavior of the catalytic onset, is of continued interest. Ni–Mo has been shown to be extremely stable under alkaline conditions.[26, 99] The stability data shown (Fig. 6.6) demonstrate that the Ni–Mo/Si system is a promising candidate to serve as a HER photocathode at other pH values as well. The observed decrease in J_{sc} and ff over time can be at least partially attributed to delamination of the catalyst due to H_2 bubble formation. A second electrodeposition of catalyst onto the electrode after initial testing consistently restored the catalytic turn-on behavior to its initial state.

6.3.1 Balancing catalytic activity and short-circuit current density

Figure 6.10A shows the calculated *ff* vs. the measured J_{sc} values for several different devices, both planar and SiMWs. The decrease in *ff* at higher J_{sc} values (corresponding to higher illumination intensity) reveals an important design constraint for solar energy-conversion systems. The turnover limitations of the catalyst and the limitations of majority carrier flow within the semiconductor lead to series-resistance losses in the performance of the both planar and microwire devices.[100] However, the fill factors for the Si MW samples were significantly greater than those of the planar control samples under equivalent illumination conditions. This observation is consistent with expectations that the enhanced surface area of the wire arrays provides an advantage in the effective catalytic turn-on of these devices. Figure 6.10B shows the voltage loss (V_{loss} calculated as the difference between E_{oc} and the

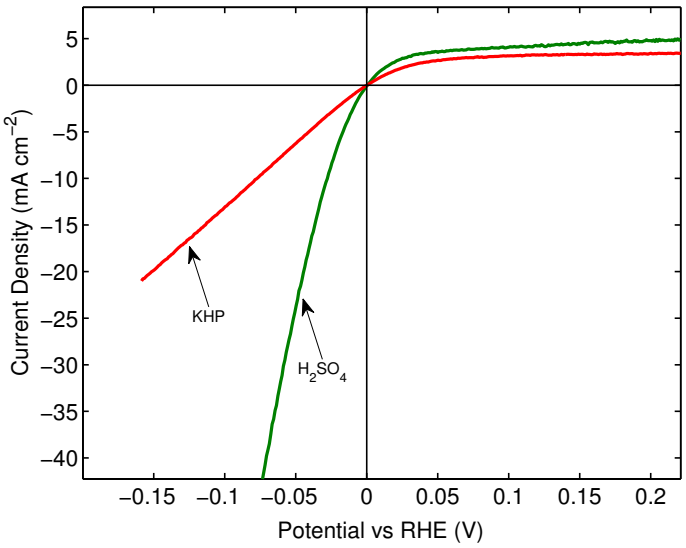

Figure 6.9. Polarization curves for a Pt disk in 0.5 M H_2SO_4 (green) and pH 4.5 KPH buffer (red)

potential of the maximum power point, E_{Pmax}). The *ff* and V_{loss} data follow the same trend, indicating that the onset of catalytic behavior near open-circuit conditions, and not just J_{sc}, can impact the device performance. The MW geometry minimizes overpotential losses, which is important for photoelectrochemical fuel-forming reactions that will not proceed unless sufficient potential is generated to drive both halves of an electrochemical reaction.

At low loading of Ni–Mo, the planar electrode showed an EQY = $\sim$ 0.5, which is 25% lower then the EQY for similar devices coated with a thin Pt catalyst. Increasing the catalyst loading decreased the EQY to $\sim$ 0.3%. However, the spectral response data (which are collected under short-circuit conditions) do not provide information about how the system operates under maximum power conditions. A comparison of the $J-E$ performance at low and high catalyst loadings reveals that although the J_{sc} was much higher in the case of low catalyst loading, the catalytic behavior was limiting, and resulted in a poor *ff* and only a slight increase in conversion efficiency at the maximum power point. Wire arrays that had an optimal catalyst loading outperformed the planar devices with high catalyst loading in *ff* as well with respect to their overall solar energy-conversion efficiency. The spectral response data for the wire arrays (Fig. 6.7A) were similar to behavior that has been that reported previously, but were uniformly lower in magnitude due to the higher loading levels of the Ni–Mo catalyst relative to a thin Pt film. When illuminated with blue wavelengths, the wire arrays performed similarly to planar devices, whereas non-optimized

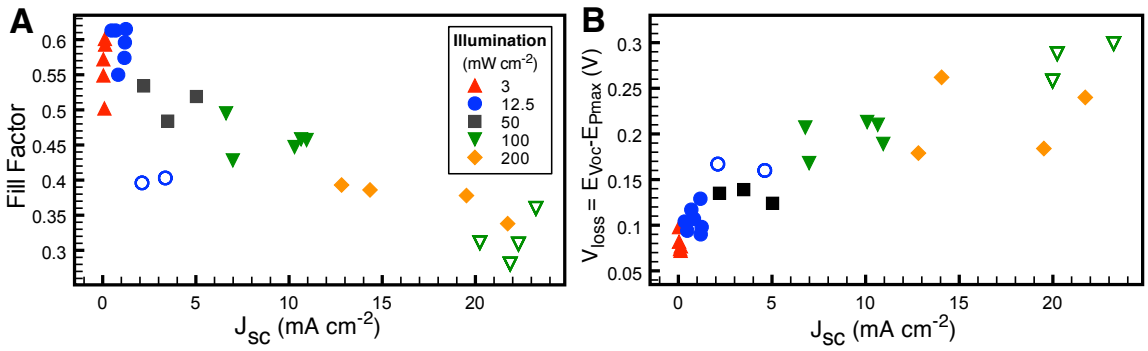

Figure 6.10. A. Comparison of fill factor vs. the attainable J_{sc} at a variety of light intensities for Ni–Mo-coated radial n$^+$p junction Si MW (closed symbols) and planar n$^+$p-Si (open symbols) electrodes in H_2-purged pH 4.5 KHP buffer over a range of light intensities. B. The voltage loss (calculated as the difference between the open-circuit potential and the potential of the maximum power point, E_{max}) for the same samples and conditions

light trapping, and concomitant absorption of photons in the degenerately doped substrate limited the red wavelength response.

6.3.2 Optical absorption in catalyst-coated Si MW arrays

To understand the absorption of light in the catalyst-coated Si MW arrays, a 2D full wave electromagnetic simulation was created to model the optical absorption. Using SEM images of electrodeposited Ni–Mo for guidance, the model consisted of a 60 μm long wire, 2 μm in diameter, with 7 μm periodic boundary conditions. Standard values were used for the optical properties of Si, PDMS, SiO_2 and the Al_2O_3 scatterers. The n and k values for Ni–Mo were measured experimentally. The model assumed unity internal quantum efficiency in the p-Si region, and internal quantum yields of zero in the catalyst and n$^+$ emitter layer.

The right side of Fig. 6.11 compares the experimentally measured EQY with the modeled absorption in the p-Si region of the wire. The data was collected near normal incidence, so there is good qualitative agreement between the maximum EQY and predicted absorption in the wires near 500 nm. Although not a quantitative comparison, the agreement between experiment and modeled absorption suggests that these devices have high internal quantum efficiency, and that the low current densities are limited by the ability of the Si MW array to absorb light when coated with a metallic catalyst.

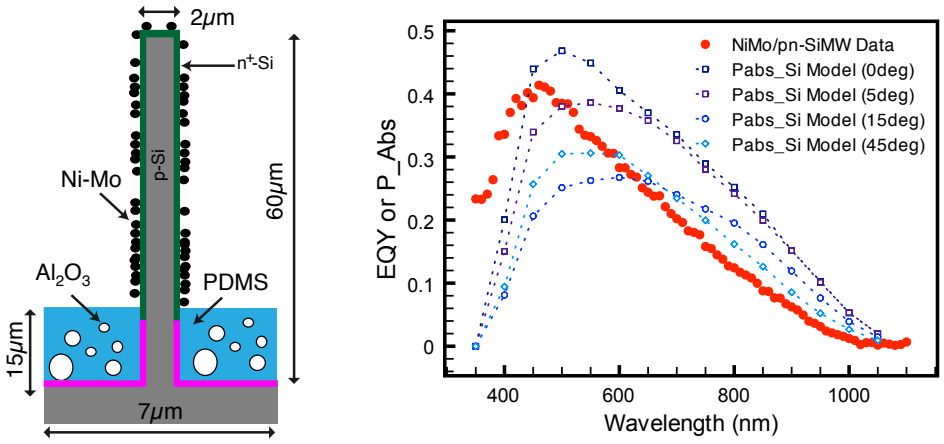

Figure 6.11. Left: Schematic of optical model. Right: Experimental EQY data compared to simulated absorption in p-Si region as a function of wavelength and angle of incident light. (Image credit: M. Shaner)

6.4 Conclusion and outlook

Arrays of radial junction n^+p-Si MWs have been coupled to earth-abundant Ni–Mo catalysts and investigated as photocathodes for the hydrogen evolution reaction. These devices show that Ni–Mo alloys can be directly coupled to high-performance semiconductor absorbers to drive the HER at efficiencies comparable to more expensive catalysts such as Pt, with promising stability under mildly acidic conditions. The balance between catalytic activity and photocurrent is clearly an important design parameter for direct solar-fuel conversion devices. The ability to remove the wire-arrays from the substrate while maintaining high open-circuit voltages is an important step in the development of a scalable, membrane-based, solar water-splitting prototype.

Further optimization of this device structure should focus on maximizing the current density of the wire arrays, and further optimizing the catalyst loading to improve the experimental fill-factor. This could be achieved by improving the light absorption with longer wires, thinner emitter layers, or better catalyst placement.

Chapter 7

Scalable processing technologies for Si microwire array fabrication

7.1 Introduction

One of the major motivating factors for the development of Si MW photovoltaic and solar fuel systems is the potential to use low-cost, high-throughput manufacturing techniques to fabricate flexible, single-crystal, solar absorbers. Silicon tetrachloride ($SiCl_4$) is a by-product of the Siemens process, which is the most widely used process to convert metallurgical grade Si to semiconductor grade poly-Si for the solar and semiconductor industries.[101] The ability to directly convert $SiCl_4$ into high-quality, single-crystal semiconductor material, without the need for further purification or wafering, makes silicon tetrachloride-based vapor-liquid-solid CVD growth a promising alternative to existing Si production methods. However, the lab-scale processes developed to date to prepare substrates for VLS growth rely on expensive, high temperature and high vacuum techniques. This chapter examines alternative fabrication techniques to those discussed in Chapter 2; specifically using soft-lithography and electrodeposition to prepare substrates for VLS growth.

Additionally, device physics modeling suggests that the optimal wire diameter for solar energy conversion is > 10 μm, a size regime that was difficult to fabricate using traditional photolithography.[102] Electrodepositing the VLS catalyst allows for the grow of wires in this size regime, while also eliminating metal waste from evaporation and lift-off of the VLS catalyst. Regenerative photoelectrochemistry was used to investigate the difference in material quality between the evaporated and electrodeposited VLS catalyst, as well as to look at the diameter-dependence on the energy conversion properties of the wire arrays.

7.2 Patterning the VLS growth substrate

The VLS Si MW arrays grown in our group have traditionally been fabricated by first growing a thermal oxide on Si wafers then using photolithography and HF etching to pattern holes that define the spacing and diameter of the wire arrays. Growing 300–500 nm of high quality SiO_2 on an Si wafer is a time and energy intensive process, requiring dedicated facilities for high temperate ($> 1000°C$)annealing of Si wafers. Using optical photolithography to pattern large areas (m^2) at < 10 μm resolution would require multiple expensive laser-written masks and mask aligners in a manufacturing environment.

Soft lithography is a cost-competitive alternative to photolithography that uses a flexible elastomers (often PDMS) to transfer a micro- or nano-scaled pattern from a master to any substrate.[103] While the master is made using expensive fabrication techniques, multiple stamps can be made from a single master, and each can be used many times, allowing this technique to be easily scaled for manufacturing. A promising alternative to the existing fabrication process for VLS substrates would be to coat the Si substrate with an inexpensive layer that could be patterned using soft-lithography to serve as the buffer layer to define the wire-array geometry. Such a material would need to be stable during the high-temperature VLS growth process and not introduce any impurities into the semiconductor material.

7.3 Reactive stamping

Initial efforts in using soft-lithography focused on using reactive wet etching, based on the protocol developed by Gryzbowski et al., to selectively etch through a SiO_2 layer in a pattern defined by a hydrogel stamp.[104–106] By soaking the stamp in an etchant, such as HF for SiO_2, the hydrogel acts as a diffusion pump, bringing the etchant in contact with the sample only where there is physical contact between the two materials.

The schematic for the fabrication of stamps for reactive micro-contact printing is shown in Fig 7.1. The master for the agarose stamp was fabricated using photolithography to pattern pillars of SU-8 photoresist on a Si wafer. This pattern was then transferred to a PDMS mold which was used to fabricate agarose stamps. The agarose stamps were then soaked in a dilute HF solution, and then pressed onto a Si wafer coated with a layer of SiO_2. The agarose/Si system was immersed in an organic solvent (mineral oil or toluene) to prevent etching to take place anywhere where the stamp did not contact the wafer.

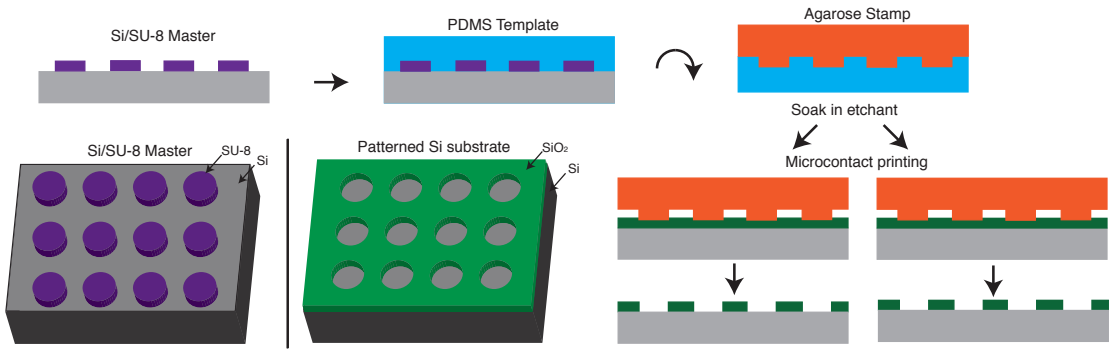

Figure 7.1. Schematic of reactive micro-contact printing. A Si/SU-8 master was used to create a PDMS template, which can then be used to make multiple agarose stamps. The agarose stamps were soaked in dilute HF solution, and then pressed into a SiO_2-coated Si wafer, resulting in a pattern of holes in the SiO_2 layer.

This technique was capable of transferring the stamp pattern to the Si wafer (Fig 7.2A, but not uniformly over large areas (Fig. 7.2B). The measured stamping rates were much lower than reported in the literature (0.2 μm h^{-1} vs. 2 μm h^{-1}).[104, 106] Efforts were made to adjust the etch rate by varying the soaking time of the stamp in HF, changing the mineral oil conditions, and by varying the concentration of HF, but no major improvement in etch rate was observed. Background etching of the unpatterned areas also limited the attainable aspect ratio of the etching using this method.

7.4 Imprint lithography

A second approach to patterning the VLS substrates used micro-transfer molding imprint lithography.[103, 107] In this technique, a PDMS stamp is used to directly transfer a pattern into a sol-gel material coating on the Si substrate. The solvent phase of the sol-gel is absorbed by the polymer stamp, creating the inverse pattern of the stamp on the Si surface. The PDMS stamps used consisted of two layers of PDMS with different formulations to prevent deformation of the PDMS during pattern transfer. The most commonly used formulation of PDMS (Sylgard 184) has a high compressibility, which can lead to deformation of the stamp, resulting in poor pattern transfer for small, high aspect-ratio features. Combining a flexible base layer with a thin, rigid top layer can improve the pattern transfer fidelity for small features.[108]

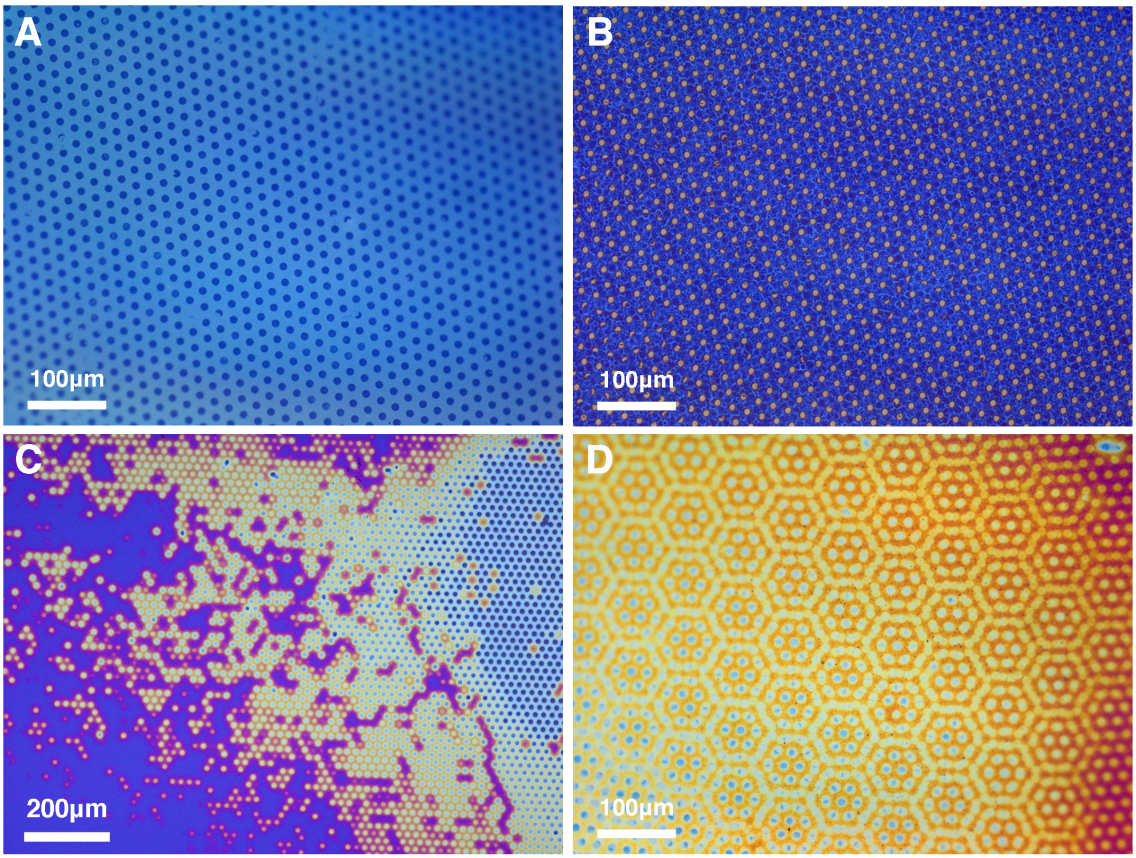

Figure 7.2. Optical microscope images of SiO_2 on Si patterned with HF etching using micro-contact stamps. A: Sample patterned without mineral oil, B: Sample patterned with mineral oil, C: Uneven etching on sample patterned with mineral oil, D: Example of pattern defect where the stamp shifted slightly during etching

Master fabrication

The rigid master for the stamps was fabricated using the same method as for traditional wire growth (Section 2.2). A positive photoresist (Shipley 1813) was spun onto a Si wafer coated with a layer of thermal oxide and patterned using optical photolithography. The exposed SiO_2 layer was then etched with buffered HF, and the photoresist was removed with acetone. Before casting the PDMS stamp, the master was silanized with tri-methyl-chlorosilane (TMCS) to prevent adhesion between the PDMS and the Si master.

Stamp fabrication

A bilayer PDMS stamp was created to combine a rigid stamping interface with a flexible substrate for more conformal patterning.[108] The high gel-strength PDMS layer was created by combining vinylmethylsiloxane copolymer, platinum-divinyltetramethyldisiloxane complex in xylene, vinyl modified Q silica resin (50% in xylene) and 1,3,5,7-tetravinyl-

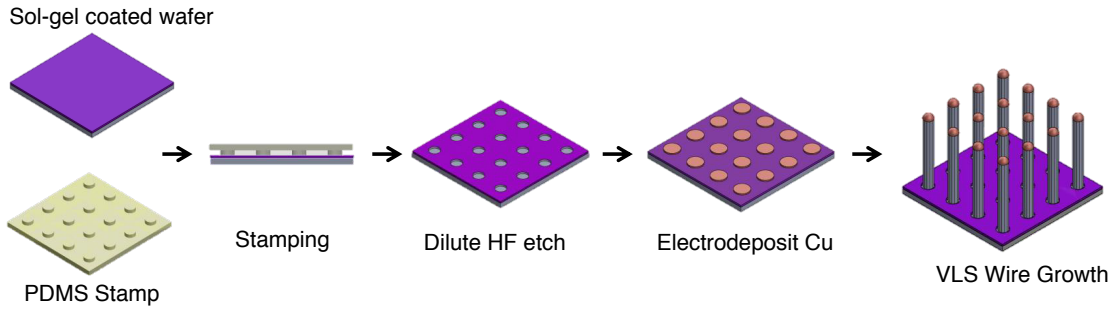

Figure 7.3. A master was prepared using lithography, and then used to make a PDMS stamp. The stamp was pressed into sol-gel spun onto a wafer while the sol-gel cured. The patterned substrate can then be used to electrodeposit Cu and grow VLS wires.

1,3,5,7-tetramethylcyclotetrasiloxane.[109] The components were mixed in a Thinky Conditioning Mixer (Phoenix Equipment Inc.) for 1 min, defoamed for 1 min and allowed to degas for 2 min. The hydride functional polydimethylsiloxane was added, and then mixed and defoamed for an additional 1 min each. The PDMS was then degassed for 8 min and then spin-coated onto the master at 500 rpm for 60 s and allowed to pre-cure for 10 min at 55 °C. The thickness of this the high gel-strength PDMS film on a planar control sample was measured to be 26 μm using contact profilometry.

The second PDMS layer was fabricated using Sylgard 184 PDMS mixed in a 10:1 ratio between monomer and curing agent. The PDMS mixture was mixed for 1 min, defoamed for 5 min, and then poured onto the master in a plastic petri dish to a total height of $\sim$ 5 mm. The stamp and master were degassed cured at 80°C for 12–24 h, and the stamp was then carefully peeled from the master. Each master can be used to make many duplicate stamps, and each stamp can be used repeatedly, making this technique easily scalable.

Stamping

A sol-gel material was spun onto degenerately doped Si (111) wafer using the following recipe: 1. Spin at 100 rpm for 5 sec while sol-gel is applied. 2. Spin at 200 rpm and close lid. 3. Spin at 400 rpm for 10 sec to achieve desired sol-gel thickness. 4. Spin at 1000 rpm for 1 sec to remove edge bead. 5. Open lid and spin at 200 rpm until color bands appear. 6. Spin at 1000 rpm to dry until uniform color seen across majority of wafer. The stamp was then pressed by hand into the sol-gel layer and allowed to cure at room temperature for 1 hour. The resulting sol gel layer was $\sim$ 200 nm thick (Fig 7.4A).

In order to keep the sol-gel pattern uniform over large areas, the master was designed

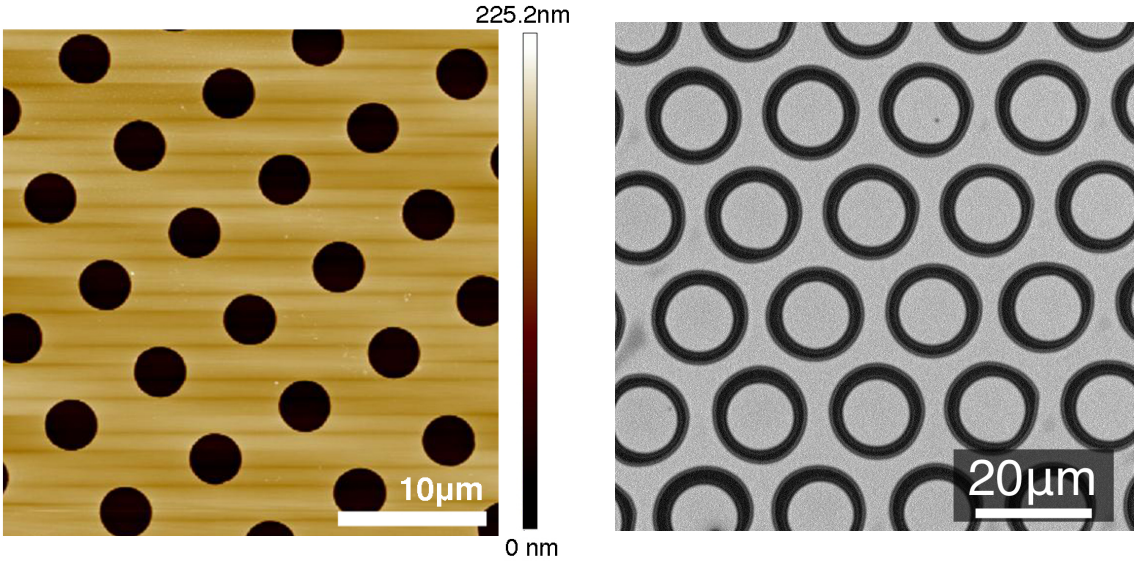

Figure 7.4. Left: AFM image of 3 x 7 μm sol-gel pattern. Right: SEM image of 10 x 20 μm pattern with PDMS pillar heights >> sol-gel thickness, resulting in the sol-gel forming a ring around each of the stamp posts, but not creating a continuous film

so that the pillars in the resulting stamp were of a similar height to the thickness of the sol-gel. If the pillars are too tall, air bubbles can be trapped between the stamp and the wafer, leading to non-uniformities in the solgel pattern (Fig. 7.4B). The optimized stamp/sol-gel system produced uniform patterning over areas greater than 20 cm^{-2}.

The sol-gel layer etches much faster than thermally grown oxide layers, but by using very dilute HF solutions we were able to remove thin layers of sol-gel from the samples without destroying the pattern. To remove any residual sol gel or native from the Si surface before electrodepositing the VLS catalyst, the samples were dipped in 1% HF for 5–10 s.

Temperature stability

To confirm the patterned sol-gel would maintain pattern fidelity during the VLS growth process, patterned substrates were annealed under N_2 at various times as temperatures, as well as under VLS growth conditions. Figure 7.5 shows SEM images of the patterned substrates before annealing and after annealing under growth conditions (H_2 with $SiCl_4$ during the growth of another sample). The diameters of the holes were increased slightly, possibly due to densification of the SiO_2 matrix, and a small amount of conformal Si growth was observed, likely due to Cu contamination from the reactor.

The ability to use wet chemical processing to remove residual sol-gel and native oxide

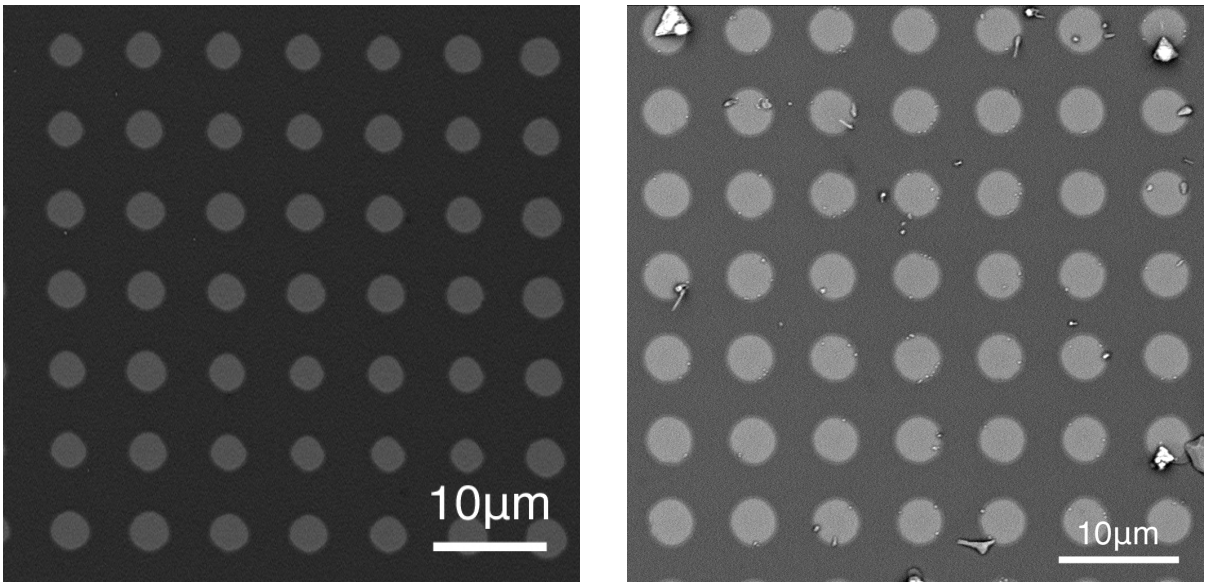

Figure 7.5. SEM image of patterned sol gel. Left: Before annealing, Right: After annealing at 1000°C in H_2 and $SiCl_4$ for 20 min

from the exposed Si, as well as the temperature/chemical stability of the sol-gel pattern, motivated continued investigation of this soft-lithography technique to pattern VLS growth substrates.

7.5 Electrodeposition of the VLS catalyst

The electrodeposition of copper is a widely used technique in the micro-electronics industry for creating interconnects in integrated circuit fabrication and printed circuit boards. It is a well-understood, high-throughput technique that does not require the use of high-vacuum conditions needed for the physical vapor deposition process that has traditional been used for Si MW substrate preparation. Previous work demonstrated that it was possible to grow Si MW using electrodeposited Au as the VLS catalyst.[44] However, the purity of the metal used as the VLS catalyst greatly affects the device performance of the resulting SiMW arrays.[52, 67] As discussed in Chapter 2, Cu impurities in Si are less detrimental to solar cell device performance than Au, motivating the investigation of electrodeposited Cu as an alternative VLS catalyst. The development of processes for Cu electrodeposition was carried out using photolithographically patterned and HF-etched SiO_2/Si(111) substrates to understand how using electrodeposited Cu affected the growth, material quality, and attainable geometry of VLS Si MW arrays.

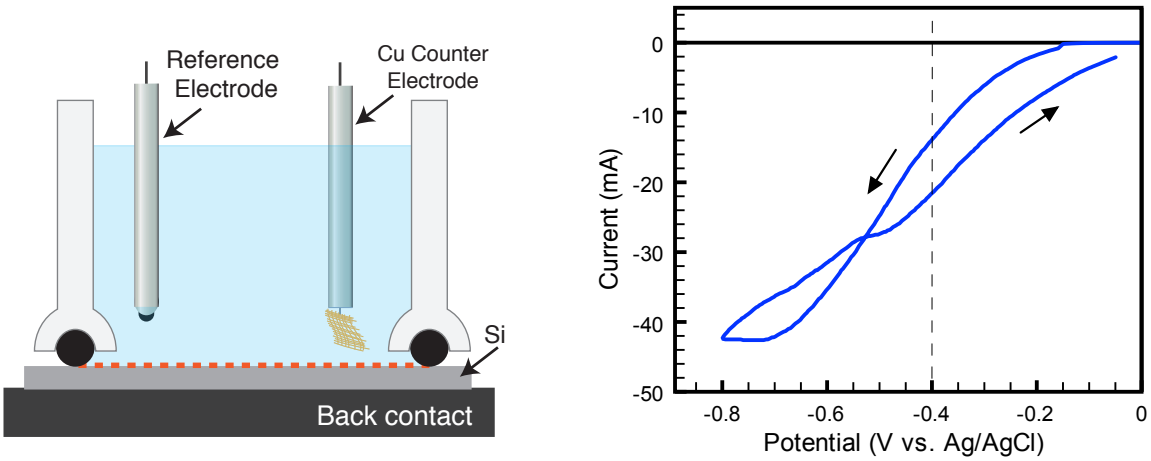

Figure 7.6. Left: Schematic of Cu electrodeposition cell. Right: Initial $I - E$ data for Cu electrodeposition on a patterned Si substrate. Potentiostatic deposition was subsequently carried out at -0.4V vs Ag/AgCl.

Experimental procedure

Electrodeposition was carried out using a pressed cell where the substrate was sandwiched between a glass cell and a stainless steel back contact using a PTFE O-ring (Fig. 7.6). A high purity (6N) Cu mesh or rod served as the counter electrode, and Ag/AgCl was used as the reference electrode. Electrodeposition was carried out potentiostatically at -0.4 to -0.6 V vs. Ag/AgCl. The potential for deposition was chosen to be halfway between the onset of deposition and the mass transport/ solution resistance limited current density (Fig 7.6).

Cu plating solutions

Several different plating solutions have been investigated as Cu sources for the VLS catalyst. The standard plating solutions available commercially consist of $CuSO_4$ salts in aqueous H_2SO_4 with additional additives to improve adhesion and control grain size.[110] A high-purity control solution (0.1 M $CuSO_4$ (5N) and ultrapure 1.8M H_2SO_4) was used, as well as plating solutions from Transene (Acidic Cu) and Clean Earth Solutions (Cu Primer). Inductively coupled plasma mass-spectrometry (ICP-MS) was used to verify the composition of the solutions, and while the results were only semi-quantitative, they indicated that the commercial plating solutions did not contain high concentrations of metals that are known to cause deep-level traps in Si.

One of the major challenges in the electrodeposition process is maintaining adhesion

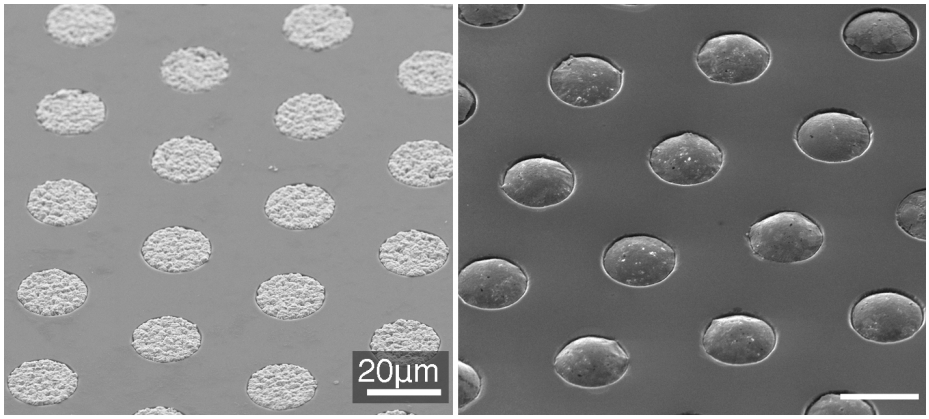

Figure 7.7. SEM images of electrodeposited Cu on a 10 x 20 μm patterned SiO_2/Si substrate before (left) and after (right) annealing at 1000°C for 20 min

between the Si wafer and the Cu disk. When removing the sample from The surface tension at the liquid-air interface often dislodges the Cu disks from the substrate. Using substrates with thicker (1.5–2 μm) SiO_2 layers and optimizing the amount of Cu deposited inside the oxide wells minimized the lift-off of Cu after electrodeposition. Figure 7.7 shows an SEM of patterned, electrodeposited Cu before and after annealing at 1000°C.

7.5.1 Controlling wire diameter

Simulations of the performance of Si MW array photovoltaics predict that for Si with minority carrier diffusion lengths > 10 μm, wires with diameters of 10 μm should be able to achieve 10% efficiency under AM 1.5G illumination.[102] While this model does not account for all of the optical properties of the wire arrays, it motivates the investigation of wires with larger diameters than have been previously been studied. Electrodeposition provides the ability to control the amount of the Cu VLS catalyst without worrying about thickness limitations due to lift-off for lithographically defined metal films, allowing the diameter of wires to be increased more than was possible using evaporation of the catalyst. Prior work in the Lewis group focused on increasing the density and diameter of VLS wire arrays by changing the photolithographic pattern and electrodepositing Au as the VLS catalyst.[111] Here, a similar approach was taken to precisely control the amount of Cu electrodeposited, and eventually correlate this with the diameter of the VLS grown microwire arrays.

Figure 7.8 shows the relationship between Cu thickness (measured by cross-sectional SEM) and the charge density passed (based on the exposed Si area). This empirical rela-

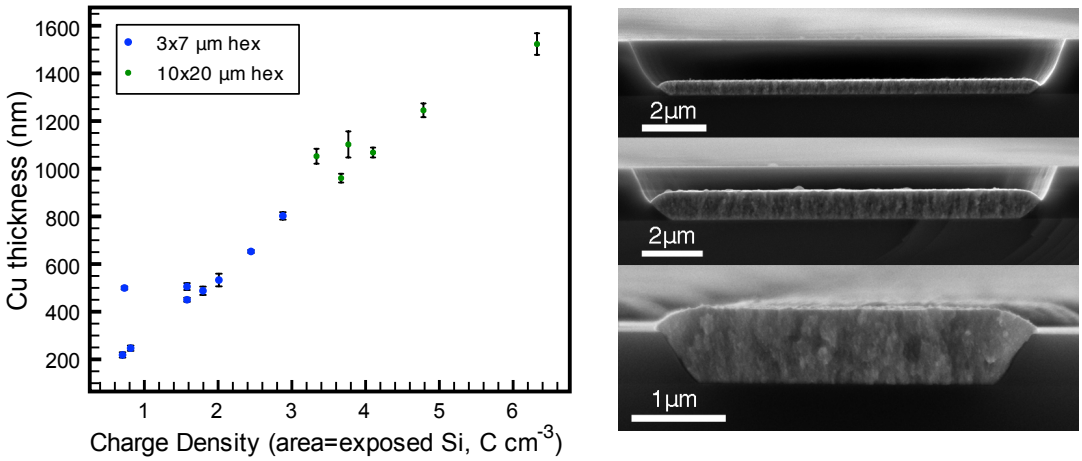

Figure 7.8. Left: Comparison of electrodeposited Cu thickness with charge density passed during electrodeposition. The data shown is for hexagonally packed patterns at different diameters and ptiches. Right: SEMs of electrodeposited Cu of different thicknesses and geometries

tionship was developed as a useful tool for predicting Cu thickness over a wide range of pattern geometries, since the measured thicknesses systematically varied from the thicknesses predicted by a simple faradaic analysis of the charge required for electrodeposition.[111]

7.5.2 Electrodepositing on Si patterned with sol-gel

Cu electrodeposition was also carried out on substrates patterned with sol-gel. The thin sol-gel layer made it difficult to maintain Cu adhesion to the substrate, as shown in the top images of Fig. 7.9. However, by using plating solutions with brightening and adhesion additives, it was possible to maintain adhesion over large areas (bottom of Fig. 7.9). Work is underway to increase the thickness of the sol-gel layer to improve adhesion of the Cu disks.

7.5.3 VLS wire growth

Arrays of VLS Si microwires were grown using the procedure discussed in Chapter 2. After electrodeposition, substrates were gently rinsed with 18 MΩ-cm water to remove any unreduced metal salts and then loaded into the growth reactor. Figure 7.10 shows SEM images of VLS Si MW arrays grown on sol-gel patterned substrates using electrodeposited Cu as the VLS catalyst (A and B show as grown wires, and C shows the wires after catalyst removal).

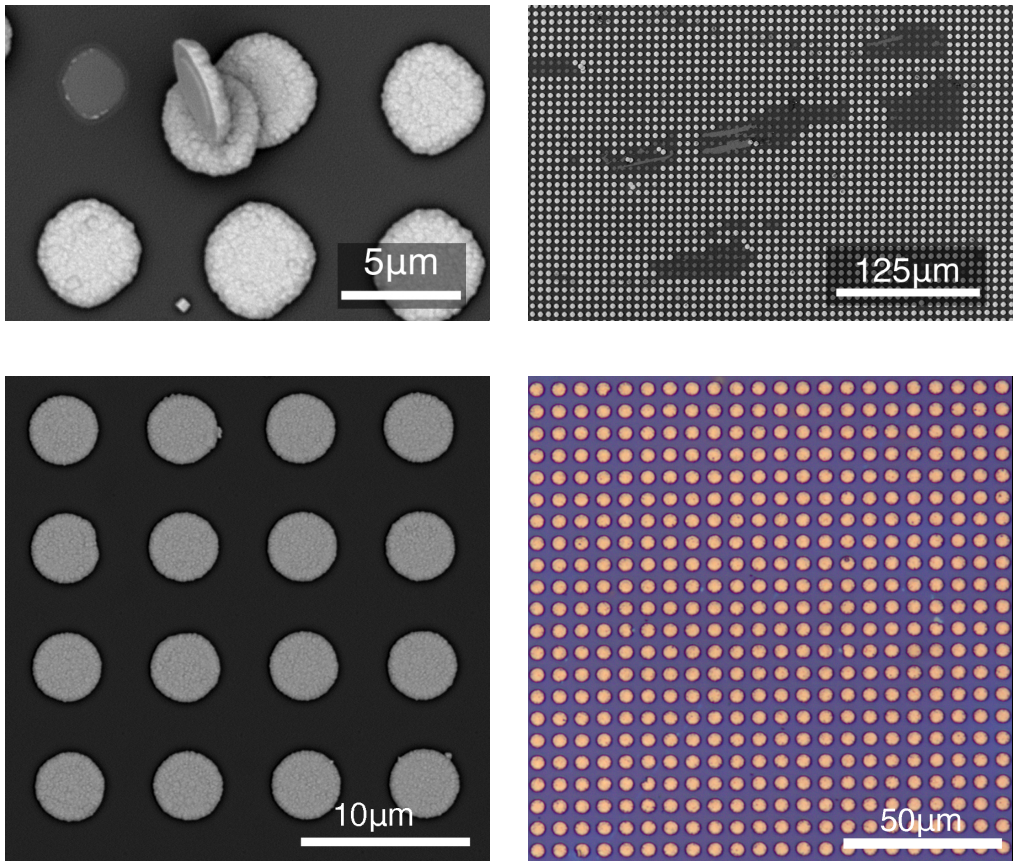

Figure 7.9. Top: SEM images of electrodeposited Cu with poor adhesion to the sol-gel patterned substrate. Bottom: SEM and optical images of electrodeposited Cu in patterned sol-gel

After growth, the Cu VLS catalyst was removed using two RCA2 cleans and then the wires were characterized using by making single-wire solid-state devices and using photoelectrochemistry. The sol-gel used to define the wire pattern etches much more quickly than a thermally grown SiO_2 layer, and was completely removed during the standard cleaning procedure. To prevent shunting between the degenerately doped base and electrolyte for these samples during photoelectrochemical characterization, the wires were "booted" using the standard thermal oxidation and partial PDMS infill procedure. (In a manufacturing setting where the final device is removed from the substrate, this step would not be necessary.)

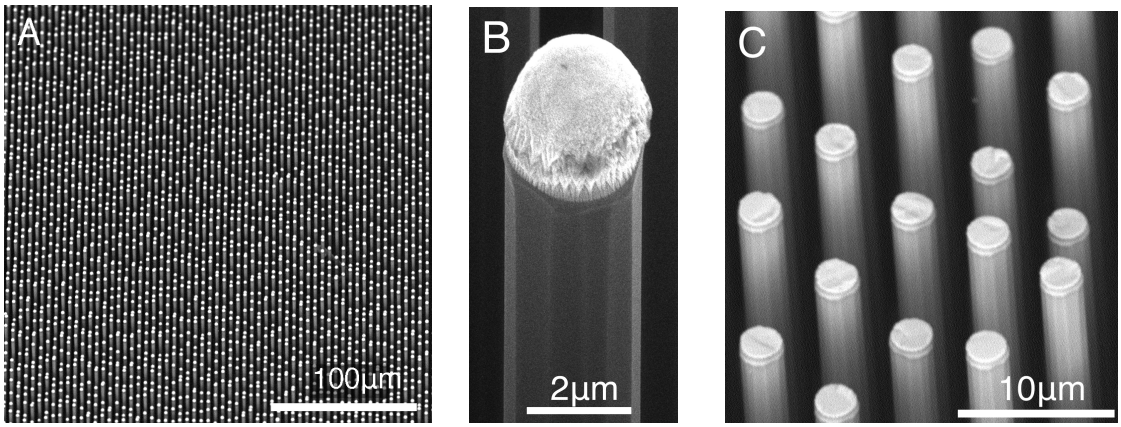

Figure 7.10. VLS wires grown from electrodeposited Cu patterned with micro-imprint lithography. A: Large area, B: Single wire, C: After Cu removal

7.6 Comparison of wires grown from electrodeposited and evaporated Cu

Wires were grown from a variety of different Cu sources to understand the effects of the Cu catalyst on the electrical properties of the wires. The effective dopant densities were tested using single-wire measurements, and the photoconversion properties were testing using regenerative electrochemistry.

7.6.1 Single-wire measurements

To compare the electrical performance of wire arrays grown from different catalysts, wires were scraped off the sample and spun-cast onto electrically insulating substrates (SiN_x-coated Si wafers). Photolithography was used to pattern 4-point contacts to individual wire arrays using and Al and Ag were evaporated to make electrical contact (Fig. 7.11).[32, 72] Micro-manipulators with tungsten probes were used to make electrical contact to each of the four contact pads. A source-meter unit (Keithly KI236) was used to source electrical current between the outer contact pads, while recording the voltage difference between the inner contacts on the wire. Using this 4-point measurement technique allows the resistance of the contacts to be decoupled from the material itself. To extract effective doping densities, the slope of the $I-V$ data was converted to a resistivity based on the diameter of the wire and the distance between the inner contacts.

Gated measurements were carried out to determine the carrier type of the unintentionally doped wires. For these measurements, the underlying Si substrate was biased during

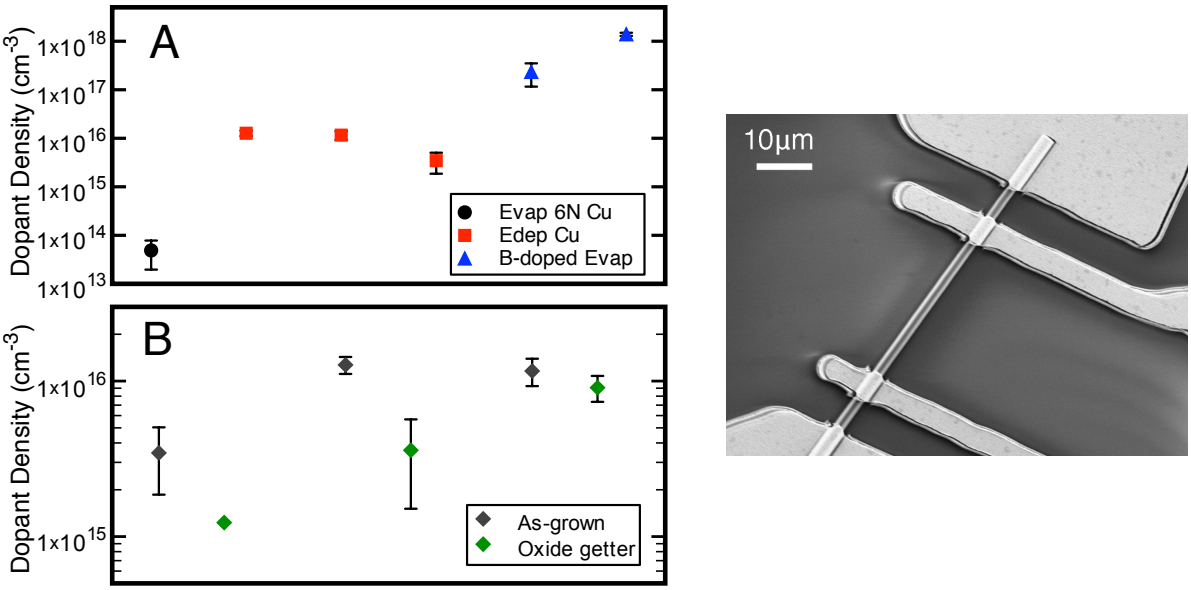

Figure 7.11. A. Dopant density of single VLS Si MWs grown from evaporated (black) and electrodeposited (red) catalysts without intentional doping, and with intentional doping (blue) B. Dopant density of single wires measured after gettering. Right: SEM of a single wire with 4-point evaporated contact

the 4-point measurement. For p-type wires, a positive gate bias induces accumulation at the surface, which increases the resistance in the wire, while a negative bias leads to depletion and decreases the resistance in the wire. (The opposite is true for n-type wires). All of the wires tested demonstrated p-type behavior.

Figure 7.11A shows the effective dopant density measured for unintentionally doped wires grown from 6N evaporated Cu and electrodeposited Cu, as well as for wires intentionally doped with boron from 6N evaporated Cu. Each data point represents the average of 5 individual wires measured from the same wire array. The effective dopant density for the wires grown from electrodeposited Cu was over an order of magnitude higher than the high purity Cu, but not as large as the optimal doping range for photovoltaic devices.

To determine if the impurities in the wires could be removed by the booting process used in p-n junction formation (Section 2.4.1), a dry thermal oxide was grown on the wires, etched off with buffered HF, and then the 4-point electrical measurements were repeated on the same samples (Fig 7.11B). This simple oxide-gettering step decreased the effective doping density of the unintentionally doped Si, but by less than an order of magnitude. To determine how the unintentional dopants affected the photo-conversion properties of the Si,

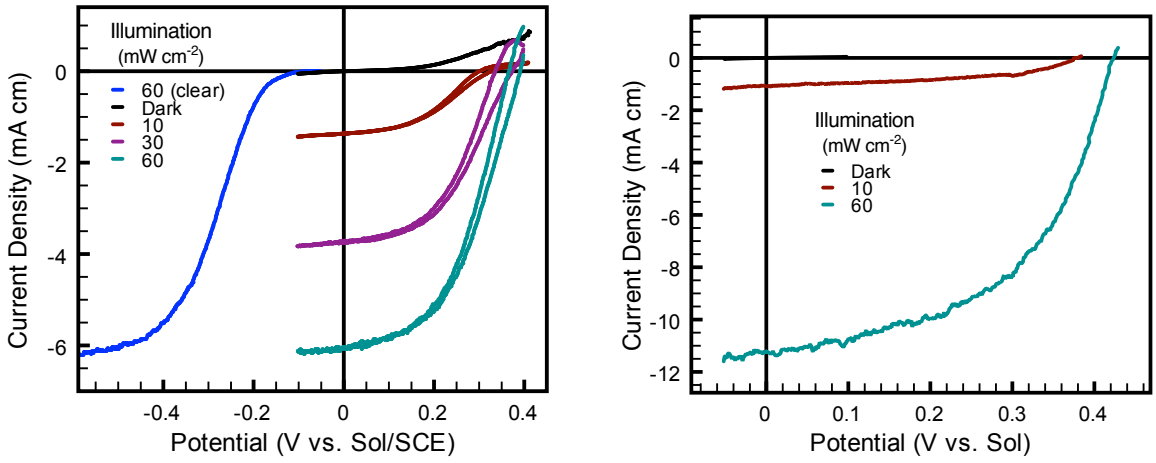

Figure 7.12. Left: $MV^{2+/+}$ $J-E$ data in of VLS wires grown from electrodeposited Cu on micro-imprint patterned substrate. Blue sweep taken in clear (no $MV^{+\cdot}$) solution. Right: $MV^{2+/+}$ $J-E$ data for wires grown from electrodeposited Cu on a 15 x 30 μm substrate. Data collected under 60 mW cm^{-2} 808 nm LED illumination

$MV^{2+/+}$ regenerative photoelectrochemistry was used to characterize the performance of p-type Si MW arrays grown from electrodeposited Cu.

7.6.2 Regenerative photoelectrochemistry

The photoelectrochemical energy conversion properties of the wire arrays were investigated using the $MV^{2+/+}$ redox couple. Details of the experimental setup can be found in Section 3.2. The left of Fig. 7.12 shows the $J-E$ data for wires grown from electrodeposited Cu on 3x7 μm square-packed sol-gel patterned substrates (wire diameter = 2.5 μm). The right of the figure shows $J-E$ data for 15 x 30 μm hexagonally patterned substrates (wire diameter = 10–11 μm). The figures of merit for these electrodes under 60 mW cm^{-2} 808 nm illumination are listed in Table 7.1. The figures of merit for both geometries of wires tested were similar to the data reported in Chapters 3 and 4, but further work is needed to fully characterize whether these wires will also perform well as n^+p homojunction devices.

7.6.3 Cu detection in VLS Si MW

Due to the larger size of the wires, several Cu-related defects were observed using scanning electron microscopy that were not as obvious for smaller diameter wires. The fabrication of larger diameter wires revealed Cu precipitates at the top and base of the wire arrays that

Table 7.1. Figures of merit for Si MW arrays grown from electrodeposited Cu

	V_{oc} (mV)	J_{sc} (mA cm^{-2})	*ff* –	η_{808} (%)
Sol-gel: 3 *x* 7 μm	405	7.1	0.49	2.3
Oxide: 15 *x* 30 μm	424	11.6	0.59	4.8

Data collected in 50 mM $MV^{2+/+}$ under 60 mW cm^{-2} 808 nm illumination

were not as easily observable in smaller wires. Figure 7.13 shows the top and bottom of Si MW arrays before and after catalyst removal, and reveals that there are Cu-related defects in both of these regions that are not removed by standard wire cleaning procedures.

Another benefit of fabricating wires with larger diameters is that it enabled the use of electron beam techniques such as microprobe analysis which have sample interaction volumes that are several microns in diameter. The Cu content of wire cross-sections was analyzed using a JXA-8200 electron probe and not shown to be above the detection limit of the machine, even in interfacial regions that are likely rich in Cu impurities. Work is currently under way in our group to selectively remove these regions, which are likely Cu-rich, to understand whether they are affecting material quality of the Si, even at very low Cu concentrations.

7.7 Predicting VLS wire diameter

A great deal of work in the literature focuses on the relationship between the size of the VLS catalyst particle, the wire diameter, and the VLS growth rate, but most experiments have focused on sub-micron diameter wires.[112–114] A prior analysis developed by Dr. Josh Spurgeon attempted to create a predictive model to correlate wire diameter with the charge passed during catalyst deposition.[111] This model was based on geometric analysis of the catalyst volume, and the catalyst/Si interactions the top of the wire, and saturation of the growth substrate with Cu.

$$V_{cat} = \frac{4}{3}\pi r_{cat}^3 \left[1 - \frac{1}{8}\left(3cos^2\varphi + (1 - sin\varphi)^2\right)(1 - sin\varphi)\right] \tag{7.1}$$

$$r_{wire} = r_{cat} cos\varphi \tag{7.2}$$

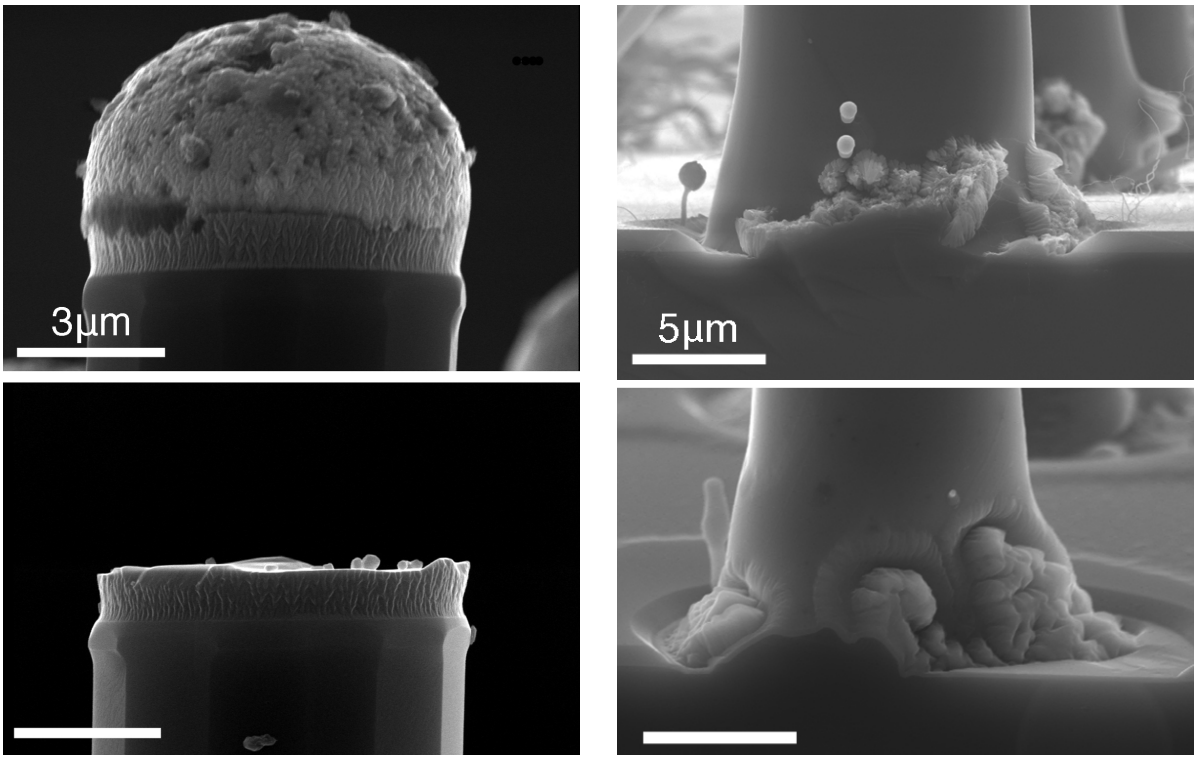

Figure 7.13. Left: SEM image of wire top before (top) and after (bottom) RCA2 catalyst removal. Right: SEM image of wire base before (top) and after (bottom) RCA2 catalyst removal

where V_{cat} is the volume of the Cu catalyst for a single wire, r_{cat} is the radius of the Cu eutectic on top of the wire, r_{wire} is the wire diameter, and φ is contact angle between VLS interface and the growth direction of the wire (45° for the Cu/Si system).[114] This model compared to experimental data as shown in Fig. 7.14. The thickness and geometry of the electrodeposited catalyst before grown was measured by cross-sectional SEM and used to calculated V_{cat}. The experimentally measured diameters (black dots) were consistently higher than that predicted by Eq. 7.2 (blue diamonds). By correcting Eq. 7.2 by a factor of 1.6, the theory provided a much better fit to the data. This factor likely accounts for the volumetric expansion of the eutectic mixture, which contains both Si and Cu. This correction to the model can be used to design the pattern/diameter of future wires grown from electrodeposited Cu.

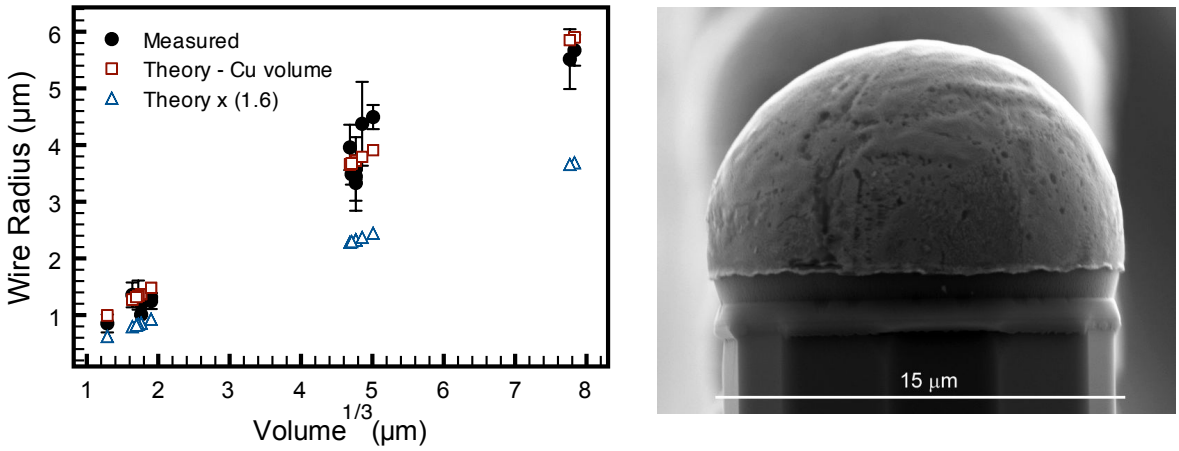

Figure 7.14. Left: Comparison of experimental and theoretical relationship between measured wire radius (black) and that predicted by equation 7.2. The red squares are the theoretical predictions scaled by 1.6. Right: SEM image of a large (15 μm diameter) Si MW

7.8 Conclusion

In this chapter we have demonstrated that it is possible to grow vertically-oriented Si MW arrays with high fidelity and material quality from electrodeposited Cu. We have demonstrated that micro-imprint lithography combined with electrodeposition is a promising alternative method to pattern the substrates for VLS wire growth and eliminates high temerature and high vacuum steps from the fabrication process.

While initial photoelectrochemical characterization of wires grown from electrodeposited Cu has demonstrated that the performance is comparable to wires grown from evaporated Cu, a detailed parametric study is needed to decouple the effects of wire geometry and catalyst material. Electrodeposition provides an ideal platform to vary the geometry of the wire arrays over several orders of magnitude in diameter and spacing. Future work should also focus on fabricating p-n junction devices from Si grown with electrodeposited Cu, since the n^+p homojunction might be more sensitive to metal impurities than the Si/liquid junctions used here.

Chapter 8

Energetics of the silicon/catalyst|electrolyte interface

While significant progress has been made in the development of Si-based photocathodes for solar-driven water splitting, there are still many fundamental questions to be answered about the physics of the semiconductor/catalyst/electrolyte interface. Experimental results have demonstrated that n^+p-Si homojunctions, when coupled to catalysts, can generate a significant portion of the potential needed to drive the water-splitting reaction. Without a diffused homojunction, however, Si-based devices have given high photovoltages when in contact with well-characterized regenerative redox couples, but not when coupled to catalysts to drive the HER (see Chapter 5). For the specific systems investigated in this thesis, it has been shown that the method of catalyst deposition plays an important role in the attainable photovoltage from catalyst-decorated p-Si electrodes.[79] To fully understand why this is the case, a carefully controlled device geometry needs to be developed and compared to device simulations.

Understanding the behavior of semiconductor/metal|electrolyte (SC/M|E) systems is complex because it is fundamentally a junction with an inhomogenous barrier height, which is not adequately described by the one-dimensional device physics models. Investigations of the ensemble behavior of electrodes with lateral variations have attracted significant attention in the electrochemical literature for over 30 years.[115] A variety of analytical models have been proposed, but the prior approaches have focused on the development of analytical solutions to explain the behavior of nano-patterned devices.[116, 117]

In this chapter, we will discuss preliminary work using finite element electrical device simulation software to simulate the band energetics and device performance of nano-patterned mixed barrier height interfaces.[118] The use of a three-dimensional simulation

allows the interactions between band-bending induced by adjacent particles to be examined over a wide range of geometries. We also outline the development of a process to create highly controlled and reproducible nano-structured catalyst patterns that can compared to theoretical models.

8.1 Introduction

It has been shown that semiconductor electrodes coated with a discontinuous metal film behave differently than when coated with a continuous film of the same material. Two approaches have been advanced to explain this phenomenon. The first, developed by Heller et al., is based on the fact that alloying the metal with H_2 can change the work function of the metal and hence increase the semiconductor/metal barrier.[119] Because the catalyst material has equilibrated its Fermi level with the H^+/H_2 redox potential, this theory predicts the driving force for the reduction reaction will only depend on the barrier height of the semiconductor/metal junction.[13] The need for non-uniform metal films can be explained by the fact that a continuous film would limit the amount of light absorbed by the semiconductor, and would thus reduce the photocurrent from the system.

Another approach to explaining the hybrid behavior of nanoscale metal particles on semiconductors is to treat the semiconductor-liquid interface as a Schottky junction with an inhomogeneous barrier height. It is well known that semiconductor-metal Schottky junctions exhibit "Fermi level pinning," where the barrier height (Φ_b) of the junction is much lower than the theoretical difference in work functions between the two materials. However, if the diameters of the metal particles are comparable to the depletion width of the semiconductor, under certain conditions, the high barrier height liquid junction can dominate the band bending in the semiconductor. This "pinch-off" theory developed by Tung et al. argues that for sufficiently small metal particles, majority carriers originating from outside the space-charge region will need to go over a potential barrier that is higher than the band edge position of the metal/semiconductor interface in order to reach the interface.[116]

Both the H_2 metal and pinch-off theories offer reasonable explanations for the behavior of SC/M|E systems with metal island nanoparticles. Work by Szklarczyk et al. and by Rossi et al. provide experimental evidence that supports the pinch-off theory.[120, 121] Szklarczyk's work systematically investigated photoelectrocatalysis for a variety of different

metals on p-Si, and found that the photo-evolution of H_2 for a variety of metal nanoparticle catalysts was directly related to the metals exchange current density for H_2 evolution in the dark.[120] Rossi's work (discussed in Section 8.1.3) used nano-patterned n-Si/Ni electrodes in contact with the 1,1'-dimethylferrocene/dimethylferrocenium ($Me_2Fc^{+/0}$) regenerative redox couple to show the electrode performance varied with particle size.

Theoretically, the pinch-off effect can be exploited to promote the desired catalytic reaction at the semiconductor surface, but there is no known precedent for using the pinch-off paradigm to guide the design of photoelectrode/catalyst systems to drive a fuel-forming reaction. A very nice summary of prior work in the field of solid-state and electrochemical inhomogenous barrier heights can be found in Rossi's PhD dissertation.[115]

8.1.1 Motivation from experimental results

The use of p-type semiconductor electrodes decorated with Pt catalysts to drive the HER has been widely reported in the literature. One of the highest efficiency photocathode devices ever reported consisted of p-type InP decorated with Pt-group metals, which generated high conversion efficiencies in acidic electrolyte.[18] In our work, we have observed that when Pt is deposited onto clean p-Si as a thin film using e-beam evaporation, the devices produce no photovoltage, and the catalytic onset is nearly identical to polished Pt (left side of Fig 8.1). However, when using electroless Pt deposition (as discussed in Section 5.4), we see a small photovoltage. The performance of these Pt-decorated p-Si electrodes is very similar under many different pH conditions (right side of Fig 8.1). XPS analysis of the Si 2p region showed that a significant amount of SiO_2 forms during the electroless Pt deposition.[79] More work is needed to understand if the observed photovoltage is due to the different geometry of catalyst particles (pinch-off), or due to the formation of a metal/insulator/semiconductor junction due to a small amount of SiO_2 between the Si and Pt particle, or both. Comparing experimental results for this system to an improved model of the pinch-off phenomenon will provide a starting point for designing the geometry of a catalyst/photoelectrode system.

8.1.2 Pinch-off

The model developed by to Tung to describe electron transport at inhomogeneous semiconductor/metal contacts can be derived by solving Poisson's equations for a system with a lateral perturbation into the boundary condition for the conduction (or valence) band

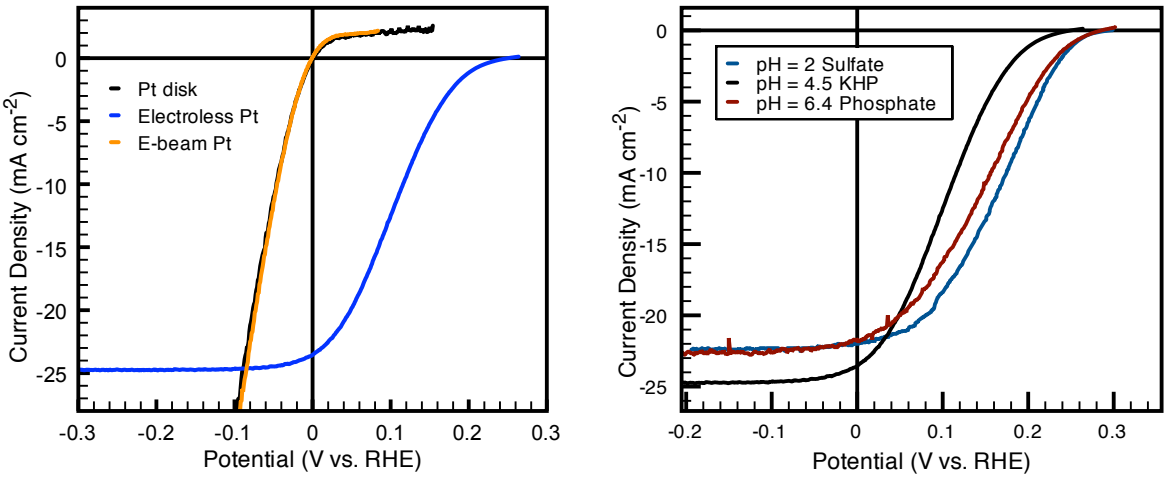

Figure 8.1. $J-E$ data for Pt/p-Si photocathodes under 1 Sun ELH illumination. Left: Varying Pt deposition method (pH 4.5 KHP buffer). Right: Varying pH of electrolyte solution. All data collected under 1 Sun ELH illumination in H_2 purged electrolyte

energy at the junction. A very similar, but less quantitative model was independently developed by Nakato et al.[122]

Starting with the following boundary condition at the surface:

$$U(x,y,0) = \Phi_E(x,y) = \Phi_E^o + \delta(x,y) \tag{8.1}$$

by applying the depletion region approximation, the potential (U) as a function of the depth into the semiconductor (z = 0 at surface) can be determined. For a simple geometry such as a circular, low barrier-height patch with radius R_0, the potential behind the center of the dot can be calculated (in cylindrical coordinates) from Eq. 8.2, where U_{bb} is the band-bending in the semiconductor, W is the depletion width for the unperturbed system, Δ is the difference between the two barrier heights (Φ_E - Φ_M), and R_0 is the radius of the metal particle.[115]

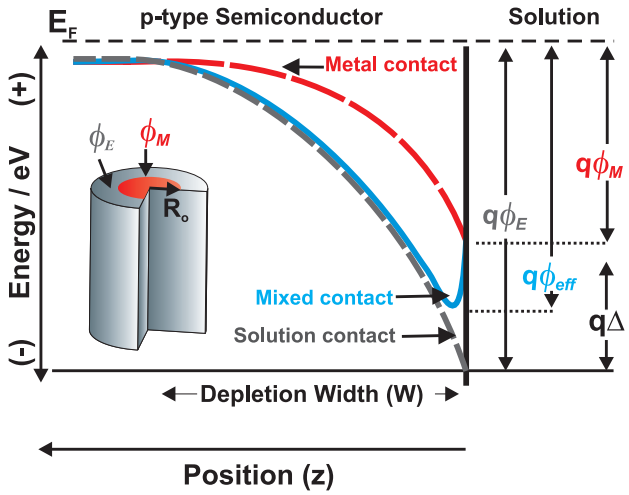

Figure 8.2. The valence band edge as a function of position in a p-type semiconductor behind a mixed barrier height contact, where Φ_E is the barrier height between the semiconductor and solution and Φ_M is the barrier height between the semiconductor and the metal. A particle with a sufficiently small radius will be pinched-off, meaning that the effective barrier height (Φ_{eff}) across a mixed contact junction will be much larger than that of the low barrier height metal contact. The extent to which pinch off occurs in a given system depends on Δ, the band bending, and the depletion width in the semiconductor.[121]

$$U(0,z) = U_{bb}\left(1 - \frac{z}{W}\right)^2 - \Delta\left(1 - \frac{z}{\sqrt{z^2 + R_o^2}}\right) \tag{8.2}$$

$$R_o = \frac{W\Delta}{2U_{bb}} \tag{8.3}$$

$$U(0,z) = U_{bb}\left(1 - \frac{z}{W}\right)^2 - \Delta\left(\frac{R_o^2}{2z^2}\right) \tag{8.4}$$

When this potential reaches a local maximum, a test charge moving behind the patch will have to overcome a potential barrier larger than that at the interface, and is hence said to be "pinched-off." Mathematically, this will occur when R_0 is less than or equal to the right side of Eq. 8.3.

This then predicts that in the regime in which the scale of the metal particle is comparable to, or smaller than, the depletion width of the semiconductor, the current density depends strongly on the band bending of the semiconductor as well as on the spatial dependence of the barrier height.[121] If the metal nanoparticles are small and well dispersed on the semiconductor surface, the effective barrier height of the system will be controlled

by the semiconductor/electrolyte interface (Figure 8.2). In the limit of a very small particle the patch can be approximated by a point dipole, and Eq. 8.2 can be approximated by Eq. 8.4.

8.1.3 Prior work on the n-Si/Ni system

Motivated by the theory developed by Tung, Rossi et al. investigated the effect of nano-patterning a low barrier height metal contact on n-Si, and then making a high barrier height $Me_2Fc^{+/0}$ liquid contact to the whole system. Arrays of Ni nanodots of various sizes were patterned onto lightly doped (N_D = 8 x 10^{14} cm^{-3}) planar n-Si substrates using nano-sphere lithography prior to making electrodes. Using bi-layers of polystyrene nano-spheres deposited in a Langmuir-Blodget trough, hexagonally packed patterns of 60, 120, 240, and 480 nm Ni patches with pitches of 200, 400, 800, and 1600 nm, respectively, were deposited by sputtering. With the same filling fraction of metal for all the geometries, the $J - E$ behavior of large particles was similar to a continuous metal film, while smaller particles ($R < R_o$) behave like a high barrier height n-Si/liquid contact. The experimental data could be modeled using the modified pinch-off equation, by assuming that the smallest (60 nm) particles were acting as point dipoles on the surface. While these experiments verified that metal particle size can affect the junction properties at a Si/M|E junction, the metal filling fraction was relatively low (7–9%) and the existing model cannot account for the effects of nearby particles, which induce band-bending profiles that overlap.

8.2 Catalyst loading

Many of the designs for an integrated photoelectrochemical energy conversion device require that the catalyst material be in direct contact with the semiconductor absorber and the electrolyte. This layer of catalyst will affect light absorption, band energetics, and the kinetics of the desired reaction. The work by Tung and Rossi has been cited as motivation for adding discontinuous metal catalyst layers to fuel-forming photocathodes.[78] However, Tung's analytical model, which predicts that high effective barrier heights can be attained by controlling the geometry at a SC/M|E interface, requires that the low barrier height patches do not interact. Since these low barrier height metal patches are also serving as catalysts for a chemical reaction, their spacing limits the catalyst loading at the surface.

Name	Diameter	Pitch	Packing	Coverage
–	μm	μm	–	%
3 x 7 sq	3	7	square	14
2.5 x 7 sq	2.5	7	square	10
1 x 10 hex	1	10	hex	0.9

Table 8.1. Geometries of patterned Pt on p^+Si electrodes to test catalyst loading

While the issue of catalyst loading is often addressed in fuel cell literature, few studies have focused on the loading effects of catalysts for fuel-evolving photoelectrodes.[78, 123] To understand whether catalyst-loading issues would limit the application of the pinch-off model the effect of catalyst loading was investigated using Pt patterned on degenerately doped planar p-type Si.

Degenerately doped p-Si (ρ <0.001 Ω-cm) was patterned with Pt islands (geometries listed in Table 8.2) using standard photolithographic procedures and e-beam evaporation. Electrodes were fabrication using the procedure discussed in Section 3.2.2. Linear sweep voltammetry (LSV) was used to characterize the catalytic onset of the HER in H_2-purged 0.5 M H_2SO_4. Before collecting data, electrodes were cycled between -0.38 and 1.05 V vs. SCE to clean the Pt surface and generate reproducible catalytic behavior. For planar films, there was very little variation between the thickness of evaporated Pt. Figure 8.3 shows $J - E$ data for 2, 5, and 10 nm of Pt evaporated onto p^+Si, as well as the performance of a polished Pt disk. All electrodes were able to pass nearly 100 mA cm^{-2} at only 100 mV overpotential.

Figure 8.4 shows HER polarization data for patterned p^+ electrodes with 5 nm of evaporated Pt, as well as SEM images of the patterns. The catalyst loading for electroless Pt is shown for comparison. At higher coverages (> 10%), the performance of the patterned electrodes is comparable to a continuous film, reaching > 60 mA cm^{-2} at 100 mV overpotential, which is much greater than the expected photogenerated current from a solar-fuel device. However, at very low catalyst coverage (< 1%), the HER performance drops significantly, indicating that the Pt loading is not high enough to keep up with the rate of carriers generated in the semiconductor electrode. The 10% catalyst coverage is similar to the ∼7%

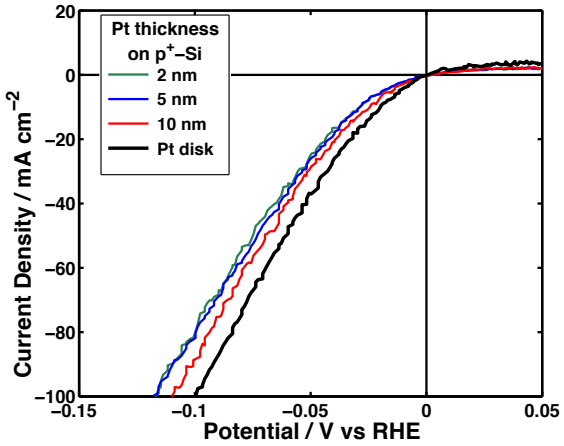

Figure 8.3. HER polarization data for Pt-coated p^+Si electrodes in H_2-purged 0.5 M H_2SO_4

catalyst loading used for Rossi's Ni/Si|$Me_2Fc^{+/0}$ experiments, which suggests that for Pt, the performance of electrodes with this catalyst coverage should not be severely limited by catalyst loading. Modeling is needed to understand how higher catalyst loading and closely spaced metal particles affect the band bending at the semiconductor/liquid interface.

8.3 Modeling inhomogeneous semiconductor contacts

8.3.1 Finite element device physics modeling

Sentaurus TCAD (by Synopsis) is a robust semiconductor device physics simulation tool that has been successfully used to simulate three-dimensional geometries such as Si MW solar cells and nano-structured thin film solar cells.[124, 125]

For computational efficiency, one quadrant of a unit cell was simulated using Neumann boundary conditions to approximate periodicity of an array. The structure simulated was a square column of Si, 100μm thick with the width equal to half the pitch between the particles. The metal, low barrier height, patch was simulated as an ideal Schottky contact, consisting of 1/4 of a circle centered on the origin. Based on the symmetry of the boundary conditions, this will produce the effect of a square-packed array of metal patches. The liquid contact was defined as a separate Schottky contact with a different barrier height covering the rest of the Si surface. The definitions used by Sentaurus to define a Schottky contact can be found in Appendix A. It it is important to note that all barrier heights are measured relative to the conduction band edge of the semiconductor, so both n and p type

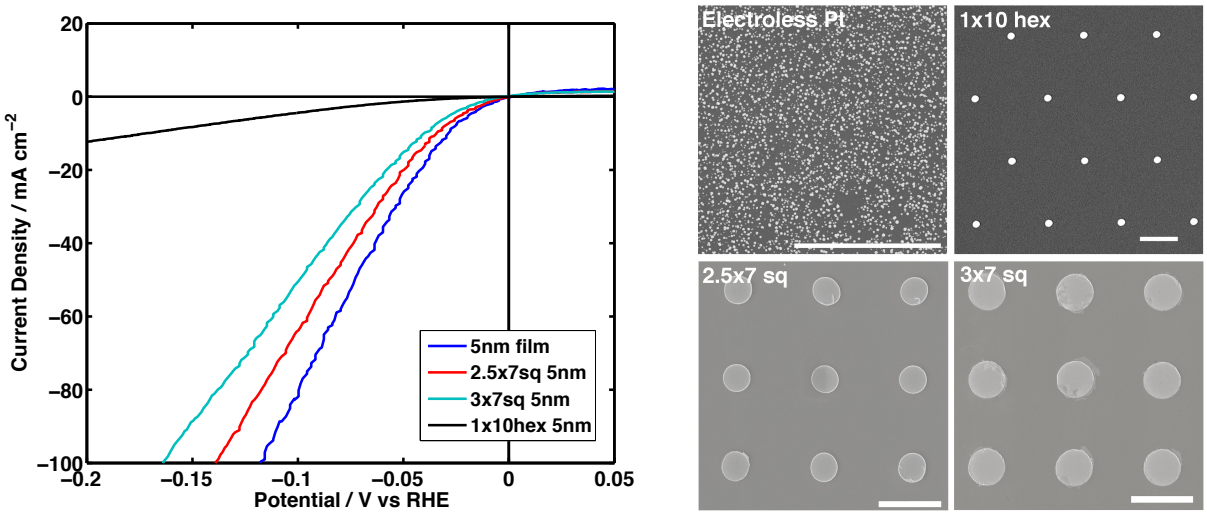

Figure 8.4. Left: Polarization data of the HER activity for various patterns of Pt on p^+-Si electrodes (Data collected in H_2-purged 0.5 M H_2SO_4.) Right: SEM image of different patterns. Electroless Pt shown for comparison. All scalebars = 5 μm.

semiconductors must use the same sign convention. Based on Rossi's work, Φ_M was defined as 0.62 V, Φ_E as 0.84 V, and N_A as 8 x 10^{14} cm^{-3} though values were varied in subsequent simulations. (A full list of the Sentaurus input parameters can be found in Appendix A)

The model was first tested using the Ni/n-Si|$Me_2Fc^{+/0}$ system to verify the analytical results from Rossi's work. Figure 8.5 shows the conduction band edge vs. position into the wafer behind the center of the metal patch $(x, y = 0, 0)$ for a variety of Ni particle sizes and compares the simulation results with the point and patch dipole models (Eqs. 8.2, 8.4). As expected, the conduction band energy reaches a maximum that increased with decreasing the size of the metal patch. For the 60 nm particles, there is excellent agreement between the analytical models and the conduction band edge calculated by Sentaurus (right side of Fig 8.6).

This model system was also used to investigate the effect of metal coverage of the band bending within the semiconductor. For 120 nm Ni particles, the pitch between particles was varied between 160 and 560 nm, corresponding to a change in metal coverage from 44.2% to 3.6% (left of Fig. 8.6). As expected, increasing the metal coverage decreased the conduction band maximum near the surface. Interestingly, the magnitude of the change of the conduction band maximum is less than 100 mV over this range of metal coverage

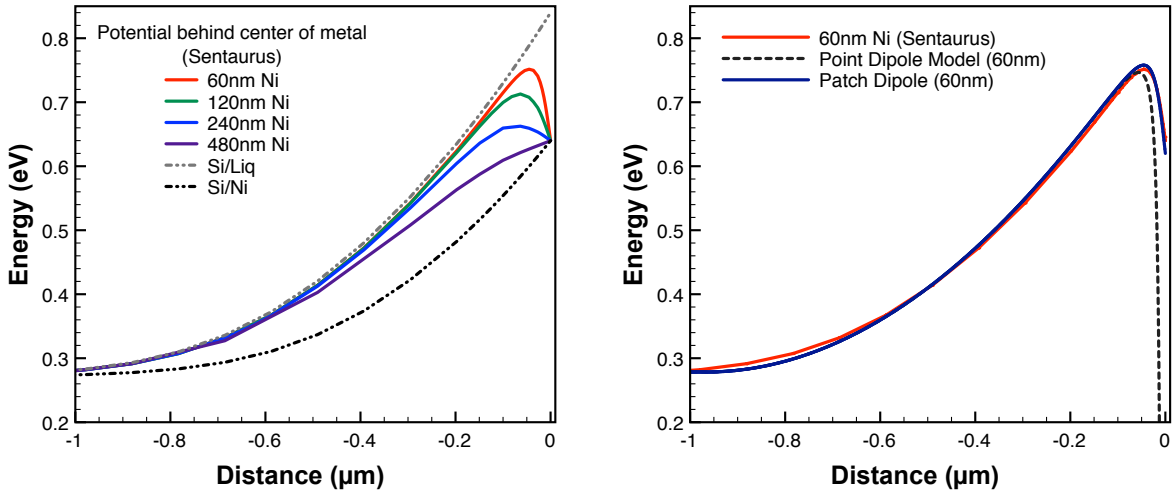

Figure 8.5. Simulated band edge positions behind Ni circle on n-Si in contact with high barrier height electrolyte in the dark. Left: Varying particle diameter and spacing of Ni. Right: Comparison of Sentaurus, point dipole and patch dipole model for a 60 nm Ni patch

for both 120 and 60 nm Ni particles (right of Fig. 8.6). Experimental verification of this phenomenon should be carried out to determine whether or not this is an artifact of the model.

Dark $J-V$ curves were generated and compared to the behavior predicted by Rossi's work (Fig. 8.7). For simulations with larger particles, the $J-V$ performance approached that of a pure Ni/Si Schottky contact, while smaller patterns were closer to the pure liquid junction. Although these trends were similar to those observed experimentally, the ideality factors are different from the analytical model developed by Rossi to match prior experimental data (symbols). Some effort has been made to vary the Sentaurus model parameters to improve the correlation, but the analytical models used by Rossi include several empirically measured parameters, and had a slightly different geometry, so future efforts will focus on fabricating patterns that better match the modeled geometry.

8.4 Modeling the p-Si/Pt/HER system

In order to accurately model the Pt/p-Si system, a value for the Pt/p-Si barrier height is needed. Experimental measurements of barrier heights for evaporated Pt on moderately doped p-Si ($N_A = 1$ x 10^{17} cm^{-3}) indicate that this contact is ohmic, but there are varying reports in the literature for Pt/p-Si Schottky contacts measured in a variety of ways ranging

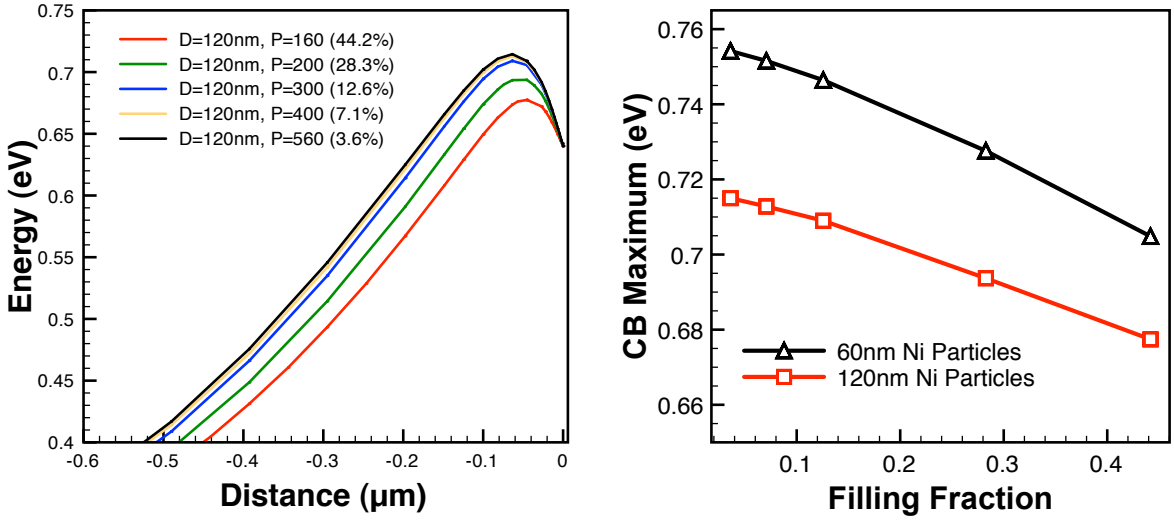

Figure 8.6. Left: Simulated band edge positions behind Ni dots for n-Si/Ni/electrolyte system varying spacing of Ni dots. Right: Conduction band maximum vs. filling fraction of metal at junction

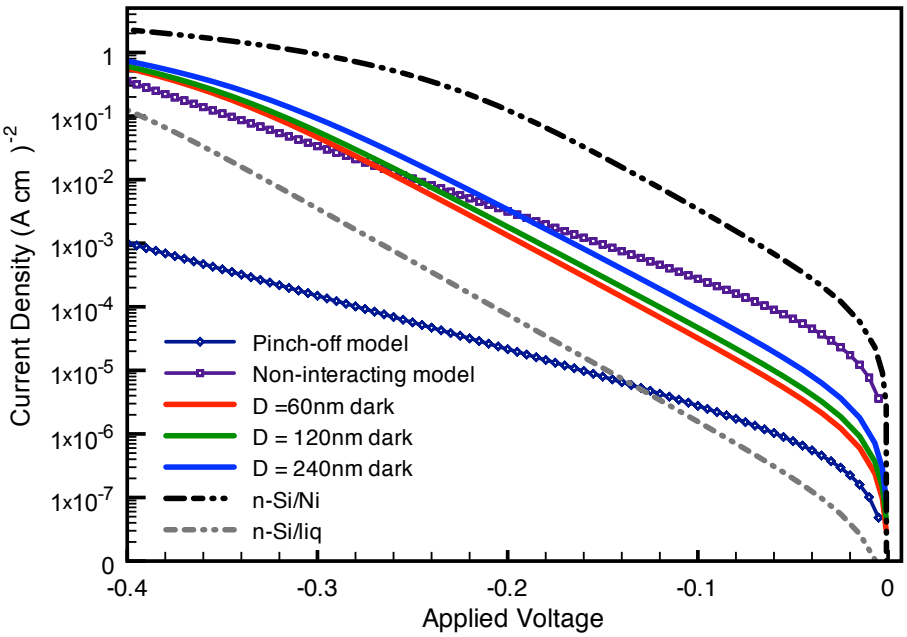

Figure 8.7. Simulated $J-V$ data for various Ni particle sizes, as well as the prediction from theory for a pinched off and non-interacting model for the diode behavior of the device

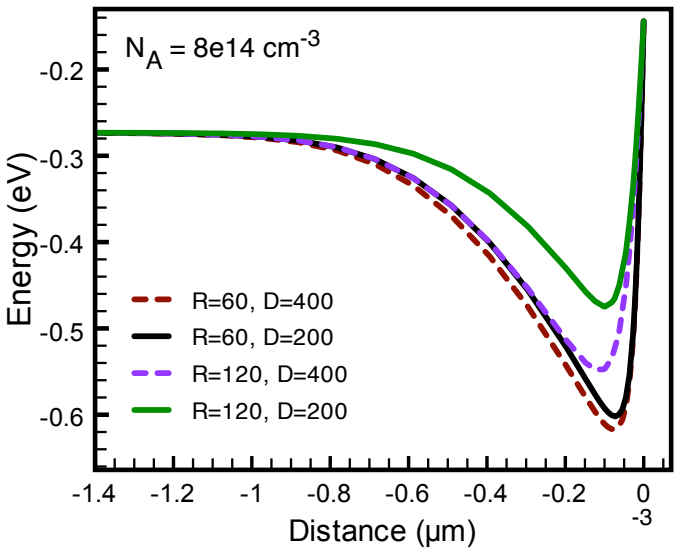

Figure 8.8. Simulated valence band edge positions behind low barrier height Pt patches on p-Si in contact with aqueous pH = 0 electrolyte

from 0.23 to 0.39 eV.[126, 127] For this work a barrier height of $\Phi_M = 0.12$ V (which is equivalent to 0.98 V relative to the conduction band edge as dictated by Sentaurus convention) was chosen based on the widely reported n-Si/Pt barrier height of 0.9 eV.[76] Assuming an experimental pH of 0, $\Phi_L = 0.39$ V based on the expected band edge positions of Si. The doping density, geometries, and SRV values were initially kept consistent with the n-type model to minimize the number of variations introduced.

Figure 8.8 shows the valence band edge vs. position into the p-Si wafer behind the center of the metal dot $(x, y = 0, 0)$ for a variety of Pt particle sizes. Similar to the n-Si/Ni system, the valence band minimum varies with Pt particle size, and decreases as the catalyst loading is increased. Due to the fact that Δ is much larger for the Pt/p-Si system than for the Ni/n-Si system, the change in the valence band minimum is much more pronounced for both the 60 nm and 120 nm particles upon changing the catalyst loading.

8.5 Experimental design

In order to experimentally test the pinch-off phenomenon for a catalytic system, a reproducible experimental platform is needed. While varying particle size was effective for testing the size dependence for an electrochemical system with fast electron-transfer, the difference in edge area for these systems might introduce variability between samples based on cat-

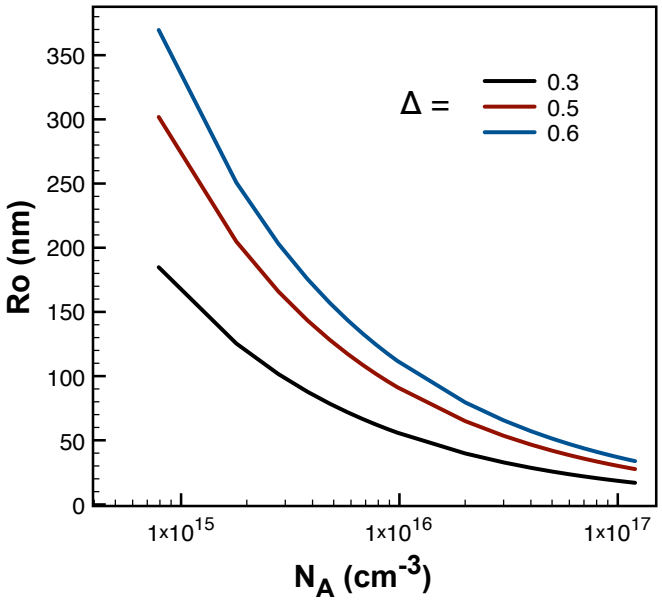

Figure 8.9. Pinch-off requirements for p-Si/Pt system for varying values of Δ

alytic effects. A better experimental approach would be to produce identical patterns on Si wafers of different doping densities. Increasing the doping density of the semiconductor decreases the depletion width, thus changing the criteria for pinch-off. Figure 8.9 shows the maximum value for R_0 calculated from Eq. 8.3 for a variety of values of Δ. By varying the doping density of Si from $\sim$1 x 10^{15} to 1 x 10^{17} cm^{-3}, it should be possible to fabricate samples with 100 nm particles across the pinch-off criteria threshold. If the pinch-off effect is playing a role, the HER performance of these devices will vary even though each device has identical catalyst loading.

Sentuarus was used to model the band bending for structures with 120 nm Pt patches for Si with the following p-type doping densities: 1 x 10^{15}, 1 x 10^{16}, 3 x 10^{16}, and 1 x 10^{17}. Figure 8.10 shows the full Sentaurus simulation for each doping density, as well as the energy behind the center of the Pt patch. For the highest doping density, the barrier height behind the Pt nearly disappears and the contact become ohmic. This can be seen in the simulated dark $J-V$ curves for these devices (Fig. 8.11), as the 1 x 10^{17} doped Si shows no rectifying behavior.

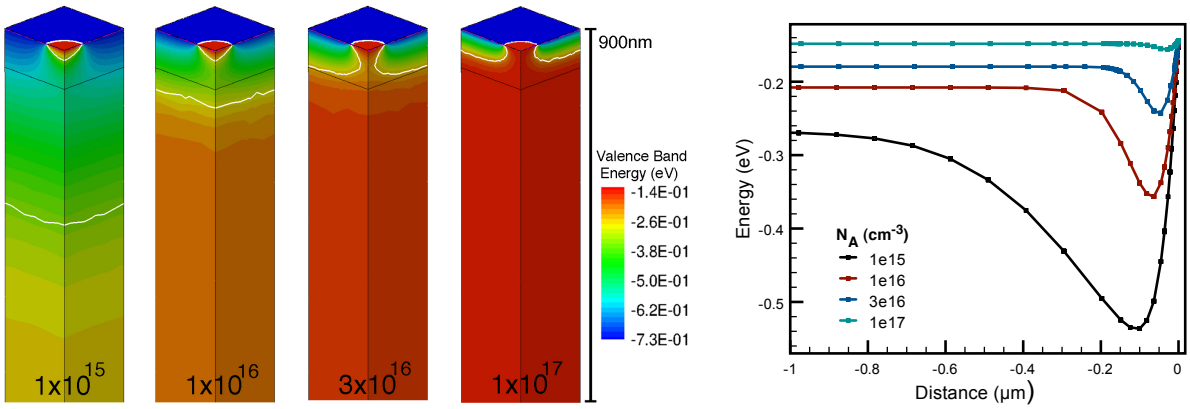

Figure 8.10. Left: Simulated valence band edge position for p-Si patterned with 1/4 of a Pt circle with the doping density of the Si ranging from 1 x 10^{15} to 1 x 10^{17} cm^{-3}. Right: Valence band energy vs. position behind the center of the metal patch

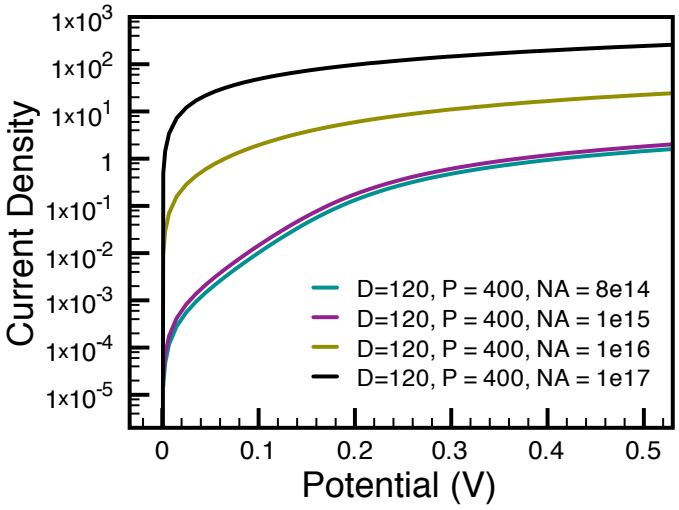

Figure 8.11. Simulated $J - V$ data for p-Si system of various doping patterned with square-packed 120 x 400 nm Pt patches

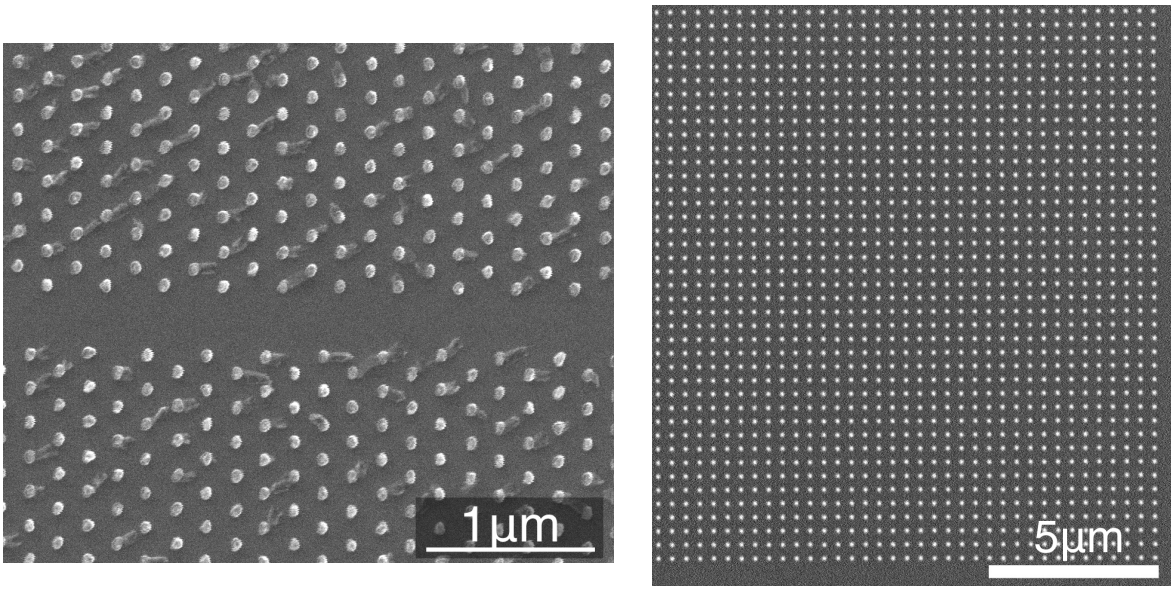

Figure 8.12. SEM images of EBPG nano-patterned metal dots on Si. Left: 60 nm x 200 nm, hexagonally packed Ni dots on Si. Right: 120 nm x 400 nm Pt dots on Si (Scale bar = 5 μm.)

8.5.1 Patterning the catalyst

To ensure accurate experimental results, a high level of control is needed over the geometry of the patterned catalyst. While nano-sphere lithography is useful for some applications, it cannot access all possible geometries and defects in the pattern occur regularly. To maintain a higher degree of control, a 100 kV Leica EBPG 5000+ electron-beam lithography system was used to write the desired pattern into an e-beam resist layer. The EBPG can write sub-100 nm features over large areas (5"), in relatively short periods of time, with writing speeds up to 50 MHz. This technology can eventually be used to create a master for nano-imprint lithography stamps similar to the micro-imprint stamping discussed in Chapter 7.

Even with this powerful tool, patterning areas large enough to make electrodes (2–4 mm^2) with features on the order of 100 nm is a time intensive process. Dosing tests and pattern optimizations were conducted to minimize the write time. Optimal write-time efficiency was achieved by designing the pattern as an array of hexagons using Layout Editor, and fracturing the pattern at 10 nm resolution with Layout Beamer to slit each hexagon into two trapezoids (minimizing the number of trapezoids increases writing efficiency).

Si substrates were coated with a bi-layer of PMMA photoresist (495k A4 and 950k A2), and patterned using the EBPG 5000+ tool with typical pattern resolution and a beam-step

size of 10 nm, an electron dose of 1100 μC cm^{-2} and a beam current of 25 nA. The EBPG tool has a sample stage with laser-interferometer positioning, allowing for devices to be written across multiple fields of view without measurable stitching errors, but to avoid the possibility of misalignment, each 500 μm mainfield was offset by 200 nm. The exposed resist was removed with 1:3 MIBK:IPA, leaving a pattern of holes in the resist. Samples were briefly dipped in buffered HF to remove any native oxide from the Si surface, and then metal was evaporated using an e-beam evaporator. Care was taken to ensure that the samples were positioned normal to the evaporation source, to minimize deposition on the sidewalls of the resist. Lift-off was performed in acetone. Figure 8.12 shows SEM images of EBPG patterned samples. The image on the left shows patterned 60 x 200 nm Ni dots $\sim$ 50 nm thick. The excess material on the pattern is due to excess Ni on the sidewalls of the photoresist during evaporation that could not be removed during lift-off. The image on the right shows a square packed array of 120 x 400 nm Pt dots ($\sim$10 nm thick).

8.6 Electrochemistry

Electrodes patterned with 120 x 400 nm square packed dots on p$^+$-Si and $N_A \sim 1$ x 10^{17} have been fabricated and tested electrochemically as HER photocathodes. For these patterns, alignment marks were not written onto the substrates, so isolating the patterned areas during electrode fabrication was a major challenge. The HER performance of these electrodes were tested in H_2-purged 0.5 M H_2SO_4 following the experimental procedure from Chapter 5. The HER performance data are shown in Fig. 8.13. For the degenerate electrodes, the onset of current required slightly more overpotential than a continuous Pt film. The photoactive p-Si showed no activity in the dark, but did show a small shift in photocurrent onset under illumination. While this result is far from conclusive, other p-Si electrodes patterned with larger Pt islands (green dashed line) did not show any photovoltage onset under the same illumination conditions. Future experiments will focus on using p-Si with lower dopant densities to confirm this effect. Due to EBPG tool availability, Si substrates with different doping densities have not yet been patterned, but work is currently underway.

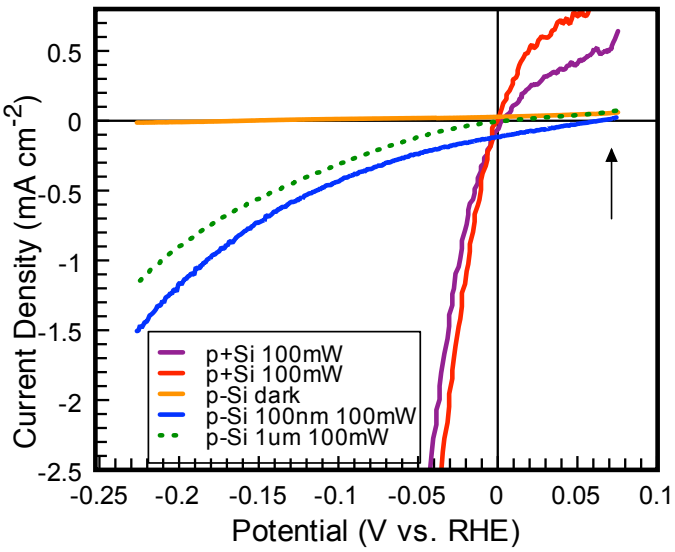

Figure 8.13. $J - E$ data for EBPG patterned Pt on p^+Si and p-Si electrodes

8.7 Future work

While this chapter provides much of the background simulation and process development work for investigation of pinch-off for the Pt/p-Si/HER system, equipment outages have limited the number of experimental samples that have been prepared. Once experimental nano-patterned samples have been fabricated, the $J - E$ performance of the patterned electrodes should be investigated in a high barrier height redox couple such as methyl viologen, as well as for the HER. Work is currently underway to fabricate nano-imprint stamps from EBPG-patterned masters to increase the throughput of fabrication for nano-patterned samples. This should enable investigation of different semiconductor and catalyst materials, as well as controlled introduction of thin barrier layers using ALD, which have been shown to improve performance and stability of photoelectrochemical systems.[128]

Future modeling work will focus on simulating the performance of these patterned devices under illumination. Initial work will focus on using simple Lambert-Beer absorption in the Si to determine how the V_{oc} values change with the effective barrier height of the junction. Eventually, the optical effects of the nano-patterned catalyst (which may introduce plasmonic resonances, significantly changing the absorption profile near the Si surface) can be coupled to the electrical simulation.

Chapter 9

Conclusion and outlook

9.1 Summary of work

The work presented in this thesis expands the existing body of knowledge on the development of Si MW arrays as absorber materials for solar energy conversion. The ability to grow a high quality semiconductor material from an inexpensive precursor ($SiCl_4$) using high-throughput processing techniques makes this technology a viable alternative to the current industry standard of bulk crystal growth, wafering, and polishing. While a great deal of previous work in the field focused on the use of VLS grown Si MW arrays for photovoltaic applications, we have demonstrated that these materials also have potential application for solar fuel generation. The potential low cost, high surface area, and flexibility of Si MW array devices provide a platform for future efforts to build a membrane-based solar fuel generating system.

In Chapter 3, we demonstrated that regenerative photoelectrochemistry, using the methyl viologen redox couple, can be used to make conformal, high barrier height contacts to Si MW arrays to characterize their energy conversion properties. We discussed the photoelectrochemical experimental setup, and provided examples of how $MV^{2+/+}$ electrochemistry was used to quantify the material quality of p-type Si MW arrays grown by the VLS process. This system can be used to understand how the energy conversion efficiency of Si MW arrays is affected by array geometry, doping density, p-n junction formation, and other processing steps. In Chapter 4, we expanded the use of the $MV^{2+/+}$ to investigate the pH-dependence of the energetics of Si photoelectrodes in aqueous environments. Even though the band edges of Si varied with pH due to changes in surface chemistry, the introduction of a p-n homojunction decoupled the energy conversion properties of the solid-state device from

that of the contacting electrolyte. The n^+p-Si devices also had improved photoconversion efficiencies compared to the p-Si/liquid contacts investigated previously.

Chapters 5 and 6 discussed the integration of HER catalysts onto Si MW arrays for solar-driven hydrogen production. By comparing different catalysts on both planar and high surface Si MW electrodes, we demonstrated that Ni–Mo is a promising alternative to Pt as an HER photocatalyst under mildly acidic conditions. However, when p-Si absorbers were directly coupled to HER catalysts, the photocathodes were only able to generate a tiny portion of the photovoltage needed for the overall water splitting reaction. The introduction of a n^+ emitter layer to create a solid-state homojunction allowed us to maintain the high photovoltages observed using regenerative photoelectrochemistry while also driving the HER photosynthetic reaction. We first demonstrated that Pt/n^+p-Si MW devices could drive the HER at 6% efficiency, and then developed fabrication techniques to drive the same reaction using earth-abundant Ni–Mo catalysts at $\sim$ 2% efficiency. Using a slower, earth-abundant catalyst presented several design challenges which were addressed by analyzing the catalyst morphology, p-n junction properties, wire geometry, and spectral response of the system.

Chapter 7 presented new fabrication techniques to lower the cost of manufacturing the wire arrays by using scalable technologies such as micro-imprint lithography and electrodeposition. We demonstrated that it was possible to grow high-fidelity VLS Si MW arrays using electrodeposited Cu and substrates patterned with imprint lithography. Using $MV^{2+/+}$ photoelectrochemistry, we confirmed that the material quality and energy conversion properties of these Si MW arrays was similar to those grown from evaporated high-purity Cu. These techniques will allow for high-throughput processing and enable the fabrication of larger diameter VLS-grown Si MW arrays.

Finally, Chapter 8 investigated the physics of catalyst/Si surface by using finite-element device physics simulations to understand the factors controlling the band energetics at Si electrodes patterned with metal nanoparticles. Future work will determine if the "pinch-off" effect can be exploited to create high-barrier height contacts for semiconductors patterned with low-barrier height metal catalysts. The use of a three-dimensional simulation allows the interactions between band-bending induced by adjacent particles to be examined over a wide range of geometries, which expands the capabilities of prior models that treated each particle separately. The model was compared to prior experimental work on the pinch-off effect using

samples of patterned Ni on n-Si that were characterized with regenerative electrochemistry, and then used to examine the energetics of the Pt/p-Si|HER system. We explored the effects of Pt catalyst loading, and found that it should be possible to achieve fast HER catalysis with loadings low enough to observe the pinch-off effect. Methods to pattern nanoscale patches of metal catalysts over large areas have been developed, and future work will examine how these nano-patterned samples will perform as HER photocathodes.

9.2 Future directions

The remarkable achievements made in the development of Si microwires for photovoltaic and photoelectrochemical energy conversion motivate continued research on the use of these materials in integrated energy conversion systems. Some active and promising areas of research are outlined below.

A great deal of effort has been devoted to "proof of concept" projects, to demonstrate the many advantages of Si MW-based energy conversion. However, now that the basic requirements for solar energy conversion have been confirmed, a detailed engineering approach is needed to systematically study and improve several of the variables in the growth and processing of Si MW array devices. While the optical absorption of Si MW arrays has been studied for a variety of wire patterns geometries,[66] a similar study is needed for a solar fuel generating system, that accounts for mass-transport within the wire array as well as the effects of bubble formation.

More work is also needed to characterize the quality and improve the consistency of the wires grown from electrodeposited Cu. There is a great deal of work to be done to compare wires from different VLS catalysts using the many techniques that have been developed for Si MW-based devices (nano-SIMS, single-wire measurements, LBIC measurements, p-n junction characterization, surface passivation). For large-diameter wires, it is particularly important to develop techniques to make electrical contact to single wires for dopant density characterization.

For Si MW array photocathodes for the HER, the major challenge is designing a way to deposit an earth-abundant catalyst in a way to balance the catalyst loading and overpotential losses with the light absorption by the catalyst that limits photocurrent generation (Chapter 6). Methods are currently being developed to put catalyst only at the base of the wires, which is very effective for a top-illuminated device. However, in a tandem-absorber

membrane-based device, the illumination direction will be reversed, and both theoretical and experimental work is needed to optimize the light absorption and catalyst activity for an integrated water-splitting system. Another challenge that needs to be addressed to realize free-standing Si MW arrays for flexible membrane-based solar-fuel or photovoltaic systems is the creation of flexible electrical contacts. Co-current work has shown that Ag nanowires and PEDOT:PSS can be used to make electrical contact to Si MW arrays, but systems need to be developed to improve the ease of manipulating and handling these membrane-based devices during processing.[65]

The model developed in Chapter 8 to investigate the pinch-off effect for semiconductor/catalyst systems has a wide variety of applications for understanding systems that semiconductor photo-absorbers with catalytic reactions. Beyond the completion of the experiment with the Pt/p-Si system, the model can be coupled to optical simulations and be used for different material systems.[125] By varying the catalyst material, semiconductor material, and catalyst geometry, a great deal can be learned about the driving forces for catalysis at semiconductor/liquid junctions. The ability to fabricate electrodes with features patterned on the 100 nm scale over very large areas using soft-lithography techniques will enable theoretical models to be matched to experiment. These patterned substrates can also be used to define the geometry of different surface functionalizations of Si, and potentially provide a template for the attachment of molecular catalysts.[129] Additionally, recent developments in the deposition of very thin passivating films using atomic layer deposition (ALD) suggest that it might be interesting to combine the passivating effects of these ALD films with controllably patterned catalysts to enhance stability and catalytic activity.[128]

The VLS Si MW project has demonstrated that it is possible to grow high quality, single-crystalline Si material that can be embedded in a flexible substrate from an inexpensive precursor material using relatively simple technology. These wire arrays have shown promising energy conversion properties for electrical energy conversion and as absorbers to drive the hydrogen evolution reaction. If the challenges associated with reproducibility, electrical contacting, and manufacturing scalability can be addressed, this method represents a potential approach to reduce the cost of photovoltaic and photoelectrochemical energy conversion systems.

Appendix A

Sentaurus model parameters

A.1 Si Parameters

The default model for Si was used to create the SDevice parameter file using Boltzmann statistics. The basic properties of Si are listed in the table below.

Table A.1. Si parameters used for Sentaurus model

Parameter	Value
ϵ	11.7
E_G	1.124 eV
χ	4.0727 eV
N_v	3.1e19 cm^{-3}
N_c	2.9e19 cm^{-3}
$\tau_{SRH,e}$	1e-5 s
$\tau_{SRH,h}$	3e-6 s
v_p, v_n	1.0e6 cm s^{-1}

In addition, mobility was modeled using a dopant-dependent-based model based on As and B as the dopant sources. The back contact was defined as an ideal/ohmic contact.

A.2 Schottky contact definitions

For the liquid/metal contacts, Schottky contacts were defined based on input barrier heights and thermionic emission velocities (i.e., SRV).[118] Sentaurus uses the following boundary conditions to define the behavior at a Schottky contact:

$$\phi = \phi_F - \phi_B + \frac{kT}{q} ln\left(\frac{N_C}{n_{i,eff}}\right) \tag{A.1a}$$

$$\vec{J_n} \cdot \hat{n} = q v_n (n - n_0^B) \tag{A.1b}$$

$$\vec{J_p} \cdot \hat{n} = q v_p (p - p_0^B) \tag{A.1c}$$

$$n_0^B = N_C exp\left(\frac{-q\Phi_B}{kT}\right) \tag{A.1d}$$

$$p_0^B = N_V exp\left(\frac{q\Phi_B - E_{g,eff}}{kT}\right) \tag{A.1e}$$

where ϕ_F is the Fermi potential at the contact that is equal to an applied voltage ($V_{applied}$) and Φ_B is the difference between the contact work-function and the electron affinity of the semiconductor. $\vec{J_n} \cdot \hat{n}$ and $\vec{J_p} \cdot \hat{n}$ are the components of the electron and hole current densities normal to the surface, and v_n/v_p are the thermionic emission velocities. n_O^B and p_O^B are the equilibrium carrier densities calculated from equations A.1d and A.1e.[118]

A.3 Values used in simulations

Table A.2. Input parameters for the pinch-off model

Variable	Ni/n-Si	Pt/p-Si
Φ_L (eV)	0.84	0.39
Φ_M (eV)	0.62, 0.64	0.88, 0.98, 1.15
N_{DorA} (cm^{-3})	4e18	4e18, 1e15, 1e16, 1e17
τ (s)	3e-6	3e-6
SRV_L (cm/s)	1e6, 1e4	1e6
SRV_M (cm/s)	1e6, 1e4	1e6

Figure A.1. Sentaurus Device command file for 3D simulation of a patterned Schottky contact

```
# Pinch-off p-type
#setdep @nodel-1:all@

*******************************************************************************************************
* FILE
*******************************************************************************************************
File
{       Grid                    = "n@nodel-1@_msh_pof.tdr"
        Parameters              = "@parameter@"
        plot                    = "@tdrdat@"
        current                         = "@plot@"
      # OpticalGenerationInput = "optgen_des_R@R@_Base@Base@.tdr"
}

*******************************************************************************************************
* ELECTRODES
*******************************************************************************************************
Electrode
{
  { name="metal_cnt" Voltage=0.0 Schottky Barrier = @PhiM@ eRecVelocity = @M_SRV@ hRecVelocity = @M_SRV@ }
  { name="liquid_cnt" voltage=0.0 Schottky Barrier = 0.39
 eRecVelocity = @L_SRV@ hRecVelocity = @L_SRV@}
  { name="base_cnt" voltage=0.0 }
}
*******************************************************************************************************
* PLOT
*******************************************************************************************************
Plot
{
        eCurrent/Vector hCurrent/Vector current/vector
      ElectricField/Vector eDriftVelocity/Vector hDriftVelocity/Vector
        SpaceCharge eDensity hDensity
        Potential ConductionBandEnergy ValenceBandEnergy
        SRH Auger TotalRecombination SurfaceRecombination eGapStatesRecombination hGapStatesRecombination
      DopingConcentration OpticalGeneration
      CurrentPotential
}
*******************************************************************************************************
* PHYSICS
*******************************************************************************************************
Physics
{
  Mobility(DopingDep)
  Recombination(SRH Auger)
  * set the area of the device, this has to do with how sentaurus handles units inherently in 3d, this makes normalizations correct
 * Area=@<1e8/(2*@R@)>@
  }
*******************************************************************************************************
* MATH
*******************************************************************************************************
Math{
   Method = ParDiSo
   Number_of_Threads = 8
   Extrapolate
   Derivatives
   AvalDerivatives
   RelErrControl
   Digits=6
   RhsMin=1E-15
   ExtendedPrecision
   Iterations=300
   Notdamped=300
   ExitOnFailure
   StackSize=4000000

  * This terminates the simulation once the current becomes negative ( i.e. after VOC is reached )
  * Note this would have to be changed for p-n vs n-p junctions....
  * BreakCriteria
 * { Current (Contact = "emitter_cnt" maxval = 1E-20) }
}
*******************************************************************************************************
* SOLVE
*******************************************************************************************************
Solve
{ *--First solve the V=0 case (short cicuit condition)
  Coupled  { poisson }
  Coupled  { poisson electron }
  Coupled  { poisson electron hole }

*  *-- Dark I-V use quasistationary to ramp the emitter current
Plot( FilePrefix = "n@node@_ISC_" )
NewCurrentPrefix="DarkIV_"

Quasistationary( InitialStep=0.001 MinStep=1E-4 MaxStep=0.01 Increment=2
Goal { Name=base_cnt Voltage=1 })
{ Coupled  { poisson electron hole }   }
}
```

Bibliography

[1] N. S. Lewis and D. G. Nocera. Powering the planet: Chemical challenges in solar energy utilization. *Proceedings of the National Academy of Sciences of the United States of America*, 104(50):20142–20142, 2007.

[2] U.S. Energy Information Administration. Annual Energy Review. U.S. Department of Energy, Sept 27, 2012.

[3] N. S. Lewis. Toward cost-effective solar energy use. *Science*, 315(5813):798–801, 2007.

[4] S. A. Kalogirou. Solar thermal collectors and applications. *Progress in Energy and Combustion Science*, 30(3):231–295, 2004.

[5] M. Gratzel. Photoelectrochemical cells. *Nature*, 414(6861):338–344, 2001.

[6] Allen J. Bard and Marye Anne Fox. Artificial photosynthesis: Solar splitting of water to hydrogen and oxygen. *Accounts of Chemical Research*, 28(3):141–145, 1995.

[7] J. R. Bolton, S. J. Strickler, and J. S. Connolly. Limiting and realizable efficiencies of solar photolysis of water. *Nature*, 316(6028):495–500, 1985.

[8] Michael G. Walter, Emily L. Warren, James R. McKone, Shannon W. Boettcher, Qixi Mi, Elizabeth A. Santori, and Nathan S. Lewis. Solar water splitting cells. *Chemical Reviews*, 110(11):6446–6473, 2010.

[9] H. Gerischer. On the stability of semiconductor electrodes against photodecomposition. *J. Electroanal. Chemistry*, 82:133–143, 1977.

[10] Independent Review. Current (2009) state-of-the-art hydrogen production cost estimate using water electrolysis. National Renewable Energy Lab, 2009.

[11] Solarbuzz. Solar module pricing—retail price summary. March, 2012, (http://www.solarbuzz.com/facts-and-figures/retail-price-environment/module-prices).

[12] Zhebo Chen, Thomas F. Jaramillo, Todd G. Deutsch, Alan Kleiman-Shwarsctein, Arnold J. Forman, Nicolas Gaillard, Roxanne Garland, Kazuhiro Takanabe, Clemens Heske, Mahendra Sunkara, Eric W. McFarland, Kazunari Domen, Eric L. Miller, John A. Turner, and Huyen N. Dinh. Accelerating materials development for photoelectrochemical hydrogen production: Standards for methods, definitions, and reporting protocols. *Journal of Materials Research*, 25(1, SI):3–16, Jan 2010.

[13] Adam Heller. Hydrogen-evolving solar cells. *Science*, 223(4641):1141–1148, 1984.

[14] O. K. Varghese and C. A. Grimes. Appropriate strategies for determining the photoconversion efficiency of water photo electrolysis cells: A review with examples using titania nanotube array photoanodes. *Sol. Energy Mater. Sol. Cells*, 92(4):374–384, 2008.

[15] Michael F. Weber and Michael J. Dignam. Efficiency of splitting water with semiconducting photoelectrodes. *J. Electrochem. Soc.*, 131(6):1258–1265, 1984.

[16] Eric L. Miller, Bjorn Marsen, Daniela Paluselli, and Richard Rocheleau. Optimization of hybrid photoelectrodes for solar water-splitting. *Electrochemical and Solid-State Letters*, 8(5):A247–A249, 2005.

[17] B.E. Conway and M. Salomon. Electrochemical reaction orders: Applications to the hydrogen- and oxygen-evolution reactions. *Electrochimica Acta*, 9(12):1599–1615, 1964.

[18] E. Aharon-Shalom and A. Heller. Efficient p-InP(Rh-H alloy) and p-InP(Re-H alloy) hydrogen evolving photocathodes. *Journal of the Electrochemical Society*, 129(12): 2865–2866, 1982.

[19] O. Khaselev and J. A. Turner. Electrochemical stability of p-$GaInP_2$ in aqueous electrolytes toward photoelectrochemical water splitting. *Journal of the Electrochemical Society*, 145(10):3335–3339, 1998.

[20] Y. Nakato, H. Yano, S. Nishiura, T. Ueda, and H. Tsubomura. Hydrogen photoevolution at p-type silicon electrodes coated with discontinuous metal layers. *Journal of Electroanalytical Chemistry*, 228(1–2):97–108, 1987.

[21] R. N. Dominey, N. S. Lewis, J. A. Bruce, D. C. Bookbinder, and M. S. Wrighton. Improvement of photo-electrochemical hydrogen generation by surface modification of p-type silicon semiconductor photo-cathodes. *Journal of the American Chemical Society*, 104(2):467–482, 1982.

[22] D. C. Bookbinder, J. A. Bruce, R. N. Dominey, N. S. Lewis, and M. S. Wrighton. Synthesis and characterization of a photosensitive interface for hydrogen generation - chemically modified p-type semiconducting silicon photo-cathodes. *Proceedings of the National Academy of Sciences of the United States of America-Physical Sciences*, 77(11):6280–6284, 1980.

[23] A. B. Bocarsly, D. C. Bookbinder, R. N. Dominey, N. S. Lewis, and M. S. Wrighton. Photo-reduction at illuminated p-type semiconducting silicon photoelectrodes—evidence for Fermi level pinning. *Journal of the American Chemical Society*, 102 (11):3683–3688, 1980.

[24] S. Trasatti. Electrocatalysis of hydrogen evolution: Progress in cathode activation. *Advances in Electrochemical Science and Engineering*, 2:1–85, 1992.

[25] S. Trasatti. Work function, electronegativity, and electrochemical behavior of metals .3. electrolytic hydrogen evolution in acid solutions. *J. Electroanal. Chem.*, 39(1):163, 1972.

[26] D. E. Brown, M. N. Mahmood, A. K. Turner, S. M. Hall, and P. O. Fogarty. Low overvoltage electrocatalysts for hydrogen evolving electrodes. *International Journal of Hydrogen Energy*, 7(5):405–410, 1982.

[27] R. M. Swanson. A vision for crystalline silicon photovoltaics. *Progress in Photovoltaics: Research and Applications*, 14(5):443–453, 2006.

[28] B. M. Kayes, H. A. Atwater, and N. S. Lewis. Comparison of the device physics principles of planar and radial p-n junction nanorod solar cells. *Journal of Applied Physics*, 97(11):114302, 2005.

[29] Morgan C. Putnam, Daniel B. Turner-Evans, Michael D. Kelzenberg, Shannon W. Boettcher, Nathan S. Lewis, and Harry A. Atwater. 10 μm minority-carrier diffusion lengths in Si wires synthesized by Cu-catalyzed vapor-liquid-solid growth. *Applied Physics Letters*, 95(16):163116–3, 2009.

[30] Michael D. Kelzenberg, Daniel B. Turner-Evans, Morgan C. Putnam, Shannon W. Boettcher, Ryan M. Briggs, Jae Yeon Baek, Nathan S. Lewis, and Harry A. Atwater. High-performance Si microwire photovoltaics. *Energy & Environmental Science*, 2011.

[31] Brendan M. Kayes. *Radial pn Junction Wire Array Solar Cells*. PhD thesis, California Institute of Technology, 2009.

[32] M. D. Kelzenberg. *Silicon Microwire Photovoltaics*. PhD thesis, California Institute of Technology, 2010.

[33] Brendan M. Kayes, Michael A. Filler, Morgan C. Putnam, Michael D. Kelzenberg, Nathan S. Lewis, and Harry A. Atwater. Growth of vertically aligned si wire arrays over large areas (> 1 cm^2) with Au and Cu catalysts. *Applied Physics Letters*, 91(10): 103110, 2007.

[34] Morgan C. Putnam. *Si Microwire-Array Solar Cells*. PhD thesis, California Institute of Technology, 2010.

[35] A. C. Tamboli, C. T Chen, E. L. Warren, D. B Turner-Evans, M. D. Kelzenberg, H. A. Atwater, and N. S. Lewis. Wafer-scale growth of silicon microwire arrays for photovoltaics. *Journal of Photovoltaics*, 2(3), 2012.

[36] R. S. Wagner and W. C. Ellis. Vapor-liquid-solid mechanism of single crystal growth. *Applied Physics Letters*, 4(5):89–90, 1964.

[37] Volker Schmidt, Joerg V. Wittemann, Stephan Senz, and Ulrich Gsele. Silicon nanowires: A review on aspects of their growth and their electrical properties. *Advanced Materials*, 21(25-26):2681–2702, 2009.

[38] V. Schmidt, J. V. Wittemann, and U. G$'$osele. Growth, thermodynamics, and electrical properties of silicon nanowires. *Chemical Reviews*, 110(1):361–388, 2010.

[39] A. A. Istratov, T. Buonassisi, R. J. McDonald, A. R. Smith, R. Schindler, J. A. Rand, J. P. Kalejs, and E. R. Weber. Metal content of multicrystalline silicon for solar cells and its impact on minority carrier diffusion length. *Journal of Applied Physics*, 94 (10):6552–6559, 11 2003.

[40] Andrei A. Istratov and Eicke R. Weber. Physics of copper in silicon. *Journal of the Electrochemical Society*, 149(1):G21–G30, 2002.

[41] S. W. Boettcher, J. M. Spurgeon, M. C. Putnam, E. L. Warren, D. B. Turner-Evans, M. D. Kelzenberg, J. R. Maiolo, H. A. Atwater, and N. S. Lewis. Energy-conversion properties of vapor-liquid-solid-grown silicon wire-array photocathodes. *Science*, 327 (5962):185–187, 2010.

[42] Morgan C. Putnam, Michael A. Filler, Brendan M. Kayes, Michael D. Kelzenberg, Yunbin Guan, Nathan S. Lewis, John M. Eiler, and Harry A. Atwater. Secondary ion mass spectrometry of vaporLiquidSolid grown, Au-catalyzed, Si wires. *Nano Letters*, 8(10):3109–3113, 2008.

[43] K. E. Plass, M. A. Filler, J. M. Spurgeon, B. M. Kayes, S. Maldonado, B. S. Brunschwig, H. A. Atwater, and N. S. Lewis. Flexible polymer-embedded si wire arrays. *Advanced Materials*, 21(3):325–328, 2009.

[44] J. M. Spurgeon, K. E. Plass, B. M. Kayes, B. S. Brunschwig, H. A. Atwater, and N. S. Lewis. Repeated epitaxial growth and transfer of arrays of patterned, vertically aligned, crystalline Si wires from a single Si(111) substrate. *Applied Physics Letters*, 93(3), 2008.

[45] S. Takayama, E. Ostuni, X. Qian, J. C. McDonald, X. Jiang, P. LeDuc, M. H. Wu, D. E. Ingber, and G. M. Whitesides. Topographical micropatterning of poly(dimethylsiloxane) using laminar flows of liquids in capillaries. *Advanced Materials*, 13(8):570–574, 2001.

[46] Morgan C. Putnam, Shannon W. Boettcher, Michael D. Kelzenberg, Daniel B. Turner-Evans, Joshua M. Spurgeon, Emily L. Warren, Ryan M. Briggs, Nathan S. Lewis, and Harry A. Atwater. Si microwire-array solar cells. *Energy & Environmental Science*, 3:1037–1041, 2010.

[47] Chito Kendrick, Heayong Yoon, Yu Yuwen, Greg Barber, Haoting Shen, Thomas Mallouk, Elizabeth Dickey, Theresa Mayer, and Joan Redwing. Radial junction silicon wire array solar cells fabricated by gold-catalyzed vapor-liquid-solid growth. *Applied Physics Letters*, 97(14):143108, 2010.

[48] N. S. Lewis. A quantitative investigation of the open-circuit photovoltage of the semiconductor liquid interface. *Journal of the Electrochemical Society*, 131(11):2496–2503, 1984.

[49] A. J. Bard and L. R. Faulkner. *Electrochemical Methods: Fundamentals and Applications*. John Wiley & Sons, Inc., Hoboken, NJ, 2nd edition, 2001.

[50] Ming X. Tan, Paul E Laibinis, Sonbinh T. Nguyen, Janet M. Kesselman, Colby E. Stanton, and Nathan S. Lewis. Principles and applications of semiconductor photoelectrochemistry. *Progress in Inorganic Chemistry*, pages 21–144, 1994.

[51] M. L. Rosenbluth and N. S. Lewis. Kinetic studies of carrier transport and recombination at the n-Silicon/Methanol interface. *Journal of the American Chemical Society*, 108(16):4689–4695, 1986.

[52] Elizabeth A. Santori, James R. Maiolo, Matthew J. Bierman, Nicholas C. Strandwitz, Michael D. Kelzenberg, Bruce S. Brunschwig, Harry A. Atwater, and Nathan S. Lewis. Photoanodic behavior of vapor-liquid-solid-grown, lightly doped, crystalline Si microwire arrays. *Energy & Environmental Science*, 5:6867–6871, 2012.

[53] A. Heller, B. Miller, H. J. Lewerenz, and K. J. Bachmann. An efficient photo-cathode for semiconductor liquid junction cells - 9.4-percent solar conversion efficiency with p-InP-VCl_3-VCl_2-HCl-C. *Journal of the American Chemical Society*, 102(21):6555–6556, 1980.

[54] Bruce J. Tufts, Louis G. Casagrande, Nathan S. Lewis, and Frank J. Grunthaner. Correlations between the interfacial chemistry and current-voltage behavior of n-GaAs/liquid junctions. *Applied Physics Letters*, 57(12):1242–1244, 1990.

[55] G. Hodes, J. Manassen, and D. Cahen. Photoelectrochemical energy-conversion and storage using polycrystalline chalcogenide electrodes. *Nature*, 261(5559):403–404, 1976.

[56] R. L. Grimm, M. J. Bierman, L. E. O'Leary, N. C. Strandwitz, B. S. Brunschwig, and N. S. Lewis. Comparison of the photoelectrochemical behavior of H-terminated and methyl-terminated Si(111) surfaces in contact with a series of one-electron, outer-sphere redox couples in CH_3CN. *Journal of Physical Chemistry C*, 116(44):23569–23576, 2012.

[57] C. L. Bird and A. T. Kuhn. Electrochemistry of the viologens. *Chem. Soc. Rev.*, 10: 49–82, 1981.

[58] Erik Johansson, Shannon W. Boettcher, Leslie E. O'Leary, Andrey Polatayev, and N. S. Lewis. Control of the ph-dependence of the band edges of si(111) surfaces using mixed methyl/allyl monolayers. *Journal of Physical Chemistry C*, 2011.

[59] T. W. Hamann and N. S. Lewis. Control of the stability, electron-transfer kinetics, and pH-dependent energetics of Si/H_2O interfaces through methyl termination of Si(111) surfaces. *Journal of Physical Chemistry B*, 110(45):22291–22294, 2006.

[60] E. S. Kooij, R. W. Despo, F. P. J. Mulders, and J. J. Kelly. Electrochemistry of porous and crystalline silicon electrodes in methylviologen solutions. *Journal of Electroanalytical Chemistry*, 406(1-2):139–146, 1996.

[61] W. John Albery and C. Paul Wilde. The photoelectrochemical kinetics of the reduction of methyl viologen on p-type GaP. *Journal of the Electrochemical Society*, 134 (9):2221–2226, 1987.

[62] Michael Heyrovsky. The electroreduction of methyl viologen. *J. Chem. Soc., Chem. Commun.*, pages 1856–1857, 1987.

[63] A. M. Fajardo and N. S. Lewis. Free-energy dependence of electron-transfer rate constants at Si/liquid interfaces. *Journal of Physical Chemistry B*, 101(51):11136–11151, 1997.

[64] E. L. Warren, D. B Turner-Evans, R. L. Grimm, H. A. Atwater, and N. S. Lewis. Photoelectrochemical characterization of si microwire array solar cells. *Proceedings of the 38th IEEE Photovoltaics Specialist Conference*, 2012.

[65] D. B Turner-Evans and H. A. Atwater. Flexible silicon microwire photovoltaics. *In Prep.*, 2012.

[66] M. D. Kelzenberg, S. W. Boettcher, J. A. Petykiewicz, D. B. Turner-Evans, M. C. Putnam, E. L. Warren, J. M. Spurgeon, R. M. Briggs, N. S. Lewis, and H. A. Atwater. Enhanced absorption and carrier collection in Si wire arrays for photovoltaic applications. *Nature Materials*, 9(3):239–244, 2010.

[67] J. R. Maiolo, B. M. Kayes, M. A. Filler, M. C. Putnam, M. D. Kelzenberg, H. A. Atwater, and N. S. Lewis. High aspect ratio silicon wire array photoelectrochemical cells. *Journal of the American Chemical Society*, 129:12346–12347, 2007.

[68] M. J. Madou, B. H. Loo, K. W. Frese, and S. Roy Morrison. Bulk and surface characterization of the silicon electrode. *Surface Science*, 108(1):135–152, 1981.

[69] Ralf Hunger, Rainer Fritsche, Bengt Jaeckel, Lauren J. Webb, Wolfram Jaegermann, and Nathan S. Lewis. High-resolution photoemission studies of the interfacial reactivity and interfacial energetics of Au and Cu schottky barriers on methyl-terminated Si(111) surfaces. *Surface Science*, 601(14):2896–2907, 2007.

[70] Yoshihiro Nakato, Yoshihiro Egi, Masahiro Hiramoto, and Hiroshi Tsubomura. Hydrogen evolution and iodine reduction on an illuminated n-p junction silicon electrode and its application to efficient solar photoelectrolysis of hydrogen iodide. *The Journal of Physical Chemistry*, 88(19):4218–4222, 1984.

[71] E. L. Johnson. The TI solar energy system development. *Electron Devices Meeting, 1981 International*, 27:2–5, 1981.

[72] M. D. Kelzenberg, D. B. Turner-Evans, B. M. Kayes, M. A. Filler, M. C. Putnam, N. S. Lewis, and H. A. Atwater. Photovoltaic measurements in single-nanowire silicon solar cells. *Nano Letters*, 8(2):710–714, 2008.

[73] A. L. Fahrenbruch and R. H. Bube. *Fundamentals of Solar Cells*. Academic Press, 1983.

[74] Thomas W. Hamann, Florian Gstrein, Bruce S. Brunschwig, and Nathan S. Lewis. Measurement of the dependence of interfacial charge-transfer rate constants on the reorganization energy of redox species at n-ZnO/H_2O interfaces. *Journal of the American Chemical Society*, 127(40):13949–13954, 2005.

[75] Thomas W. Hamann, Florian Gstrein, Bruce S. Brunschwig, and Nathan S. Lewis. Measurement of the driving force dependence of interfacial charge-transfer rate constants in response to ph changes at n-ZnO/H_2O interfaces. *Chemical Physics*, 326(1): 15–23, 2006.

[76] Simon M. Sze and Kwok K. Ng. *Physics of Semiconductor Devices*. Wiley-Interscience, 2006.

[77] O. Khaselev and J. A. Turner. A monolithic photovoltaic-photoelectrochemical device for hydrogen production via water splitting. *Science*, 280(5362):425–427, 1998.

[78] I. Lombardi, S. Marchionna, G. Zangari, and S. Pizzini. Effect of Pt particle size and distribution on photoelectrochemical hydrogen evolution by p-Si photocathodes. *Langmuir*, 23(24):12413–12420, 2007.

[79] James R. McKone, Emily L. Warren, Matthew J. Bierman, Shannon W. Boettcher, Bruce S. Brunschwig, Nathan S. Lewis, and Harry B. Gray. Evaluation of Pt, Ni, and Ni–Mo electrocatalysts for hydrogen evolution on crystalline Si electrodes. *Energy & Environmental Science*, 4:3573–3583, 2011.

[80] Yidong Hou, Billie L. Abrams, Peter C. K. Vesborg, Mårten E. Björketun, Konrad Herbst, Lone Bech, Alessandro M. Setti, Christian D. Damsgaard, Thomas Pedersen, Ole Hansen, Jan Rossmeisl, Søren Dahl, Jens K. Nørskov, and Ib Chorkendorff. Bioinspired molecular co-catalysts bonded to a silicon photocathode for solar hydrogen evolution. *Nat. Mater.*, 10(6):434–438, 2011.

[81] A. Heller and R. G. Vadimsky. Efficient solar to chemical conversion—12-percent efficient photoassisted electrolysis in the [p-type Inp(Ru)] - HCl-KCl-Pt(Rh) cell. *Physical Review Letters*, 46(17):1153–1156, 1981.

[82] Sophia Haussener, Chengxiang Xiang, Joshua M. Spurgeon, Shane Ardo, Nathan S. Lewis, and Adam Z. Weber. Modeling, simulation, and design criteria for photoelectrochemical water-splitting systems. *Energy Environ. Sci.*, 5:9922–9935, 2012.

[83] C. Carraro, R. Maboudian, and L. Magagnin. Metallization and nanostructuring of semiconductor surfaces by galvanic displacement processes. *Surface Science Reports*, 62(12):499–525, 2007.

[84] S. Yae, N. Nasu, K. Matsumoto, T. Hagihara, N. Fukumuro, and H. Matsuda. Nucleation behavior in electroless displacement deposition of metals on silicon from hydrofluoric acid solutions. *Electrochimica Acta*, 53(1):35–41, 2007.

[85] X. Zhang, Z. Chen, and K. N. Tu. Immersion nickel deposition on blank silicon in aqueous solution containing ammonium fluoride. *Thin Solid Films*, 515(11):4696–4701, 2007.

[86] Shannon W. Boettcher, Emily L. Warren, Morgan C. Putnam, Elizabeth A. Santori, Daniel Turner-Evans, Michael D. Kelzenberg, Michael G. Walter, James R. McKone, Bruce S. Brunschwig, Harry A. Atwater, and Nathan S. Lewis. Photoelectrochemical hydrogen evolution using Si microwire arrays. *Journal of the American Chemical Society*, 133(5):1216–1219, 2011.

[87] J.S Kilby, J.W. Lanthrop, and W.A. Porter. U.S. patent 4021323, 1977, U.S. patent 4100051, 1978, U.S. patent 4136436, 1979. Texas Instruments, 1979.

[88] R. E. Rocheleau, E. L. Miller, and A. Misra. High-efficiency photoelectrochemical hydrogen production using multijunction amorphous silicon photoelectrodes. *Energy and Fuels*, 12(1):3–10, 1998.

[89] Steven Y. Reece, Jonathan A. Hamel, Kimberly Sung, Thomas D. Jarvi, Arthur J. Esswein, Joep J. H. Pijpers, and Daniel G. Nocera. Wireless solar water splitting using silicon-based semiconductors and earth-abundant catalysts. *Science*, 334(6056):645–648, 2011.

[90] Zhebo Chen, Dustin Cummins, Benjamin N. Reinecke, Ezra Clark, Mahendra K. Sunkara, and Thomas F. Jaramillo. Core–shell MoO_3–MoS_2 nanowires for hydrogen evolution: A functional design for electrocatalytic materials. *Nano Letters*, 11(10): 4168–4175, 2011.

[91] K. Sun, K. Madsen, P. Andersen, W. N. Bao, Z. L. Sun, and D. L. Wang. Metal on metal oxide nanowire Co-catalyzed Si photocathode for solar water splitting. *Nanotechnology*, 23(19), 2012.

[92] Emily L. Warren, James R. McKone, Harry A. Atwater, Harry B. Gray, and Nathan S. Lewis. Hydrogen-evolution characteristics of ni-mo-coated, radial junction, n^+p-silicon microwire array photocathodes. *Energy Environ. Sci.*, 5:9653–9661, 2012.

[93] Joshua M. Spurgeon, Michael G. Walter, Junfeng Zhou, Paul A. Kohl, and Nathan S. Lewis. Electrical conductivity, ionic conductivity, optical absorption, and gas separation properties of ionically conductive polymer membranes embedded with Si microwire arrays. *Energy & Environmental Science*, 4(5):1772–1780, 2011.

[94] Joshua M. Spurgeon, Shannon W. Boettcher, Michael D. Kelzenberg, Bruce S. Brunschwig, Harry A. Atwater, and Nathan S. Lewis. Flexible, polymer-supported, Si wire array photoelectrodes. *Advanced Materials*, 22:3277–3281, 2010.

[95] S. L. McFarlane, B. A. Day, K. McEleney, M. S. Freund, and N. S. Lewis. Designing electronic-ionic conducting membranes for artificial photosynthesis. *Energy & Environmental Science*, 4(5):1700–1703, 2011.

[96] Iman Yahyaie, Kevin McEleney, Michael Walter, Derek R. Oliver, Douglas J. Thomson, Michael S. Freund, and Nathan S. Lewis. Electrical characterization of Si microwires and of Si microwire/conducting polymer composite junctions. *J. Phys. Chem. Lett.*, 2(6):675–680, 2011.

[97] Emily L. Warren, Shannon W. Boettcher, Michael G. Walter, Harry A. Atwater, and Nathan S. Lewis. ph-independent, 520 mV open-circuit voltages of Si/methyl viologen$^{2+/+}$ contacts through use of radial n^+p-Si junction microwire array photoelectrodes. *The Journal of Physical Chemistry C*, 115(2):594–598, 2010.

[98] Sigmund Schuldiner. Hydrogen overvoltage on bright platinum. *Journal of the Electrochemical Society*, 101(8):426–432, 1954.

[99] D. E. Brown, M. N. Mahmood, M. C. M. Man, and A. K. Turner. Preparation and characterization of low overvoltage transition metal alloy electrocatalysts for hydrogen evolution in alkaline solutions. *Electrochimica Acta*, 29(11):1551–1556, 1984.

[100] J Nelson. *The Physics of Solar Cells*. Imperial College Press, London, 2003.

[101] Bruno Ceccaroli and Otto Lohne. *Solar Grade Silicon Feedstock*, chapter 5, pages 169–217. John Wiley & Sons, Ltd, 2011.

[102] M. D. Kelzenberg, D. B. Turner-Evans, M. C. Putnam, Kayes B. M., M. A. Filler, N. S. Lewis, and H. A. Atwater. Single-nanowire si solar cells. In *Photovoltaic Specialists Conference (PVSC), 2008 33th IEEE*, 2008.

[103] Younan Xia and George M. Whitesides. Soft lithography. *Angewandte Chemie International Edition*, 37(5):550–575, 1998. ISSN 1521-3773.

[104] Christopher J. Campbell, Stoyan K. Smoukov, Kyle J. M. Bishop, and Bartosz A. Grzybowski. Reactive surface micropatterning by wet stamping. *Langmuir*, 21(7): 2637–2640, 2005.

[105] S.K. Smoukov, K.J.M. Bishop, R. Klajn, C.J. Campbell, and B.A. Grzybowski. Cutting into solids with micropatterned gels. *Advanced Materials*, 17(11):1361–1365, 2005.

[106] Jessie Ku. Silicon microwire array production with microcontact printing and electrodeposition of growth catalyst. Honors thesis, California Institute of Technology, 2011.

[107] Vivian E. Ferry, Marc A. Verschuuren, Hongbo B. T. Li, Ruud E. I. Schropp, Harry A. Atwater, and Albert Polman. Improved red-response in thin film a-Si:H solar cells with soft-imprinted plasmonic back reflectors. *Applied Physics Letters*, 95(18), NOV 2 2009. ISSN 0003-6951.

[108] Teri W. Odom, J. Christopher Love, Daniel B. Wolfe, Kateri E. Paul, and George M. Whitesides. Improved pattern transfer in soft lithography using composite stamps. *Langmuir*, 18(13):5314–5320, 2002.

[109] M. A. Verschuuren. *Substrate conformal imprint lithography for nanophotonics*. PhD thesis, Utrecht University, 2010.

[110] T. P. Moffat, J. E. Bonevich, W. H. Huber, A. Stanishevsky, D. R. Kelly, G. R. Stafford, and D. Josell. Superconformal electrodeposition of copper in 500-90 nm features. *Journal of the Electrochemical Society*, 147(12):4524–4535, 2000.

[111] J. M. Spurgeon. *Wire Array Solar Cells: Fabrication and Photoelectrochemical Studies*. PhD thesis, California Institute of Technology, 2010.

[112] Yi Cui, Lincoln J. Lauhon, Mark S. Gudiksen, Jianfang Wang, and Charles M. Lieber. Diameter-controlled synthesis of single-crystal silicon nanowires. *Applied Physics Letters*, 78(15):2214–2216, 2001.

[113] Sarah M. Eichfeld, Haoting Shen, Chad M. Eichfeld, Suzanne E. Mohney, Elizabeth C. Dickey, and Joan M. Redwing. Gas phase equilibrium limitations on the vapor–liquid–solid growth of epitaxial silicon nanowires using sicl4. *Journal of Materials Research*, 26:2207–2214, 2011.

[114] V. A. Nebol'sin and A. A. Shchetinin. Role of surface energy in the vapor-liquid-solid growth of silicon. *Inorganic Materials*, 39(9):899–903, 2003.

[115] R. C. Rossi. *The Electrical Properties of Nanoscale Parallel Semiconductor Interfaces*. PhD thesis, California Institute of Technology, 2002.

[116] R. T. Tung. Electron-transport at metal-semiconductor interfaces - general-theory. *Physical Review B*, 45(23):13509–13523, 1992.

[117] Yoshihiro Nakato, Keiichi Ueda, Hiroyuki Yano, and Hiroshi Tsubomura. Effect of microscopic discontinuity of metal overlayers on the photovoltages in metal-coated semiconductor-liquid junction photoelectrochemical cells for efficient solar energy conversion. *The Journal of Physical Chemistry*, 92(8):2316–2324, 1988.

[118] Synopsis. TCAD Sentaurus. Oct. 4, 2012, (http://www.synopsys.com).

[119] A. Heller, E. Aharonshalom, W. A. Bonner, and B. Miller. Hydrogen-evolving semiconductor photo-cathodes - nature of the junction and function of the platinum group metal catalyst. *Journal of the American Chemical Society*, 104(25):6942–6948, 1982.

[120] M. Szklarczyk and J. Ombockris. Photoelectrocatalysis and electrocatalysis on p-silicon. *Journal of Physical Chemistry*, 88(9):1808–1815, 1984.

[121] R. C. Rossi and N. S. Lewis. Investigation of the size-scaling behavior of spatially nonuniform barrier height contacts to semiconductor surfaces using ordered nanometer-scale nickel arrays on silicon electrodes. *Journal of Physical Chemistry B*, 105(49):12303–12318, 2001.

[122] Yoshishiro Nakato and Hiroshi Tsubomura. Structures and functions of thin metal layers on semiconductor electrodes. *Journal of Photochemistry*, 29(1–2):257–266, 1985. ISSN 0047-2670.

[123] S. Litster and G. McLean. PEM fuel cell electrodes. *Journal of Power Sources*, 130 (1–2):61–76, 2004. ISSN 0378-7753.

[124] M. D. Kelzenberg, M. C. Putnam, D. B. Turner-Evans, N. S. Lewis, and H. A. Atwater. Predicted efficiency of si wire array solar cells. In *Photovoltaic Specialists Conference (PVSC), 34th IEEE*, pages 001948–001953, 2009.

[125] M. G. Deceglie, V. E. Ferry, A. P. Alivisatos, and H. A. Atwater. Design of nanostructured solar cells using coupled optical and electrical modeling. *Nano Letters*, 12 (6):2894–2900, 2012.

[126] J. Shi, D. Kojima, and M. Hashimoto. The interaction between platinum films and silicon substrates: Effects of substrate bias during sputtering deposition. *Journal of Applied Physics*, 88(3):1679–1683, 2000.

[127] A Tanabe, K Konuma, N Teranishi, S Tohyama, and K Masubuchi. Influence of fermi level pinning on PtSi schottky-barrier contacts to p-Si. *Journal of Electronic Materials*, 19(7):36, 7 1990. ISSN 0361-5235.

[128] Yi Wei Chen, Jonathan D. Prange, Simon Dhnen, Yohan Park, Marika Gunji, Christopher E. D. Chidsey, and Paul C. McIntyre. Atomic layer-deposited tunnel oxide stabilizes silicon photoanodes for water oxidation. *Nature Materials*, 10(7):539–544, 2011.

[129] Leslie E. O'Leary, Erik Johansson, Bruce S. Brunschwig, and Nathan S. Lewis. Synthesis and characterization of mixed methyl/allyl monolayers on Si(111). *The Journal of Physical Chemistry B*, 114(45):14298–14302, 2010.